Cryoelectron tomography of bacteria and their macromolecular machines

Thesis by

Gavin Erick Murphy

In Partial Fulfillment of the Requirements

for the Degree of

Doctor of Philosophy

California Institute of Technology

Pasadena California

2007

(Defended May 4, 2007)

ET IGNOTAS ANIMUM DIMITTIT IN ARTES
NATURAMQUE NOVAT

Ovid, Metamorphoses, VIII 188-9

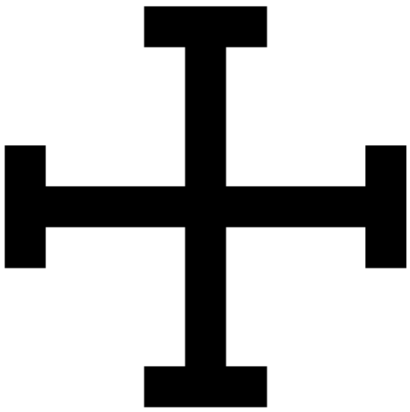

Dein Reich komme, Dein Wille geschehe

Acknowledgements

I dedicate this thesis to my parents Leo Anthony Murphy and Victoria Mary Murphy. They have loved and supported me every day and been a center around which to orient my life.

I would like to thank Grant Jensen for being a model professor, mentor, and family man who I hope to equal one day. He is a forward-thinking scientist with great thinking and motivation. He has always been fun, helpful, accessible, and thankfully tolerant of nocturnal graduate students. I owe him for having such a productive graduate career.

I am glad to have gotten to know and collaborate with Jared Leadbetter and Eric Matson. Three of my thesis chapters would be missing without Jared's inspiration and help. I look forward to learning more about microbiology from him.

I am thankful that I came to Caltech where I have received an excellent education and met many good people. I am happy to have worked with Dylan Morris, Greg Henderson, Jordan Benjamin, Lu Gan, Zhuo Li, and Zhiheng, fun guys, and to have had the pleasure of working with Elizabeth Wright, Cristina Iancu, and Ariane Briegel, who brighten the lab with their presence. I appreciate the work of D. Prabha Dias and Bill Tivol because they have kept the lab or microscope running. Thanks go to Bernard Heymann, Jane Ding and Andy Rawlinson for helping me solve numerous problems.

Lastly, my Caltech experience was fun because of my friendship with Adam Dennis, Chad Vecitis, Dave Ebner, Erik Rodriguez, Heather Murrey, my time with the late Caltech rugby team, the Beavers and my enjoyment of the finer things of life.

Abstract

Cryoelectron tomography (CET) fills a glaring gap in the imaging capabilities of biology by reconstructing cells to medium resolution. The technique was applied in three areas to understand biology's macromolecular machines: (1) the quaternary structure of the octahedrally-cored *E. coli* pyruvate dehydrogenase (PDHC) and 2-oxoglutarate dehydrogenase (OGDHC) complexes *in vitro*; (2) the ultrastructure of the spirochete *Treponema primitia;* and (3) the structure of the *in situ* flagellar motors from *T. primitia*, *Hylemonella gracilis*, *Caulobacter crescentus*, and *Vibrio cholerae*. Whereas the complexes PDHC and OGDHC were thought to have their subunit proteins E1 and E3 bound directly to the octahedral E2 core—the so-called face/edge model—it was discovered that the subunits are flexibly tethered 11 nm from the corners of the core. Several novel structures were discovered in the spirochete *T. primitia*. Spirochetes are spiral-shaped cells that propel themselves with periplasmic, not external, flagella. Bowl-shaped structures dot its surface and hook-like appendages that form arcades stripe the length of the cell. Fibrils extend from its cell tips that might help attach the cells to surfaces. Inside the periplasm, porous, cone-shaped structures reside at each cell tip and a second periplasmic layer undergirds its outer membrane, which might prevent the periplasmic flagella from rupturing the cell. Previous imaging of the flagellar motor produced either high-resolution reconstructions of the purified basal body removed from its context or low-resolution images of the *in situ* motor. Our *in situ* 3-D reconstructions described for the first time the structure of the stators, the membrane embedded component that spins the rotor. Novel shapes were discovered that indicate there are various attachments and versions of the flagellar motor that were never expected.

Table of Contents

List of Tables and Figures

Chapter I

Introduction

Cryoelectron Tomography

Decades ago the paradigm for cellular components was the one-gene/one-protein model, where the activities of the cell were performed by independent proteins catalyzing second-order reactions as they diffused and rotated quickly through the cell[1]. Today we understand that it is more complicated. The cell is a factory with ordered and regulated assembly lines whose activities are performed by macromolecular assemblies that can rightly be called machines. An important goal is to understand what these machines consist of, how they work, and how to modify them to serve us. How to understand them? It would be simpler to focus on individual proteins because these machines are often labile complexes difficult to purify and difficult to study with more established techniques, however, it is crucial to study them as a whole and preferably in their cellular context. Cryoelectron tomography allows us to do that.

Existing techniques left a gap between low-resolution and high-resolution. Light microscopy can view whole and living cells but the resolution is limited to the wavelength, around 400 nm. NMR and X-ray crystallography can produce atomic resolution structures but are typically limited to smaller domains or monomers. X-ray crystallography also can produce atomic structures, but requires that the protein be crystallizable: The bigger and more flexible the object, the less likely it will crystallize. Macromolecular machines are definitely large and some are necessarily flexible.

Cryoelectron microscopy-based single particle analysis can produce medium resolution (7–30 Å) structures of large complexes and can tolerate some flexibility, but requires purified complexes. Loosely bound adaptor proteins can be lost in the purification. Cryoelectron tomography (CET) fills this gap. Individual cells and complexes can be reconstructed without averaging to resolutions reaching 40 to 50 Å.

CET is a relatively new technique that extends traditional transmission electron microscopy (TEM)[2-5]. The first application to prokaryotes was in 1998[6]. TEM has produced much of our information in cell biology starting from the 1940s[7], but it introduces artifacts to the sample that undermine confidence in fine details. Traditionally, in order to view biological samples in the vacuum of the electron microscope (EM), the samples had to be fixed, dehydrated, embedded in resin, sectioned with an ultramicrotome, and stained with heavy metals—a lengthy and error-prone procedure. CET preserves samples in a nearly life-like state because the samples are flash-frozen in a thin layer of liquid to produce transparent, vitreous ice. Were the samples thawed, many cells would still be alive. The samples are kept frozen in the microscope during imaging.

CET produces 3-D reconstructions instead of just 2-D TEM images. Tomography is an imaging strategy that produces 3-D tomograms of a sample from 2-D projections using any electromagnetic radiation like light, X-rays (e.g., CAT scans), or electrons. Light's wavelength is on the order of hundreds of nanometers; an X-ray's is on the order of ångstroms and an electron's is on the order of picometers. Electrons are superior to X-rays because of the high number of useful scattering events for each instance of radiation damage and because electrons can be focused[8]. In order to produce a

tomogram, a tilt-series must be collected—ideally from -90 degrees to 90 degrees with a fine increment, while preserving the imaging conditions throughout. To do so manually with an EM is too time-consuming, but with the introduction of modern instruments and automated data-collection in the last decade, CET is possible.

There are many factors to be adjusted to collect excellent data, most of which are determined by the chief problem with biological samples: their limited dose-tolerance. Beyond a radiation threshold of ~ 80–200 electrons/$Å^2$, organic compounds are destroyed and literally bubble within the ice. The maximum dose must be fractionated over the total number of images[9]. The number of images should not be too high, or else each image would receive an insufficient dose, nor should they be too low, or else insufficient information will be collected. The minimum number is determined by the Crowther criterion, where the tilt increment is equated to 180º multiplied by the desired resolution distance (i.e., the inverse of the resolution) and divided by the product of the object's diameter and Pi[6, 10]. The number of images is then determined by the maximum tilt range of the microscope's goniometer, which is typically ±70˚. The inability to collect over the full 180º results in the missing wedge problem where typically ~ 30% of the information is missing, which results in features parallel to the sample plane being poorly resolved. The two factors governing the tilt increment are the sample diameter and the desired resolution. The greater the object's diameter and the better the desired resolution, the finer the increment and the more images needed, which, if taken too far, will lower the signal-to-noise ratio of each image and yield a useless reconstruction.

The object's diameter should be narrow not only to allow sufficient information to be collected, but to minimize the number of inelastic scattering events, which not only are

devoid of useful projection data, but also damage the sample. Like shooting a bullet into a forest—the greater the number of trees, the less likely a bullet will avoid a tree. For a microscope with an accelerating voltage of 300 keV, like the F30 Polara of the Jensen lab, the mean inelastic free path is 350 nm[11], which means the mean distance an electron will travel through a sample before causing an inelastic event is 350 nm. Samples should thus be narrower than that to produce excellent tomograms.

The desired resolution should be realistic in consideration of the object's diameter and is typically worse than 5 nm and even poorer for thicker samples[6, 12]. Given the expected resolution, one chooses the defocus and the magnification. The defocus' effect is much like an electromagnetic aperture, in a sense cutting off information past a certain resolution[13]. By removing noisier high-resolution information, the contrast is improved at the expense of lower resolution. (Contrast is the ratio of the difference in intensity of the foreground and background divided by the background intensity.) The defocus is set so that information past the desired resolution is affected. Since the data must be pixelated in order to use computational image processing and reconstruction, necessarily the limitations of discrete sampling must be considered. The limiting Nyquist resolution distance is twice the sampling[13], i.e., the pixel value—for example, a sampling of 13.4 Å/pixel would have a Nyquist resolution distance of 26.8 Å. Truly, the limiting resolution is two-thirds the Nyquist frequency, or in this example, 40 Å, because of non-ideal conditions. The magnification must be set high enough to achieve the desired resolution.

From the tilt series a reconstruction is calculated using a weighted back-projection algorithm[10]. If the data were collected well, the Fourier structure factors would have

been sampled finely enough to achieve the desired resolution. The tomogram might not be the final step because identical 3-D particles within multiple reconstructions can be computationally extracted, aligned, and averaged to produce structures with a better signal-to-noise ratio[14]. This was first done with an unknown cytoplasmic protein in 2003[15], and there are tens of additional examples to date—like surface and capsid proteins from HIV and other viruses[16-23], the nuclear pore complex[24], microtubules[25, 26], and the flagellar motor[27].

CET is relatively young, so improvements are still being made. Dual-axis tomography is a method that recovers some of the missing wedge information by tilting the sample in two orthogonal directions. This produces a missing pyramid that lacks less than half as much information. The Jensen lab advanced the technique by helping design and implement a dual-tilt cartridge which improves the resolution and decreases the degree of anisotropy (see Appendix A)[28]. A protocol was also written on the proper use of the Vitrobot (see Appendix B)[29].

Discoveries

Armed with the powerful technique of CET, the goal of studying macromolecular machines in their cellular context or *in vitro* was achieved. Biological discoveries were made in three areas: (1) the quaternary structure of the octahedrally-cored, *E. coli* pyruvate dehydrogenase and 2-oxoglutarate dehydrogenase complexes (PDHC and OGDHC, respectively), described in Chapter II;[30] (2) the novel surface and periplasmic ultrastructure of the spirochete *Treponema primitia*, described in Chapter IV; and (3) the

structure of *in situ* flagellar motors from *T. primitia*[27], *Hylemonella gracilis*, *Caulobacter crescentus*, and *Vibrio cholerae*, described in Chapters III, V, and VI.

Pyruvate dehydrogenase and 2-Oxoglutarate dehydrogenase complexes

PDHC and OGDHC were studied with CET because although there was some indication that the peripheral subunits E1 and E3 were separated by a gap from the core E2 complex, the reigning model of the complexes was the face/edge model[31]. 12 E1 dimers were thought to be bound directly to the 12 edges of the E2 octahedral (i.e., cubic) core, and 6 E3 dimers were thought to be bound directly to the 6 faces. The model was based on 3 lines of evidence: (1) stoichiometry results which gave chain ratios of E1:E2:E3 as 2:2:1, which matches the number of edges and faces of a cube;[32] (2) negatively-stained TEM images of the complex which appeared to have subunits bound directly to the core[33, 34]; and (3) scanning transmission electron microscopy (STEM) results of the radial masses of the full and partial complexes, which were interpreted as supportive of the face/edge model[35]. Previous attempts failed to obtain a 3-D structure of the two complexes using single particle analysis (SPA) of 2-D cryoelectron microscopy (CEM) images because it was concluded that the position of the subunits was too variable[36, 37]. SPA requires one or a few stable and reproducible conformations of an object in order to classify and average together similar particles[13].

Dual-axis tomography was used to reconstruct *in vitro* complexes using high doses and high defocuses in order to improve contrast. The paper describing the results was published in *Structure* in December, 2005, and is reproduced in Chapter II[30]. The chief biological discovery was that the subunits E1 and E3 are flexibly tethered 11 nm

from the corners of the E2 cubic core and are definitely not bound directly to the core. The technological advance was that domains as small as 80 kilodaltons (kDa) could be resolved (in the microscopic sense), though not to a high enough resolution to computationally fit in crystal structures. Also, in contrast to contemporary studies of the flexible antibody, which compensated for low defocuses and low doses with extensive denoising and enhancement[38], no denoising was used to visualize the PDHC and OGDHC complexes. The dual-axis reconstruction had enough contrast and resolution as is to make the discoveries. The insight is that rather than having the three enzymes unconnected and diffusing independently through the bacterial cell, nature has instead brought them all together to form an assembly line or machine so that the metabolites are effectively concentrated where they are produced and modified. Nature has produced two variants of the PDH complex: the octahedrally cored version present in a portion of the Bacterial kingdom, and the icosahedrally cored version present in the rest of the Bacteria and in Eukaryotes. All are similar in having an E2 core with one or both subunits flexibly tethered close by.

Ultrastructure of *Treponema primitia*

The second project was the ultrastructure of *Treponema primitia*. It is a member of the Phylum *Spirochaetes*, which are helical or undulate cells propelled by periplasmic, rather than external, flagella[39]. *T. primitia* lives in the hindgut of the termite *Zootermopsis angusticolis* and synthesizes acetate as a foodstuff for itself and its host from H_2 and CO_2, which are intermediates produced during the fermentation of wood polysaccharides[40-42]. It was studied with CET, instead of the more commonly known

bacteria like *E. coli* or *Salmonella*, because it is 350 nm narrow, which is around the mean free inelastic path of the microscope, and because it participates with other microbes in the biotechnologically relevant process of biofuel production.

What was known of its ultrastructure and that of other spirochetes came from TEM images and non-cryo ET reconstructions, which revealed its two membranes, its periplasmic flagella, and, in one instance, cytoplasmic filaments[42-44]. Some termite gut spirochetes were found to definitely attach at their cell poles to neighboring protozoa, and in one case, actually help propel it[43, 45, 46]. Surface structures were a major finding in the author's CET reconstructions of *T. primitia*, and different kinds have been seen before in other cells. In general, surface structures serve as protective coatings, as platforms for adhesion and interaction with neighbors and hosts, and in motility[47]. S-layers are proteinaceous networks often packed in crystalline arrays[47] that act as an additional cell wall in Bacteria and Archaea. Unusual grappling-hook structures called "hami" tie together neighboring archaea in one species[48]. "Goblets," which actually resemble goblets, fully coat the surface of the bacteria *Flexibacter polymorphus*[49, 50]. Fibrils like pili and fimbriae may attach to other cells or surfaces, may transfer genetic information or serve in motility[51].

Three surface structures, two of them novel, and two novel periplasmic structures were discovered through CET reconstructions of *T. primitia*. Its flagellar motor was also well reconstructed, but will be discussed in the next section. Fibrils extended in one or two tufts from either cell pole for hundreds of nanometers. They may help the cells to attach to each other, other organisms, or surfaces. "Surface bowls" dotted, but did not fully cover, its outer membrane (OM). They appeared to be spread out mostly randomly,

except for one case where three rows of bowls spiraled around a portion of a cell. Rows of "surface hook arcades" wrapped around some cells. They formed a series of arches, and each arch was composed of two counteropposed hooks. The best guess for their function is to increase drag, which is essential for current models of spirochete motility and will be discussed later. At each tip were "periplasmic cones" that appeared to be porous-like and even maintained their cone shape in connected, undivided cells. The discovery of a second outer periplasmic layer (OPL), perhaps consisting of peptidoglycan, resolves the conundrum of how spirochetes can rotate their flagella inside the periplasm without rupturing or desupporting the outer membrane. Flagella (PF) were observed between the inner periplasmic layer (IPL) and the OPL. In the cytoplasm were membrane invaginations, 30 nm wide spherical bodies, a central zone free of ribosome-like particles that may be the nucleoid, and arrays near the tips under the inner membrane (IM) that may be chemotaxis arrays.

Spirochete motility models are complicated and untested, and the newly observed ultrastructure was reconciled with them. For *T. primitia's* class of spirochete, it is believed that the rotation of the PF causes the outer sheath (OS), which is the OM and OPL, to rotate in one direction[52, 53]. The drag or shear of the OS provides the foothold for the protoplasmic cylinder (PC), which is the IM and IPL, and concomitantly, the attached PF and the OS, to counterrotate. The whole cell drills through gel-like viscous media and moves forward. See Chapter IV for a fuller discussion.

In situ flagellar motors

The bacteria flagella motor is a fascinating macromolecular machine that can rotate at speeds between 3600 and 60000 rpm in various bacteria, and although it is slower than the 80,000 to 150,000 rpm speeds of a jet turbine, the flagella motor is even more remarkable for its ~ 50–70 nm size. It is a focus of active research because of its amazing ability to assemble itself, to rotate at high speeds, and to tolerate symmetry mismatch between all of its components. The motor has been reviewed extensively[54-57] and will be described briefly. The motor moves the bacteria by using either a proton or sodium concentration gradient to turn the propeller-like flagellar. The power-generating components of the motor are located in the inner membrane, and the shaft extends from there out through the peptidoglycan (PG) layer and outer membrane and connects to the several-micron-long flagella.

The motor is composed of more than 20 proteins and is assembled by an additional 30 (Figure I-1). The *Salmonella* and *E. coli* motors have been the most studied versions, and these cells have exterior flagella. The part of the motor proximal to the cell is called the basal body and comprises the most important components. The rotor is the first component to be assembled; it consists of ~ 26 copies of FliF, and has a mean symmetry of 25–26[58, 59] (Figure I-2). Bound to the rotor comes the same number of FliG proteins, to which are then attached the C ring[55]. The C ring resides in the cytoplasm just below the rotor and has a larger diameter than the rotor. The C ring has a mean symmetry of 34 and consists of approximately 34 copies of FliM and ~ 4 times as many copies of FliN[60, 61]. The C ring is the switchgear for the motor and causes the motor to rotate CCW or CW. Many more assembly proteins attach themselves to this

initial complex and create the export apparatus. Through it and atop the rotor is built the flagella rod or shaft, which has 11-fold helical symmetry. As the shaft rises, a hole is cut through the PG layer. Between this layer and the shaft many species then attach a bushing called the P ring, which is made from FlgI proteins. An additional bushing through the OM, called the L ring, is then made from FlgH proteins. As the shaft rises outwards, a hook is created to turn rotation motion into propeller motion, and finally the several-micron long flagella is built and eventually capped by a 5-fold symmetric complex. Sometime between the creation of the C ring and the capping of the flagella, several stators are assembled around the rotor and on top of the C ring. The stators convert the electro-chemical energy of the gradient into mechanical energy to turn the rotor. Each stator is thought to be composed of a complex of 4 MotA and 2 MotB proteins[62]. The maximum number of stator "studs" appears to be either 12 or 16 in various species.

The nearly occult numerology of the flagella motor, among other problems, has confused attempts to propose mechanisms[55, 63]. In *Salmonella* and *E. coli*, it is believed that the N-terminal portion of FliG attaches to the 26-fold symmetric rotor while its middle and C-terminal portions rest upon FliM of the 34-fold symmetric C-ring[64]. Some portion of FliG must tether the rotor to the C ring. The critical, rotation-generating interaction occurs between MotA's charged, cytoplasmic domain and the complementarily charged domain of FliG (Figure 3)[56]. The difference of 8 between the symmetries of the rotor and stator, which equaled the estimated number of torque-generating units in resurrection studies of the stators[65], led to suggestions that the stators fit over the 8 unmatched FliM proteins. However, it is unlikely that MotA can

directly interact with FliM, and the variable symmetry of the C ring and rotor discourages models that rely on numerically-precise interactions[66]. The motor can probably tolerate a variety of numerical mismatches, which is remarkable for a machine. Human-made machines rely on precise interactions of gears and cogs. It is more likely that the MotA domains "walk" upon the FliG domains and that the number of gaps is insufficient to make enough MotA domains detach from the C ring[67]. The tethered rotor and its attached rod would then rotate along with the C ring.

Spirochetes contain many of the same components as other bacteria, with some minor differences. The sequenced *Borrelia* and *Treponema* species (*B. garinii*, *T. pallidum*, and *T. denticola*) do not have the FlgH L ring genes, as is expected since the flagella does not go through the OM, however, *Leptospira interrogans* does[57]. *Borrelia* and *Leptospira* have the FlgI P ring genes, but *Treponema*, curiously, do not[57]. This information is helpful for understanding what the alternative bushing is in *T. primitia*. Additionally, Blast searches found no genes for the P and L rings in *Firmicutes*, so perhaps they use the same bushing as *Treponema*. Since not much is known about the copy numbers of the components in Spirochetes, it is assumed that they are similar to *Salmonella* and *E. coli*.

Until two decades ago, our knowledge of the flagellar motor basal body came from 2-D TEM images[68-79] (Figure I-4). Only general features could be seen, and some approximate measurements were taken of the components. Most of our detailed information about the motor comes from single particle analysis of cryo-EM images of the *in vitro Salmonella* basal body[59, 60, 63, 80, 81]. The *Caulobacter crescentus* basal body without the C ring has also been reconstructed[82]. This technique necessarily must

study biochemically-isolated objects, which not only removes the rotor and such from its bacterial context, but also might remove loosely bound proteins. The *in situ* motor has been imaged using negatively stained, freeze-etched samples. The number of stator studs has been counted in such a way, and so has the *in situ* shape of the C ring, however, the images are 2-D, difficult to interpret, and measurements can only be estimated. Science has until recently had to settle for cartoons of the *in situ* motor.

In situ CET reconstructions of the flagellar motor from *T. primitia*, *Hylemonella gracilis*, *Caulobacter crescentus*, and *Vibrio cholerae* show the entire machine in its cellular context as if frozen in time. The chief discovery was the stators, which were revealed in 3-D for the first time. *T. primitia*'s structure was determined first. Its stators had strong 16-fold symmetry, but the studs were twenty times larger than that of the two OmpA domains of each stator complex. *H. gracilis*'s stator region had variable symmetry. Only the 13-fold class average showed stud density, and the volume of the studs was as expected. No stator symmetry was detectable in the others, but a stator ridge was visible in *C.c.* The diameter of the stator region was ~ 60, ~ 50 and ~ 40 nm in *T. primitia*, *H. gracilis*, and *C. caulobacter*, respectively, so there is variability in the diameters of flagellar motors across species. The C ring diameter matched the stator diameter, justifying the belief that the stators make crucial interactions with the C ring. Novel structures were seen in *T. primitia*: instead of a P ring, it had a P collar. Export apparatus shapes—i.e. a ring and what could be a ribosome—were found in nearly all motors under the rotor. An extended "E" collar was seen in *H. gracilis*, and the presence of a T ring was also found in *V. cholerae*, just as in *V. alginolyticus* (Figure I-3c)[83]. See Chapter VI for a more complete comparison of the motors. Each motor structure had

some unexpected difference in diameter or structure, so new discoveries will probably be made as the flagellar motors from other species are studied.

References

1. Alberts, B. The cell as a collection of protein machines: preparing the next generation of molecular biologists. *Cell*. **92**, 291-4 (1998).
2. Jensen, G. J., and Briegel, A. How electron cryotomography is opening a new window onto prokaryotic ultrastructure. *Curr Opin Struct Biol*. **17**, 260-7 (2007).
3. Lucic, V., Forster, F., and Baumeister, W. Structural studies by electron tomography: from cells to molecules. *Annu Rev Biochem*. **74**, 833-65 (2005).
4. McIntosh, R., Nicastro, D., and Mastronarde, D. New views of cells in 3D: an introduction to electron tomography. *Trends Cell Biol*. **15**, 43-51 (2005).
5. Subramaniam, S., and Milne, J. L. Three-dimensional electron microscopy at molecular resolution. *Annu Rev Biophys Biomol Struct*. **33**, 141-55 (2004).
6. Grimm, R., et al. Electron tomography of ice-embedded prokaryotic cells. *Biophys J*. **74**, 1031-42 (1998).
7. Frey-Wyssling, A. The submicroscopic structure of the cytoplasm. *J R Microsc Soc* **60**, 128-139 (1940).
8. Henderson, R. The potential and limitations of neutrons, electrons and X-rays for atomic resolution microscopy of unstained biological molecules. *Q Rev Biophys* **28**, 171-193 (1995).

9. McEwen, B. F., Downing, K. H., and Glaeser, R. M. The relevance of dose-fractionation in tomography of radiation-sensitive specimens. *Ultramicroscopy*. **60**, 357-73 (1995).

10. Frank, J. *Electron Tomography*. Springer, New York (2006).

11. Grimm, R., Typke, D., Barmann, M., and Baumeister, W. Determination of the inelastic mean free path in ice by examination of tilted vesicles and automated most probable loss imaging. *Ultramicroscopy*. **63**, 169-79 (1996).

12. Koster, A. J., et al. Perspectives of molecular and cellular electron tomography. *J Struct Biol*. **120**, 276-308 (1997).

13. Frank, J. *Three-Dimensional Electron Microscopy of Macromolecular Assemblies*. Oxford University Press, Inc., New York (2006).

14. Walz, J., et al. Electron Tomography of Single Ice-Embedded Macromolecules: Three-Dimensional Alignment and Classification. *J Struct Biol*. **120**, 387-95 (1997).

15. Grunewald, K., Medalia, O., Gross, A., Steven, A. C., and Baumeister, W. Prospects of electron cryotomography to visualize macromolecular complexes inside cellular compartments: implications of crowding. *Biophys Chem*. **100**, 577-91 (2003).

16. Cardone, G., et al. Visualization of the herpes simplex virus portal in situ by cryo-electron tomography. *Virology* (2006).

17. Chang, J. T., Schmid, M. F., Rixon, F. J., and Chiu, W. Electron cryotomography reveals the portal in the herpesvirus capsid. *J Virol*. **81**, 2065-8 (2007).

18. Deng, B., O'Connor, C. M., Kedes, D. H., and Zhou, Z. H. Direct visualization of the putative portal in the Kaposi's sarcoma-associated herpesvirus capsid by cryoelectron tomography. *J Virol*. **81**, 3640-4 (2007).

19. Forster, F., Medalia, O., Zauberman, N., Baumeister, W., and Fass, D. Retrovirus envelope protein complex structure in situ studied by cryo-electron tomography. *Proc Natl Acad Sci U S A*. **102**, 4729-34 (2005).

20. Harris, A., et al. Influenza virus pleiomorphy characterized by cryoelectron tomography. *Proc Natl Acad Sci U S A*. **103**, 19123-7 (2006).

21. Zanetti, G., Briggs, J. A., Grunewald, K., Sattentau, Q. J., and Fuller, S. D. Cryo-Electron Tomographic Structure of an Immunodeficiency Virus Envelope Complex In Situ. *PLoS Pathog*. **2** (2006).

22. Zhu, P., et al. Electron tomography analysis of envelope glycoprotein trimers on HIV and simian immunodeficiency virus virions. *Proc Natl Acad Sci U S A*. **100**, 15812-7 (2003).

23. Zhu, P., et al. Distribution and three-dimensional structure of AIDS virus envelope spikes. *Nature*. **441**, 847-52 (2006).

24. Beck, M., et al. Nuclear pore complex structure and dynamics revealed by cryoelectron tomography. *Science*. **306**, 1387-90 (2004).

25. Garvalov, B. K., et al. Luminal particles within cellular microtubules. *J Cell Biol*. **174**, 759-65 (2006).

26. Nicastro, D., McIntosh, J. R., and Baumeister, W. 3D structure of eukaryotic flagella in a quiescent state revealed by cryo-electron tomography. *Proc Natl Acad Sci U S A*. **102**, 15889-94 (2005).

27. Murphy, G. E., Leadbetter, J. R., and Jensen, G. J. In situ structure of the complete Treponema primitia flagellar motor. *Nature*. **442**, 1062-4 (2006).

28. Iancu, C. V., et al. A "flip-flop" rotation stage for routine dual-axis electron cryotomography. *J Struct Biol*. **151**, 288-97 (2005).

29. Iancu, C. V., et al. Electron cryotomography sample preparation using the Vitrobot. *Nat Protoc*. **1**, 2813-9 (2006).

30. Murphy, G. E., and Jensen, G. J. Electron cryotomography of the E. coli pyruvate and 2-oxoglutarate dehydrogenase complexes. *Structure*. **13**, 1765-73 (2005).

31. de Kok, A., Hengeveld, A. F., Martin, A., and Westphal, A. H. The pyruvate dehydrogenase multi-enzyme complex from Gram-negative bacteria. *Biochim Biophys Acta*. **1385**, 353-66 (1998).

32. Reed, L. J., et al. Reconstitution of the Escherichia coli pyruvate dehydrogenase complex. *Proc Natl Acad Sci U S A*. **72**, 3068-72 (1975).

33. Bleile, D. M., Munk, P., Oliver, R. M., and Reed, L. J. Subunit structure of dihydrolipoyl transacetylase component of pyruvate dehydrogenase complex from Escherichia coli. *Proc Natl Acad Sci U S A*. **76**, 4385-9 (1979).

34. Oliver, R. M., and Reed, L. J. Multienzyme Complexes in *Electron Microscopy of Proteins*. (Harris, R., ed.), Academic Press, London, (1982).

35. Yang, H. C., Hainfeld, J. F., Wall, J. S., and Frey, P. A. Quaternary structure of pyruvate dehydrogenase complex from Escherichia coli. *J Biol Chem*. **260**, 16049-51 (1985).

36. Wagenknecht, T., Grassucci, R., Berkowitz, J., and Forneris, C. Configuration of interdomain linkers in pyruvate dehydrogenase complex of Escherichia coli as determined by cryoelectron microscopy. *J Struct Biol*. **109**, 70-7 (1992).

37. Wagenknecht, T., Grassucci, R., and Schaak, D. Cryoelectron microscopy of frozen-hydrated alpha-ketoacid dehydrogenase complexes from Escherichia coli. *J Biol Chem*. **265**, 22402-8 (1990).

38. Sandin, S., Ofverstedt, L. G., Wikstrom, A. C., Wrange, O., and Skoglund, U. Structure and flexibility of individual immunoglobulin G molecules in solution. *Structure*. **12**, 409-15 (2004).

39. Li, C., Motaleb, M. A., Sal, M., Goldstein, S. F., and Charon, N. W. Gyrations, rotations, periplasmic flagella: the biology of spirochete motility in *The Spirochetes Molecular and Cellular Biology*. (Saier, M. H., Jr & Garcia-Lara, J., eds.), Horizon Press, Norfolk (2001).

40. Breznak, J. A., and Switzer, J. M. Acetate synthesis from H(2) plus CO(2) by termite gut microbes. *Appl Environ Microbiol*. **52**, 623-630 (1986).

41. Graber, J. R., Leadbetter, J. R., and Breznak, J. A. Description of *Treponema azotonutricium sp. nov*. and *Treponema primitia sp. nov*., the first spirochetes isolated from termite guts. *Appl Environ Microbiol*. **70**, 1315-20 (2004).

42. Leadbetter, J. R., Schmidt, T. M., Graber, J. R., and Breznak, J. A. Acetogenesis from H_2 plus CO_2 by spirochetes from termite guts. *Science*. **283**, 686-9 (1999).

43. Holt, S. C. Anatomy and chemistry of spirochetes. *Microbiol Rev*. **42**, 114-60 (1978).

44. Izard, J., et al. Tomographic reconstruction of treponemal cytoplasmic filaments reveals novel bridging and anchoring components. *Mol Microbiol*. **51**, 609-18 (2004).

45. Bloodgood, R. A., and Fitzharris, T. P. Specific associations of prokaryotes with symbiotic flagellate protozoa from the hindgut of the termite *Reticulitermes* and the wood-eating roach *Cryptocercus*. *Cytobios*. **17**, 103-22 (1976).

46. Cleveland, L. R., and Grimstone, A. V. The fine structure of the flagellate *Mixotricha paradoxa* and its associated micro-organisms. *Proc Roy Soc London*. **B159**, 668-686 (1964).

47. Fernandez, L. A., and Berenguer, J. Secretion and assembly of regular surface structures in Gram-negative bacteria. *FEMS Microbiol Rev*. **24**, 21-44 (2000).

48. Moissl, C., Rachel, R., Briegel, A., Engelhardt, H., and Huber, R. The unique structure of archaeal 'hami', highly complex cell appendages with nano-grappling hooks. *Mol Microbiol*. **56**, 361-70 (2005).

49. Ridgway, H. F. Ultrastructural characterization of goblet-shaped particles from the cell wall of *Flexibacter polymorphus*. *Can J Microbiol*. **23**, 1201-13 (1977).

50. Ridgway, H. F., Wagner, R. M., Dawsey, W. T., and Lewin, R. A. Fine structure of the cell envelope layers of *Flexibacter polymorphus*. *Can J Microbiol*. **21**, 1733-50 (1975).

51. White, D. *The Physiology and Biochemistry of Prokaryotes*. Oxford University Press, New York (2007).

52. Berg, H. C. How spirochetes may swim. *J Theor Biol*. **56**, 269-73 (1976).

53. Berg, H. C., and Turner, L. Movement of microorganisms in viscous environments. *Nature*. **278**, 349-51 (1979).

54. Berg, H. C. The rotary motor of bacterial flagella. *Annu Rev Biochem.* **72**, 19-54 (2003).

55. Kojima, S., and Blair, D. F. The bacterial flagellar motor: structure and function of a complex molecular machine. *Int Rev Cytol*. **233**, 93-134 (2004).

56. Blair, D. F. Flagellar movement driven by proton translocation. *FEBS Lett*. **545**, 86-95 (2003).

57. Limberger, R. J. The periplasmic flagellum of spirochetes. *J Mol Microbiol Biotechnol*. **7**, 30-40 (2004).

58. Suzuki, H., Yonekura, K., and Namba, K. Structure of the rotor of the bacterial flagellar motor revealed by electron cryomicroscopy and single-particle image analysis. *J Mol Biol*. **337**, 105-13 (2004).

59. Thomas, D. R., Francis, N. R., Xu, C., and DeRosier, D. J. The three-dimensional structure of the flagellar rotor from a clockwise-locked mutant of Salmonella enterica serovar Typhimurium. *J Bacteriol*. **188**, 7039-48 (2006).

60. Young, H. S., Dang, H., Lai, Y., DeRosier, D. J., and Khan, S. Variable symmetry in Salmonella typhimurium flagellar motors. *Biophys J*. **84**, 571-7 (2003).

61. Brown, P. N., Mathews, M. A., Joss, L. A., Hill, C. P., and Blair, D. F. Crystal structure of the flagellar rotor protein FliN from Thermotoga maritima. *J Bacteriol*. **187**, 2890-902 (2005).

62. Braun, T. F., Al-Mawsawi, L. Q., Kojima, S., and Blair, D. F. Arrangement of core membrane segments in the MotA/MotB proton-channel complex of Escherichia coli. *Biochemistry*. **43**, 35-45 (2004).

63. Thomas, D. R., Morgan, D. G., and DeRosier, D. J. Rotational symmetry of the C ring and a mechanism for the flagellar rotary motor. *Proc Natl Acad Sci U S A*. **96**, 10134-9 (1999).

64. Brown, P. N., Terrazas, M., Paul, K., and Blair, D. F. Mutational analysis of the flagellar protein FliG: sites of interaction with FliM and implications for organization of the switch complex. *J Bacteriol*. **189**, 305-12 (2007).

65. Blair, D. F., and Berg, H. C. Restoration of torque in defective flagellar motors. *Science*. **242**, 1678-81 (1988).

66. Thomas, D., Morgan, D. G., and DeRosier, D. J. Structures of bacterial flagellar motors from two FliF-FliG gene fusion mutants. *J Bacteriol*. **183**, 6404-12 (2001).

67. Manson, M. D. How 34 pegs fit into 26 + 8 holes in the flagellar motor. *J Bacteriol*. **189**, 291-3 (2007).

68. Abram, D., Vatter, A. E., and Koffler, H. Attachment and structural features of flagella of certain bacilli. *J Bacteriol*. **91**, 2045-68 (1966).

69. Coulton, J. W., and Murray, R. G. Cell envelope associations of Aquaspirillum serpens flagella. *J Bacteriol*. **136**, 1037-49 (1978).

70. Holt, S. C., and Canale-Parola, E. Fine structure of Spirochaeta stenostrepta, a free-living, anaerobic spirochete. *J Bacteriol*. **96**, 822-35 (1968).

71. Hovind-Hougen, K., Birch-Andersen, A., and Jensen, H. J. Ultrastructure of cells of Treponema pertenue obtained from experimentally infected hamsters. *Acta Pathol Microbiol Scand [B]*. **84**, 101-8 (1976).

72. Jackson, S., and Black, S. H. Ultrastructure of Treponema pallidum Nichols following lysis by physical and chemical methods. II. Axial filaments. *Arch Mikrobiol*. **76**, 325-40 (1971).

73. Khan, S., Dapice, M., and Reese, T. S. Effects of mot gene expression on the structure of the flagellar motor. *J Mol Biol*. **202**, 575-84 (1988).

74. Khan, S., Ivey, D. M., and Krulwich, T. A. Membrane ultrastructure of alkaliphilic Bacillus species studied by rapid-freeze electron microscopy. *J Bacteriol*. **174**, 5123-6 (1992).

75. Khan, S., Khan, I. H., and Reese, T. S. New structural features of the flagellar base in Salmonella typhimurium revealed by rapid-freeze electron microscopy. *J Bacteriol*. **173**, 2888-96 (1991).

76. Khan, S., Zhao, R. B., and Reese, T. S. Architectural features of the Salmonella typhimurium flagellar motor switch revealed by disrupted C-rings. *Journal Of Structural Biology*. **122**, 311-319 (1998).

77. Kupper, J., Wildhaber, I., Gao, Z., and Baeuerlein, E. Basal-body-associated disks are additional structural elements of the flagellar apparatus isolated from Wolinella succinogenes. *J Bacteriol*. **171**, 2803-10 (1989).

78. Nauman, R. K., Holt, S. C., and Cox, C. D. Purification, ultrastructure, and composition of axial filaments from Leptospira. *J Bacteriol*. **98**, 264-80 (1969).

79. Paster, B. J., and Canale-Parola, E. Involvement of periplasmic fibrils in motility of spirochetes. *J Bacteriol*. **141**, 359-64 (1980).

80. Francis, N. R., Sosinsky, G. E., Thomas, D., and DeRosier, D. J. Isolation, characterization and structure of bacterial flagellar motors containing the switch complex. *J Mol Biol*. **235**, 1261-70 (1994).

81. Sosinsky, G. E., Francis, N. R., Stallmeyer, M. J., and DeRosier, D. J. Substructure of the flagellar basal body of Salmonella typhimurium. *J Mol Biol*. **223**, 171-84 (1992).

82. Stallmeyer, M. J., Hahnenberger, K. M., Sosinsky, G. E., Shapiro, L., and DeRosier, D. J. Image reconstruction of the flagellar basal body of Caulobacter crescentus. *J Mol Biol*. **205**, 511-8 (1989).

83. Terashima, H., Fukuoka, H., Yakushi, T., Kojima, S., and Homma, M. The Vibrio motor proteins, MotX and MotY, are associated with the basal body of Na-driven flagella and required for stator formation. *Mol Microbiol*. **62**, 1170-80 (2006).

Figures

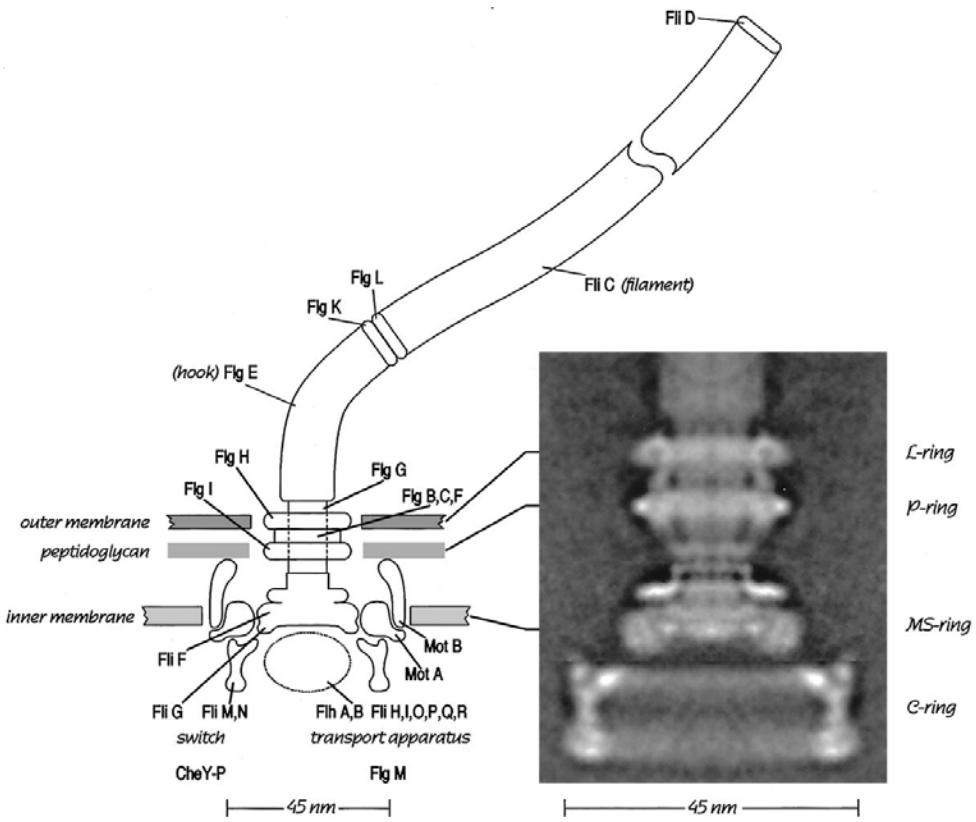

Figure I-1 Components of the flagellar motor

from Berg, HC, Annu. Rev. Biochem., 2003[54]

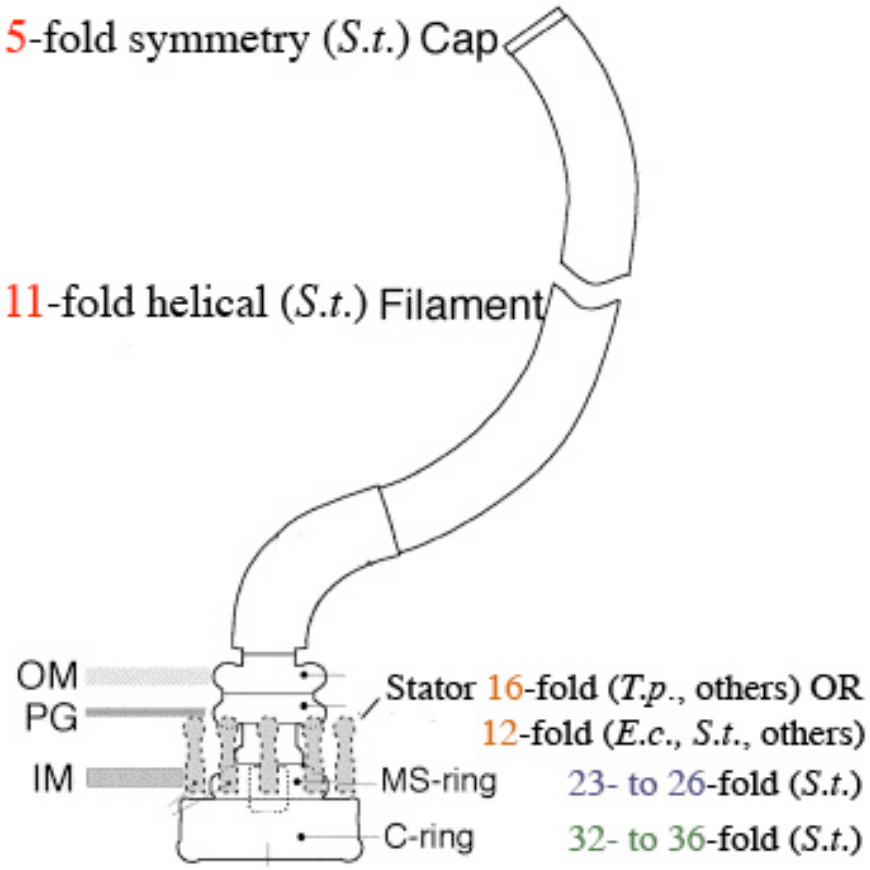

Figure I-2 Symmetry of motor components

modified from Blair, D.F., FEBS, 2003[56]

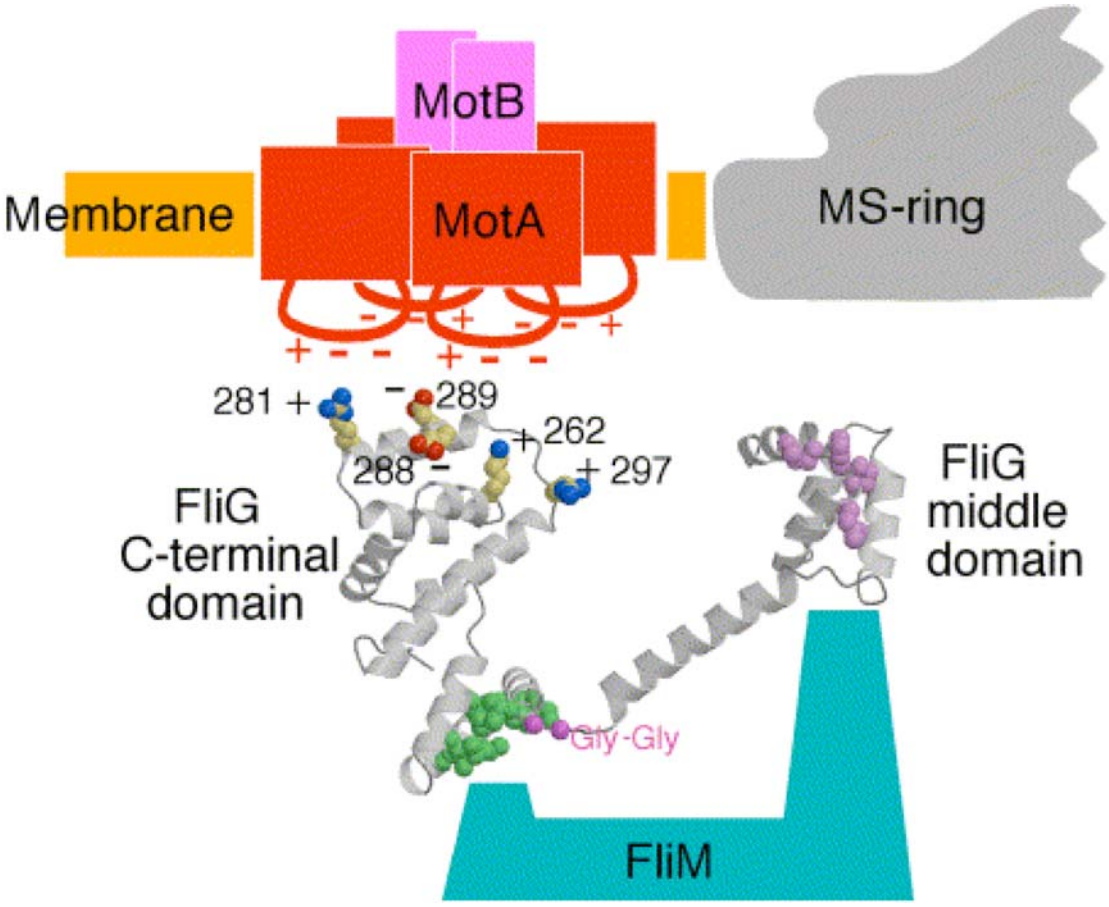

Figure I-3 Stator-C ring interaction

from Blair, D.F. FEBS, 2003[56]

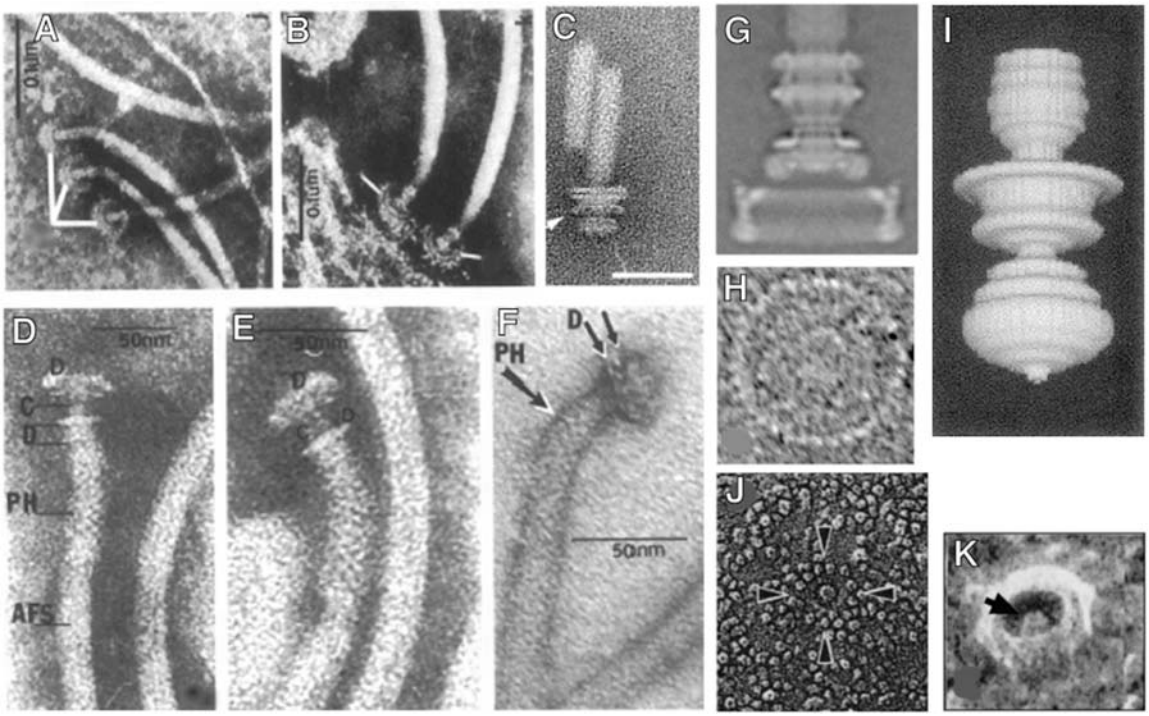

Figure I-4 Past electron microscopy of flagellar motors *in vitro* and *in situ*

(A–B) Negatively stained EM images of the *Treponema pallidum* basal body. (Panels A,B,D–F are from Holt, S.C., 1978[43].) (C) The *Vibrio alginolyticus* basal body. The arrowhead points to the novel T ring. (From Terashima, H., et al., 2006[83].) (D–E) The *Leptospira interrogans* basal body. (F) The *Spirochaeta stenostrepta* basal body. (G) Cryo EM reconstruction of the *Salmonella* basal body. (Panels G, H, J and K are from Blair, D.F., FEBS, 2003[56].) (H) Cryo EM image of the C ring from *Salmonella*. (I) The reconstructed *Caulobacter crescentus* basal body. (From Stallmeyer, M.J., et al., 1989[82].) (J) Negatively stained freeze-etch image of an *in situ* flagellar motor. (K) Negatively stained freeze-etch of a C ring from an *in situ* flagellar motor.

Chapter II

Electron cryotomography of the *E. coli* pyruvate and 2-oxoglutarate dehydrogenase complexes

Gavin E. Murphy, Grant J. Jensen*

Division of Biology, California Institute of Technology, Pasadena, CA 91125, USA

*Correspondence: 1200 E. California Blvd., Pasadena, CA 91125, 626-395-8827 (phone), 626-395-5730 (fax), Jensen@caltech.edu.

Published in Structure 2005 Dec; 13(12):1765-73.

doi: 10.1016/j.str.2005.08.01

Received 27 May 2005; revised 27 July 2005; accepted 1 August 2005. Published: December 13, 2005. Available online 13 December 2005.

Summary

The *E. coli* pyruvate and 2-oxoglutarate dehydrogenases are two closely related, large complexes that exemplify a growing number of multiprotein "machines" whose domains have been studied extensively and modeled in atomic detail, but whose quaternary structures have remained unclear for lack of an effective imaging technology. Here, electron cryotomography was used to show that the E1 and E3 subunits of these complexes are flexibly tethered ~ 11 nm away from the E2 core. This result demonstrates unambiguously that electron cryotomography can reveal the relative positions of features as small as 80 kDa in *individual* complexes, elucidating quaternary structure and conformational flexibility.

Introduction

The pyruvate and 2-oxoglutarate dehydrogenases of *E. coli* (PDHC and OGDHC, respectively) are two closely related assemblies of three protein types each (E1, E2, and E3). Together, the three enzymes catalyze five separate reactions that in sum decarboxylate 2-oxo acids and attach the remaining acyl group to coenzyme A (de Kok et al., 1998). PDHC converts pyruvate to acetyl-CoA, which then enters the citric acid cycle. OGDHC acts within the citric acid cycle, converting 2-oxoglutarate to succinyl-CoA. The E2 polypeptide (dihydrolipoamide acetyltransferase or dihydrolipoamide succinate transferase in PDHC and OGDHC, respectively) contains an ~ 26 kDa catalytic domain, an ~ 4 kDa E1/E3 binding domain, and either three or one (in PDHC and OGDHC, respectively) ~ 8 kDa lipoyl domains. Each of these domains is separated by apparently flexible "tether" sequences rich in alanine and proline and exposed to solvent (de Kok et al., 1998; Green et al., 1992; Perham, 1991). In both PDHC and OGDHC, the catalytic domains of 24 copies of E2 unite to form an octahedral "core" at the center of the complex. Outside this core, dimers of both the E3 (dihydrolipoamide dehydrogenase) and E1 (pyruvate dehydrogenase or 2-oxoglutarate dehydrogenase in PDHC and OGDHC, respectively) enzymes bind to E2's E1/E3 binding domain. In contrast, eukaryotic PDHC is icosahedral with a core made up of 60 E2s arranged as a pentagonal dodecahedron, 12 E3s bound within the pentagonal openings, and E1s bound peripherally through a flexible linker on E2 (Gu et al., 2003; Zhou et al., 2001a). In the reaction cycle, the 2-oxo acid is captured and decarboxylated by an E1 and then transferred to the mobile lipoyl domain of an E2. The lipoyl domain carries the acyl group to E2's catalytic

domain, which transfers it to coenzyme A. Acyl-CoA is released, and the lipoyl domain of E2 is regenerated (reoxidized) for another cycle by E3.

Following decades of study, atomic models for all the ordered domains of E1, E2, and E3 are now available, either directly or by homology to a closely related structure (Arjunan et al., 2002; Hendle et al., 1995; Jones et al., 2000; Mande et al., 1996). PDHC can accommodate up to 24 dimers of either E1 alone or E3 alone, and these compete for binding when mixed (Reed et al., 1975). The E1:E2:E3 chain ratio of the wild-type PDHC complex has been measured variously as 1:1:1, 2:2:1, 2:1:1, and 4:3:2 (Bosma et al., 1984; de Kok et al., 1998; Reed et al., 1975), apparently due to differing preparation and measurement methods.

Three lines of evidence led to the so-called "face/edge" model for the quaternary structure in which one E1 dimer binds to each of the 12 edges of the E2 core and one E3 dimer binds to each of the 6 faces, with the lipoyl domains moving freely above and between them. First, early experiments indicated that the highest rates of catalysis occurred with chain ratios of 2:2:1, which matches the numbers of faces and edges of a cube (Reed et al., 1975). Second, EM images of negatively stained samples, including intact and trypsin-treated PDHC complexes, as well as E2 cores, were judged to support the face/edge model, though some flexibility was suggested for the interaction of E1 with E2 (Bleile et al., 1979; Oliver and Reed, 1982). Finally, STEM images of several lyophilized and cross-linked samples, including PDHC, an E2-E3 subcomplex, and the E2 core, were used to generate radial density plots (Yang et al., 1985). Compared to the E2 core, the E2-E3 subcomplex had more mass from 0 to 11 nm. PDHC had more mass than the subcomplex from 8 to 22 nm. Because the E2 core extends up to 8 nm from the

center, and the E1 and E3 dimers have diameters of approximately 9 nm, the authors interpreted their results as supportive of the face/edge model.

A more distant and flexible attachment of the subunits to the core was shown by electron cryomicroscopy images of PDHC and OGDHC (Wagenknecht et al., 1992; Wagenknecht et al., 1990). For PDHCs loaded with either E1 or E3 separately, gaps of 4–6 and 3–4 nm were observed between the E2 core and the extra density attributed to E1 or E3, respectively. Similarly, for OGDHC, gaps of 2–4 and 3–5 nm were observed. The average distance from the center of the subunits to the center of the core was judged to be ~ 13 nm (Wagenknecht et al., 1992). The highly variable contrast extending 14–16 nm from the core's surface was attributed to the lipoyl domains. Despite this electron cryomicroscopy data supporting a flexible and extended nature of the complexes, the face/edge model has not been discarded, although it has been qualified that such a model is merely a time-averaged structure, and that the E3 subunits may be mobile (de Kok et al., 1998). Other techniques, including fluorescence energy transfer—which showed that the distance between the E1 and E3 active sites was between 3 and 6 nm—have not distinguished between the models (Moe et al., 1974). Thus PDHC and OGDHC are examples of a growing number of large macromolecular "machines" where atomic models of all the subunits are available, but the quaternary structure of the complete complex remains unclear, probably because the machine is inherently flexible or too difficult to purify to homogeneity for study by traditional means.

In order to clarify the molecular organization of these dehydrogenases, electron cryotomography was performed. In this technique, projections of a frozen sample are recorded with an electron microscope as it is tilted about one or two axes (Baumeister et

al., 1999). Thus while other standard structural biology techniques such as X-ray crystallography, NMR spectroscopy, electron crystallography, and electron cryomicroscopy-based single particle analysis all require averaging signals from large numbers of identical copies of the object of interest, electron cryotomography can be used to determine three-dimensional structures of *unique* objects ranging from whole cells to individual protein complexes. While the idea is several decades old, because the necessary instruments and protocols for this technique have only recently (~ 1997) became available, only a couple dozen applications have been published to date [for recent reviews, see (Kürner et al., 2004; McIntosh et al., 2005; Subramaniam and Milne, 2004)]. Nevertheless, these have already achieved resolutions sufficient to recognize membranes, protein shells, filaments, and some individual protein complexes. Among those that have targeted purified protein complexes (Bohm et al., 2000; Frangakis et al., 2002; Medalia et al., 2002; Nitsch et al., 1998; Sandin et al., 2004; Walz et al., 1997; Zhao et al., 2004), it has already been shown that tomographic reconstructions of individual particles are clear enough to be mutually aligned and averaged, and that different species mixed together in the same reconstruction can be distinguished computationally. It has long been hoped, however, that electron cryotomography would eventually reveal the structure of *individual* particles to high enough resolution that atomic models of subunits could simply be "docked," yielding both quaternary structure and conformational variability between particles. Indeed one recent study claimed to have done just that (Sandin et al., 2004) using small underfocuses and doses followed by extensive denoising. The reliability of the results was unclear, however, because (1) the shapes of specific domains were changed significantly by the denoising; (2) only a small

percentage of the appropriately-sized densities were then described as having "well-resolved subunits," and (3) all the remaining variability seen in this small, chosen class was attributed to conformational heterogeneity in the particles themselves, rather than as an inherent resolution limitation or an artifact of denoising.

Here a different strategy has been explored using higher defocuses and doses, but then no denoising. Dual-axis tilt-series (Iancu et al., 2005) were also used for the first time for purified protein complexes. The results are noteworthy as individual, ~ 80 kDa features within both the PDHC and OGDHC core are clearly discernible *without any averaging or denoising*; their relative positions are reproduced in many independent particles; and these positions match the known core structure well. The resolution was insufficient, however, to dock the crystal structures of the peripheral domains uniquely. Nevertheless, the results show clearly that in PDHC and ODGHC, the E1 and E3 subunits are flexibly tethered ~ 11 nm away from the E2 core.

Results

Solutions of purified PDHC and OGDHC were plunge-frozen in thin films across EM grids. Orthogonal dual-axis tilt-series (Iancu et al., 2005) were recorded through many holes in the carbon support, aligned, and merged to produce three-dimensional reconstructions of fields of particles suspended in vitreous ice. In the individual low-dose images of the tilt-series, particles were quite faint and barely recognizable (Fig. II-1a). After the reconstruction process, the complexes stood out unambiguously from the background (Fig. II-1b). All eight ~ 80 kDa corners of the E2 core were often visible in serial x-y slices of extracted, unaveraged, undenoised, and unrefined particles in which

only in-plane rotations had been performed. Their arrangement matched the low-pass-filtered E2 core crystal structure well, as could be most easily judged when the particles froze with their 4-, 3-, or 2-fold axes perpendicular to the grid (Fig. II-1c–j). The resolution was estimated to be ~5.5 nm using the Fourier Shell Correlation method. The globular nature of the peripheral subunits and their separation from the E2 core were also clear (Fig. II-2), demonstrating conclusively that the E1 and E3 subunits are indeed flexibly attached some distance away from the core, rather than bound specifically to the faces and edges. The asymmetric and non-homogenous nature of the *E. coli* PDHC prevented meaningful classification and averaging, as was done for the eukaryotic PDHC (Gu et al., 2003).

To distinguish between the face/edge and flexibly-tethered models quantitatively, their radial densities were compared to those of several individual, reconstructed particles (Fig. II-3). The radial density of the E2 core X-ray crystal structure shows a single peak at ~ 5 nm from the center. A face/edge model was built by placing 12 E1 dimers along the edges and 6 E3 dimers on the faces of the E2 core. The radial density of this model shows two peaks: the same peak at ~ 5 nm due to the E2 core, and another at ~ 10 nm from the additional E1/E3 subunits. To compare these to the experimentally reconstructed PDHC and OGDHC particles, the raw densities in the reconstructions were scaled linearly to match the atomic models at the top of the ~ 5 nm peak and decay to zero density at the edge of the reconstructed volumes. The experimentally reconstructed particles have two density peaks at ~ 5 and ~ 16 nm, separated by a clear minimum at ~ 10 nm. The "negative" densities at the origin, ~ 10 nm and ~ 25 nm in these plots, are artifacts of the point-spread-function, which under our imaging conditions looks roughly

like a sinc function with the first minima ~ 6 nm away from the center. This interpretation was confirmed by the radial density profiles of the 10 nm gold fiducials, which also show minima 6–8 nm away from their density peaks. Finally, the radial density of a fitted model of PDHC (described later) was plotted which matched the experimental densities well. Together these curves argue definitively for the flexibly-tethered model and highlight the reproducibility of the tomographic reconstructions.

Three hundred and five PDHC particles were selected from the reconstructions and aligned to the E2 crystal structure. Due to the regular configuration of the 24 E2 catalytic domains in PDHC, this alignment was straightforward and unambiguous. Next we tried to dock the structures of E1 and E3 into the peripheral densities in several reconstructions using the Situs software (Wriggers and Birmanns, 2001). Unfortunately, the peripheral tomographic densities did not partition clearly into two classes, which could potentially have corresponded to the ~ 100 kDa E3 dimer and the ~ 200 kDa E1 dimer. Thus, which peripheral densities were E1 and which were E3 could not be distinguished. This was particularly true where multiple subunits were close together or touching, yielding continuous reconstructed densities large enough to accommodate more than one E1 or E3 dimer. This fact illustrates how *distinguishing subunits* by shape or size requires higher resolution than simply *resolving their separate positions*, as was possible with the ~ 80 kDa corners of the E2 core. Nevertheless, to explore the range of positions accessible to E1/E3 subunits, three reconstructed PDHC particles (the three rendered in Fig. II-2) were thresholded so as to enclose a volume corresponding to a fully-loaded complex and crystal structures were roughly placed into the densities (Fig.

II-4). In the three interpreted structures, 24, 23 and 21 peripheral subunits could be positioned with a plausible correspondence to the surface map.

The positions of each fitted E1/E3 subunit were displayed in the same space as an averaged, octahedrally symmetrized map generated from all 305 PDHC particles (Fig. II-5a). No pattern was discerned in the positions of the E1/E3 subunits. To investigate further, the 8 corners of the core were superimposed, moving each fitted subunit accordingly to preserve its relationship to the corner. A new coordinate system was established wherein the three-fold axis of the corner was defined as the z-axis, the tip of the corner (defined by the center of the three most N-terminal residues of the E2 trimer) was defined as the origin, and the direction of the x-axis was left arbitrary. In this way the distance, relative azimuthal angle, and polar angle of the subunits' center-of-mass could be observed in relation to the corner. First, the distribution of relative azimuthal angles was displayed by rotating each subunits' center-of-mass onto the x-y plane (i.e. its polar angle was increased to 90˚). The azimuthal angle was apparently random (Fig. II-5b). Next, each center-of-mass was rotated onto the x-z plane (Fig. II-5c). The minimum, maximum, and average polar angle were 7˚, 70˚, and 41º (standard deviation 15º). The minimum, maximum, and mean distance between the corner and the subunits' centers-of-mass were 6.8, 15, and 11 nm (standard deviation 1.9 nm). Similar results were obtained for OGDHC.

Discussion

This paper reports two key findings. The first is of interest primarily to the enzymology community: that in the pyruvate and 2-oxoglutarate dehydrogenase

multienzyme complexes of *E. coli* (PDHC and OGDHC, respectively), the E1 and E3 enzymes are flexibly tethered ~ 11 nm away from the E2 core, rather than being specifically bound to the faces or edges. The second finding is of broad interest to the cell and structural biology communities: that electron cryotomography can reveal the quaternary structure and conformation of *individual* multiprotein complexes with resolutions sufficient to visualize the relative locations of features as small as 80 kDa.

Concerning the conformation of PDHC and OGDHC, the measurements of distance, azimuthal angle, and polar angle of the fitted subunits with respect to their closest corner are consistent with the hypothesis that E1 and E3 diffuse freely, constrained only by the length of their tether and steric occlusion. If the 31-residue tether between the catalytic and E1/E3 binding domains of E2 were fully extended (0.38 nm/residue), for instance, its maximum expected length would be 12 nm (blue circle in Fig. II-5). Adding the ~ 4.5 nm radius of an E1 or E3 subunit, the largest distance expected between a corner and the center-of-mass of an E1 or E3 would be ~ 16 nm, and indeed our measured maximum (15 nm) was just below that value. If the tether is assumed to be completely flexible and adopt a random-walk configuration, its expected length would be $(8/3\pi)^{1/2} N^{1/2} b$, where N is the number of steps (residues) and b is the length of one step (0.38 nm/residue) (Boal, 2002). This leads to an expected length of only 2.0 nm (purple circle in Fig. II-5). This value is too small, however, to accommodate more than just a few E1 and E3 dimers in the complete assembly. Thus the average distance of 11 nm measured here (corresponding to a tether length of ~ 6 nm, assuming the tether is usually attached to an inner-facing surface of E1 or E3) is reasonable, as it lies between these two extremes. A 9-nm thick spherical shell

(corresponding to the approximate diameter of an E1 or E3 subunit) centered on PDHC at a radius 11 nm past a corner (the average distance observed here) has a volume ~ 4.5 times larger than a full complement of 16 E1 and 8 E3 dimers. Thus this distance is also plausible for mobile and colliding subunits tethered to a common point. Concerning the polar angle, if three spheres of radius 4.5 nm are placed 11 nm away from a corner so that they just touch, their polar angles would be 29˚. The measured average of 41˚ is comfortably larger than that minimum, but no values past 70˚ are seen, since such angles would place subunits deep into the already occupied space above adjacent corners.

These results can be compared to those obtained for the eukaryotic forms of PDHC (Zhou et al., 2001b). In *Saccharomyces cerevisiae* PDHC, the E2 core is icosahedral, but expands and contracts uniformly by ~ 20%. It has been proposed that this "breathing" is thermally driven, and may augment the movement of substrates between active sites. Here no significant variation in the E2 core dimensions was measured, as predicted, because of the additional inter-trimer interactions in the *E. coli* PDHC (Zhou et al., 2001a). In the presence of substoichiometric amounts of E1, the *S. cerevisiae* E1 shell appears to be icosahedrally ordered. More complete occupancy of E1 lengthens the linker between E1 and E2 from ~ 5.0 to ~ 7.5 nm and disrupts the symmetry of the E1 shell (Gu et al., 2003). Here no evidence was found for order in the E1/E3 shell or for any preferred conformations of the ~ 11 nm linker.

In order to obtain an intuitive sense for the length of the tethers and the crowdedness within PDHC and OGDHC, and to present our flexible model visually as an alternative to the traditional face/edge model, a complete atomic model of one corner was assembled (Fig. II-6). The crystal structure for E2 was used as a starting point (Hendle

et al., 1995). A crystal structure of an E3 dimer in complex with E2's E1/E3 binding domain (Mande et al., 1996) was then fit into the three main peripheral densities seen surrounding a corner of one reconstructed PDHC. E1 was not used because there is no crystal structure available of it specifically bound to the E1/E3 binding domain. The 31-residue tether present in the E2 sequence between the catalytic and E1/E3 binding domains was modeled as a beta-strand and positioned accordingly. Finally, an NMR structure of the lipoyl domain (Jones et al., 2000) was placed at nine reasonable but purely hypothetical locations (three for each of the three E2 monomers that form the corner). The nine corresponding tether sequences were modeled between them mostly as an extended beta-strand, except wherever there was a strong secondary-structure prediction for a helix. (A schematic figure in (Aevarsson et al., 1999) previously illustrated the relative size of the components and the reaction cycle, but the length of the linkers and the crowdedness of the complex were not meant to be physically realistic.) This complete model revealed that there is still sufficient space around the subunits for the tethers and lipoyl domains to move. Given that each corner has three E2 monomers, that the E1/E3 binding domains can bind either E1 or E3, and that these subunits are flexibly tethered several nanometers away from the corner, then the entire complex is inherently nonhomogeneous, asymmetric, and flexible.

The ultimate potential of electron cryotomography is, of course, still unknown. In this study, relatively high total doses (~ 120 e^-/A^2) and high defocus values (–10 μm) were used in an effort to obtain the most interpretable reconstructions possible *without the use of any post-processing (denoising)*, which can introduce artifacts. In a comparable study (Sandin et al., 2004), much lower doses and defocus values were used,

but the reconstructions only became interpretable after extensive denoising, and the reliability of the final results was difficult to assess. Further studies are needed to determine how faithful the various denoising techniques actually are and how to optimally balance radiation damage, contrast enhancement through defocus, and denoising. Nevertheless, electron cryotomography has unambiguously demonstrated here its capacity to reveal quaternary structure and conformational variability, and should be applied generally to the myriad large, multi-protein machines found in nature.

Experimental Procedures

Sample Preparation

Unengineered PDHC and OGDHC were purified from *E. coli* and assayed for activity as described (Wagenknecht et al., 1992). Carbon-coated, R1.5/1.3 Quantifoil grids (Quantifoil Micro Tools GmbH) were glow-discharged and treated with 5 μL of 10 nm colloidal gold (Ted Pella). Purified protein was diluted to 2 mg/ml in 20 mM potassium phosphate buffer pH 7.0, and additional gold was added. Four-μL samples at 22˚ C were plunge-frozen using a Vitrobot (FEI Company) in 100% humidity using a 3.5 s blot time and a –3 offset. Frozen grids were stored in liquid nitrogen.

Cryo-electron tomography

Grids were mounted into “flip-flop” cartridges (Iancu et al., 2005) and imaged with an FEI Polara FEG TEM cooled by liquid nitrogen. Orthogonal dual-axis tomographic tilt-series from -63° to 63° on both axes in steps of 3° were collected at 300 kV under low dose conditions on a Gatan imaging filter (20 eV slit width) using the UCSF tomography

package (Zheng et al., 2004). The magnification was 27,500 (0.82 nm/pixel), the defocus was –10 μm (first CTF zero at 1/4.5 nm^{-1}), and the total dose per sample was ~ 120 e^-/A^2, distributed according to the 1/cos scheme.

Image Processing

Dual-axis tomograms were reconstructed with IMOD using weighted back-projection (Mastronarde, 1997) and were low-pass filtered to the resolution of the first CTF zero. Individual particles are shown in Fig. II-2. Using the Bsoft package (Heymann, 2001) and the Peach distributed-computing system (Leong et al., 2005), 305 and 42 spherical volumes with radii of 40 nm (including individual PDHC and OGDHC particles, respectively) were extracted from the tomograms, aligned to the low-pass filtered crystal structure of the E2 core from either PDHC (PDB ID #1DPC) (Hendle et al., 1995) or OGDHC (PDB ID #1E2O) (Knapp et al., 1998), averaged, and symmetrized solely to produce the isosurface background of Fig. II-5. Only measured regions of reciprocal space were used to align the particles to the crystal structure (the missing pyramid was excluded in calculations of the cross correlation coefficient). A resolution of 5.5 nm was estimated using Fourier shell correlation (using the 0.5 threshold) by extracting the core from one individual aligned PDHC particle and correlating it with the 2.0 nm low-pass filtered, E2 crystal structure.

Modeling

Amira (Mercury Computer Systems) was used for all surface and volume rendering and segmentation. Individual reconstructions were thresholded to enclose a volume

corresponding to 5.6 MDa, which is the sum of 24 E2 monomers, 16 E1 dimers and 8 E3 dimers. This corresponds to an E1:E2:E3 chain ratio of 4:3:2, which was favored here among the various reported values because it saturates the E1/E3 binding sites and has been indicated by some measurements as the optimal stoichiometry (Bosma et al., 1984; de Kok et al., 1998; Reed et al., 1975). Crystal structures of E1 (PDB ID #1L8A) (Arjunan et al., 2002) and E3 subunits (PDB ID #1EBD) (Mande et al., 1996) were placed within peripheral densities as described. None of the conclusions depended on the exact threshold used because the gradients defining the peripheral densities in the reconstructions were steep and only the center positions of the fit crystal structures (rather than specific orientations) were used in the analysis. VMD (Humphrey et al., 1996) was used to visualize and manipulate the atomic models. Deep View (Guex and Peitsch, 1997) was used to build a hypothetical model of one complete corner of PDHC using the *A. vinelandii* E2 core (PDB ID #1DPC, 56% identity) (Hendle et al., 1995), E3 bound to the E1/E3 binding domain from *B. stearothermophilus* (PDB ID #1EBD, 44% identity) (Mande et al., 1996), the *E. coli* lipoyl domain (PDB ID #1QJO) (Jones et al., 2000), and tether sequences from *E. coli*. The 11 most N-terminal residues present in the *Azotobacter vinelandii* E2 core crystal structure are thought to be part of the 31-residue disordered tether in the *E. coli* complex (Bateman et al., 2004), and so were depicted as such here. One extracted PDHC particle and one OGDHC particle were submitted to the EM Data Bank with the accession codes EMD-1151 and EMD-1152, respectively.

Acknowledgements

We thank T. Wagenknecht and J. Berkowitz for the protein samples, and A. Rawlinson for help preparing the figures. This work was supported in part by NIH Grant PO1 GM66521 to GJJ, DOE grant DE-FG02-04ER63785 to GJJ, the Beckman Institute at Caltech, and gifts to Caltech from the Ralph M. Parsons Foundation, the Agouron Institute, and the Gordon and Betty Moore Foundation.

References

Aevarsson, A., Seger, K., Turley, S., Sokatch, J. R., and Hol, W. G. (1999). Crystal structure of 2-oxoisovalerate and dehydrogenase and the architecture of 2-oxo acid dehydrogenase multienzyme complexes. Nat. Struct. Biol. *6*, 785-792.

Arjunan, P., Nemeria, N., Brunskill, A., Chandrasekhar, K., Sax, M., Yan, Y., Jordan, F., Guest, J. R., and Furey, W. (2002). Structure of the pyruvate dehydrogenase multienzyme complex E1 component from Escherichia coli at 1.85 A resolution. Biochemistry *41*, 5213-5221.

Bateman, A., Coin, L., Durbin, R., Finn, R. D., Hollich, V., Griffiths-Jones, S., Khanna, A., Marshall, M., Moxon, S., Sonnhammer, E. L.*, et al.* (2004). The Pfam protein families database. Nucleic Acids Res. *32*, D138-141.

Baumeister, W., Grimm, R., and Walz, J. (1999). Electron tomography of molecules and cells. Trends Cell Biol. *9*, 81-85.

Bleile, D. M., Munk, P., Oliver, R. M., and Reed, L. J. (1979). Subunit structure of dihydrolipoyl transacetylase component of pyruvate dehydrogenase complex from Escherichia coli. Proc. Natl. Acad. Sci. U.S.A. *76*, 4385-4389.

Boal, D. (2002). Mechanics of the Cell (Cambridge, UK: Cambridge University Press).

Bohm, J., Frangakis, A. S., Hegerl, R., Nickell, S., Typke, D., and Baumeister, W. (2000). Toward detecting and identifying macromolecules in a cellular context: Template matching applied to electron tomograms. Proc. Natl. Acad. Sci. U.S.A. *97*, 14245-14250.

Bosma, H. J., de Kok, A., Westphal, A. H., and Veeger, C. (1984). The composition of the pyruvate dehydrogenase complex from Azotobacter vinelandii. Does a unifying model exist for the complexes from gram-negative bacteria? Eur. J. Biochem. *142*, 541-549.

de Kok, A., Hengeveld, A. F., Martin, A., and Westphal, A. H. (1998). The pyruvate dehydrogenase multi-enzyme complex from Gram-negative bacteria. Biochim. Biophys. Acta *1385*, 353-366.

Frangakis, A. S., Bohm, J., Forster, F., Nickell, S., Nicastro, D., Typke, D., Hegerl, R., and Baumeister, W. (2002). Identification of macromolecular complexes in cryoelectron tomograms of phantom cells. Proc. Natl. Acad. Sci. U.S.A. *99*, 14153-14158.

Green, J. D., Perham, R. N., Ullrich, S. J., and Appella, E. (1992). Conformational studies of the interdomain linker peptides in the dihydrolipoyl acetyltransferase component of the pyruvate dehydrogenase multienzyme complex of Escherichia coli. J. Biol. Chem. *267*, 23484-23488.

Gu, Y., Zhou, Z. H., McCarthy, D. B., Reed, L. J., and Stoops, J. K. (2003). 3D electron microscopy reveals the variable deposition and protein dynamics of the peripheral pyruvate dehydrogenase component about the core. Proc. Natl. Acad. Sci. U.S.A. *100*, 7015-7020.

Guex, N., and Peitsch, M. C. (1997). SWISS-MODEL and the Swiss-PdbViewer: an environment for comparative protein modeling. Electrophoresis *18*, 2714-2723.

Hendle, J., Mattevi, A., Westphal, A. H., Spee, J., de Kok, A., Teplyakov, A., and Hol, W. G. (1995). Crystallographic and enzymatic investigations on the role of Ser558, His610, and Asn614 in the catalytic mechanism of Azotobacter vinelandii dihydrolipoamide acetyltransferase (E2p). Biochemistry *34*, 4287-4298.

Heymann, J. B. (2001). Bsoft: image and molecular processing in electron microscopy. J. Struct. Biol. *133*, 156-169.

Humphrey, W., Dalke, A., and Schulten, K. (1996). VMD: visual molecular dynamics. J. Mol. Graphics *14*, 33-38, 27-38.

Iancu, C. V., Wright, E. R., Benjamin, J., Tivol, W. F., Dias, D. P., Murphy, G. E., Heymann, J. B., and Jensen, G. J. (2005) A "flip-flop" rotation stage for routine dual-axis electron cryotomography. J. Struct. Biol. *151,* 288-297.

Jones, D. D., Stott, K. M., Howard, M. J., and Perham, R. N. (2000). Restricted motion of the lipoyl-lysine swinging arm in the pyruvate dehydrogenase complex of Escherichia coli. Biochemistry *39*, 8448-8459.

Knapp, J. E., Mitchell, D. T., Yazdi, M. A., Ernst, S. R., Reed, L. J., and Hackert, M. L. (1998). Crystal structure of the truncated cubic core component of the Escherichia coli 2-oxoglutarate dehydrogenase multienzyme complex. J. Mol. Biol. *280*, 655-668.

Kürner, J., Medalia, O., Linaroudis, A. A., and Baumeister, W. (2004). New insights into the structural organization of eukaryotic and prokaryotic cytoskeletons using cryo-electron tomography. Exp. Cell Res. *301*, 38-42.

Leong, P. A., Heymann, J. B., and Jensen, G. J. (2005). Peach: A simple Perl-based system for distributed computation and its application to cryoEM data processing. Structure *13*, 1-7.

Mande, S. S., Sarfaty, S., Allen, M. D., Perham, R. N., and Hol, W. G. (1996). Protein-protein interactions in the pyruvate dehydrogenase multienzyme complex: dihydrolipoamide dehydrogenase complexed with the binding domain of dihydrolipoamide acetyltransferase. Structure *4*, 277-286.

Mastronarde, D. N. (1997). Dual-axis tomography: an approach with alignment methods that preserve resolution. J. Struct. Biol. *120*, 343-352.

McIntosh, R., Nicastro, D., and Mastronarde, D. (2005). New views of cells in 3D: an introduction to electron tomography. Trends Cell Biol. *15*, 43-51.

Medalia, O., Typke, D., Hegerl, R., Angenitzki, M., Sperling, J., and Sperling, R. (2002). Cryoelectron microscopy and cryoelectron tomography of the nuclear pre-mRNA processing machine. J. Struct. Biol. *138*, 74-84.

Moe, O. A., Jr., Lerner, D. A., and Hammes, G. G. (1974). Fluorescence energy transfer between the thiamine diphosphate and flavine adenine dinucleotide binding sites on the pyruvate dehydrogenase multienzyme complex. Biochemistry *13*, 2552-2557.

Nitsch, M., Walz, J., Typke, D., Klumpp, M., Essen, L. O., and Baumeister, W. (1998). Group II chaperonin in an open conformation examined by electron tomography. Nat. Struct. Biol. *5*, 855-857.

Oliver, R. M., and Reed, L. J. (1982). Multienzyme Complexes, In Electron Microscopy of Proteins, R. Harris, ed. (London: Academic Press), pp. 1-48.

Perham, R. N. (1991). Domains, motifs, and linkers in 2-oxo acid dehydrogenase multienzyme complexes: a paradigm in the design of a multifunctional protein. Biochemistry *30*, 8501-8512.

Reed, L. J., Pettit, F. H., Eley, M. H., Hamilton, L., Collins, J. H., and Oliver, R. M. (1975). Reconstitution of the Escherichia coli pyruvate dehydrogenase complex. Proc. Natl. Acad. Sci. U.S.A. *72*, 3068-3072.

Sandin, S., Ofverstedt, L. G., Wikstrom, A. C., Wrange, O., and Skoglund, U. (2004). Structure and flexibility of individual immunoglobulin G molecules in solution. Structure *12*, 409-415.

Subramaniam, S., and Milne, J. L. S. (2004). Three-dimensional electron microscopy at molecular resolution. Annu. Rev. Biophys. Biomol. Struct. *33*, 141-155.

Wagenknecht, T., Grassucci, R., Berkowitz, J., and Forneris, C. (1992). Configuration of interdomain linkers in pyruvate dehydrogenase complex of Escherichia coli as determined by cryoelectron microscopy. J. Struct. Biol. *109*, 70-77.

Wagenknecht, T., Grassucci, R., and Schaak, D. (1990). Cryoelectron microscopy of frozen-hydrated alpha-ketoacid dehydrogenase complexes from Escherichia coli. J. Biol. Chem. *265*, 22402-22408.

Walz, J., Tamura, T., Tamura, N., Grimm, R., Baumeister, W., and Koster, A. J. (1997). Tricorn protease exists as an icosahedral supermolecule in vivo. Mol. Cell *1*, 59-65.

Wriggers, W., and Birmanns, S. (2001). Using Situs for flexible and rigid-body fitting of multiresolution single-molecule data. J. Struct. Biol. *133*, 193-202.

Yang, H. C., Hainfeld, J. F., Wall, J. S., and Frey, P. A. (1985). Quaternary structure of pyruvate dehydrogenase complex from Escherichia coli. J. Biol. Chem. *260*, 16049-16051.

Zhao, Q., Ofverstedt, L. G., Skoglund, U., and Isaksson, L. A. (2004). Morphological variation of individual Escherichia coli 30S ribosomal subunits in vitro and in situ, as revealed by cryo-electron tomography. Exp. Cell Res. *297*, 495-507.

Zheng, Q. S., Braunfeld, M. B., Sedat, J. W., and Agard, D. A. (2004). An improved strategy for automated electron microscopic tomography. J. Struct. Biol. *147*, 91-101.

Zhou, Z. H., Liao, W., Cheng, R. H., Lawson, J. E., McCarthy, D. B., Reed, L. J., and Stoops, J. K. (2001a). Direct evidence for the size and conformational variability of the pyruvate dehydrogenase complex revealed by three-dimensional electron microscopy. The "breathing" core and its functional relationship to protein dynamics. J. Biol. Chem. *276*, 21704-21713.

Zhou, Z. H., McCarthy, D. B., O'Connor, C. M., Reed, L. J., and Stoops, J. K. (2001b). The remarkable structural and functional organization of the eukaryotic pyruvate dehydrogenase complexes. Proc. Natl. Acad. Sci. U.S.A. *98*, 14802-14807.

Figures

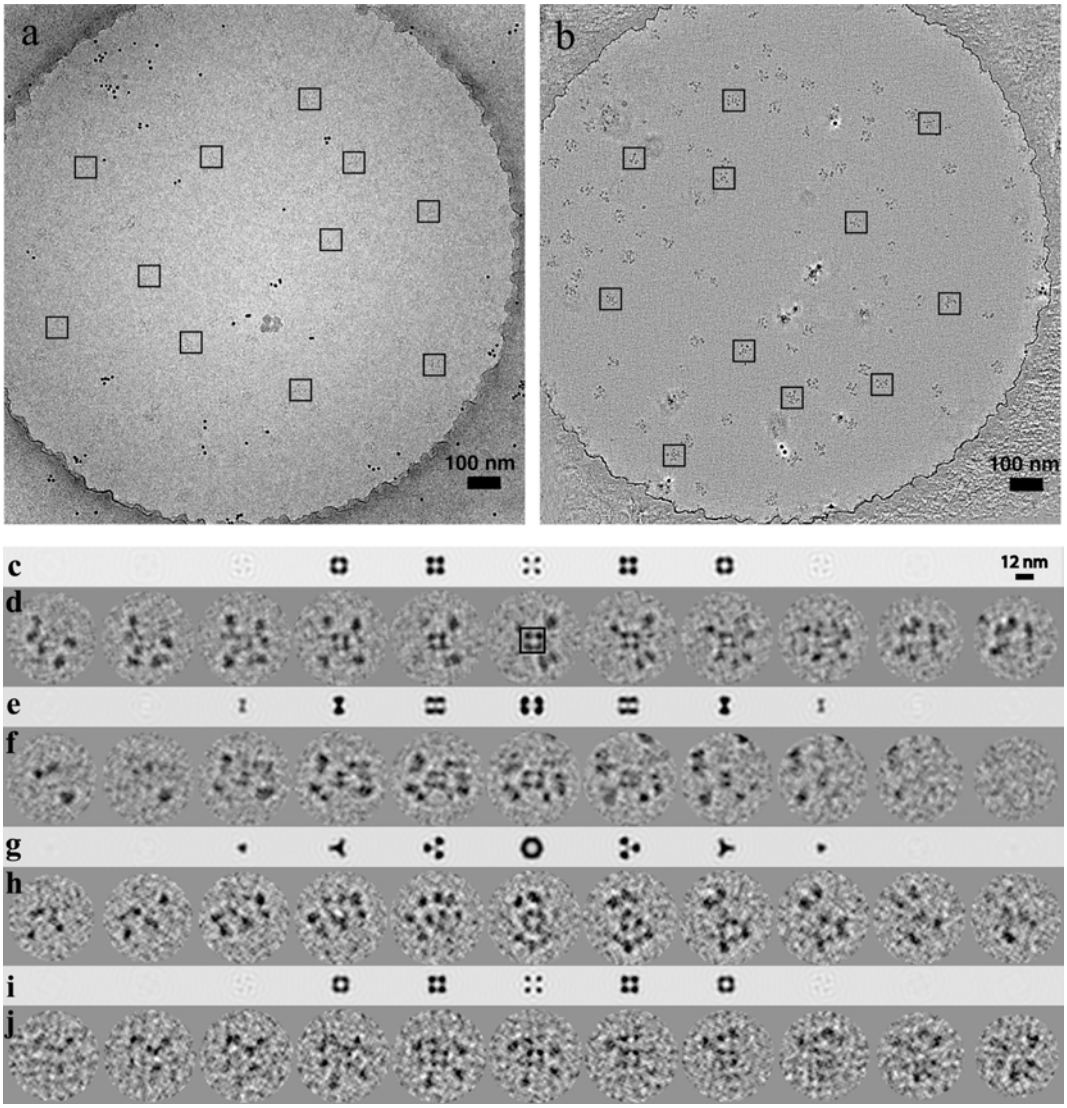

Figure II-1. Raw data and reconstructions

(a) One image from the tomographic tilt series with many PDHC particles boxed in black. The small dark dots are gold fiducials. (b) One 0.82 nm central slice through the three-dimensional reconstruction with particles again boxed. (d, f, h) 2.5 nm thick serial slices through extracted, undenoised PDHC particles that were frozen with their 4-, 2-, and 3-fold axes perpendicular to the plane of the grid, respectively. (c, e, g) 2.5 nm thick

serial slices through a 2.0 nm low-pass filtered map of the E2 crystal structure for comparison, again viewed down the 4-, 2-, and 3-fold axes, respectively. (i, j) Analogous slices through one OGDHC particle frozen with its 4-fold axis perpendicular to the plane of the grid, and its corresponding E2 core crystal structure. A single box drawn in the center of (d) clarifies the region of the reconstructed particles that should be compared to the X-ray structures above. Only in-plane rotations were made to orient the particles in relation to the crystal structure.

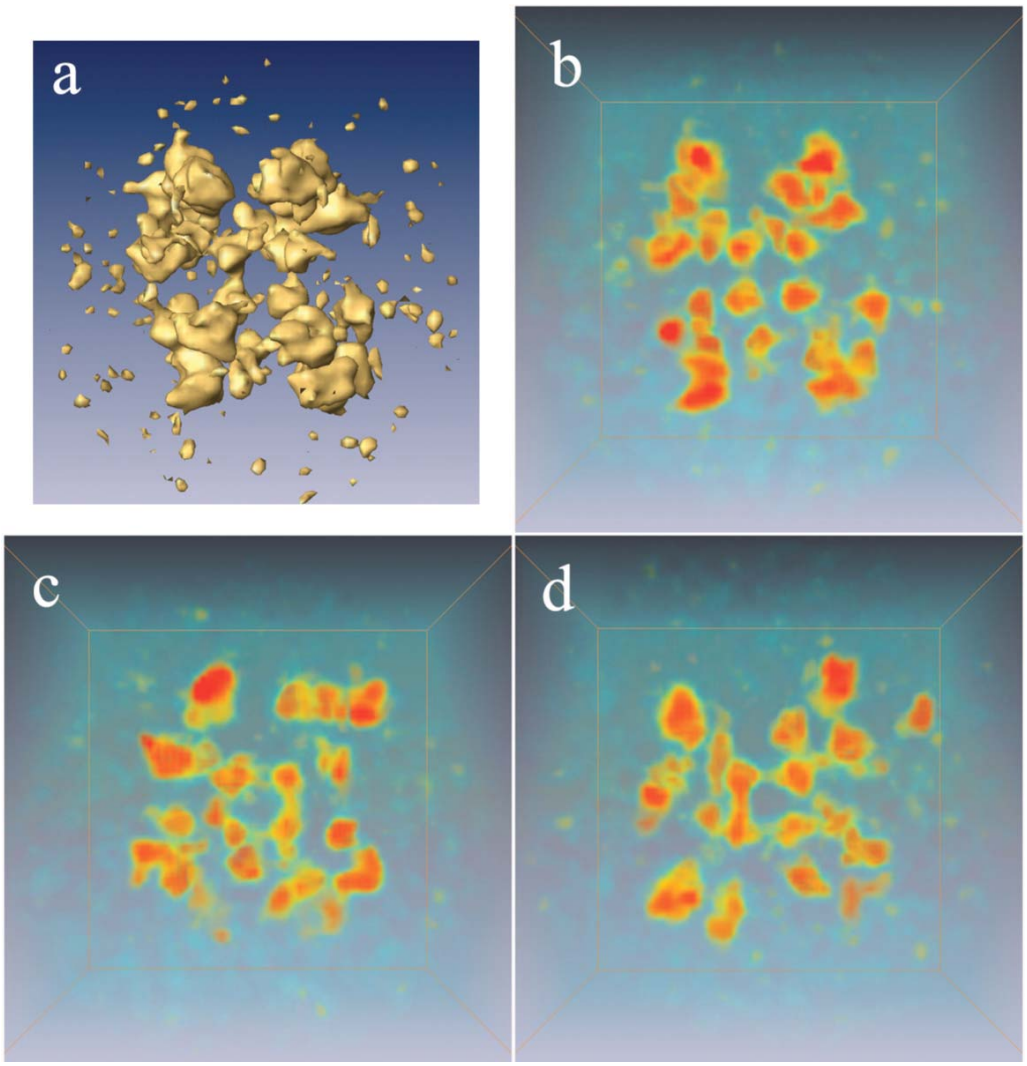

Figure II-2. Particle renderings

(a) Surface rendering of one reconstructed PDHC particle, enclosing the estimated volume of a complete 5.6 MDa complex. (b) Volume rendering of the same particle with the foreground excluded for clarity and to reveal the cubic core. (c-d) Similar volume renderings for two other particles.

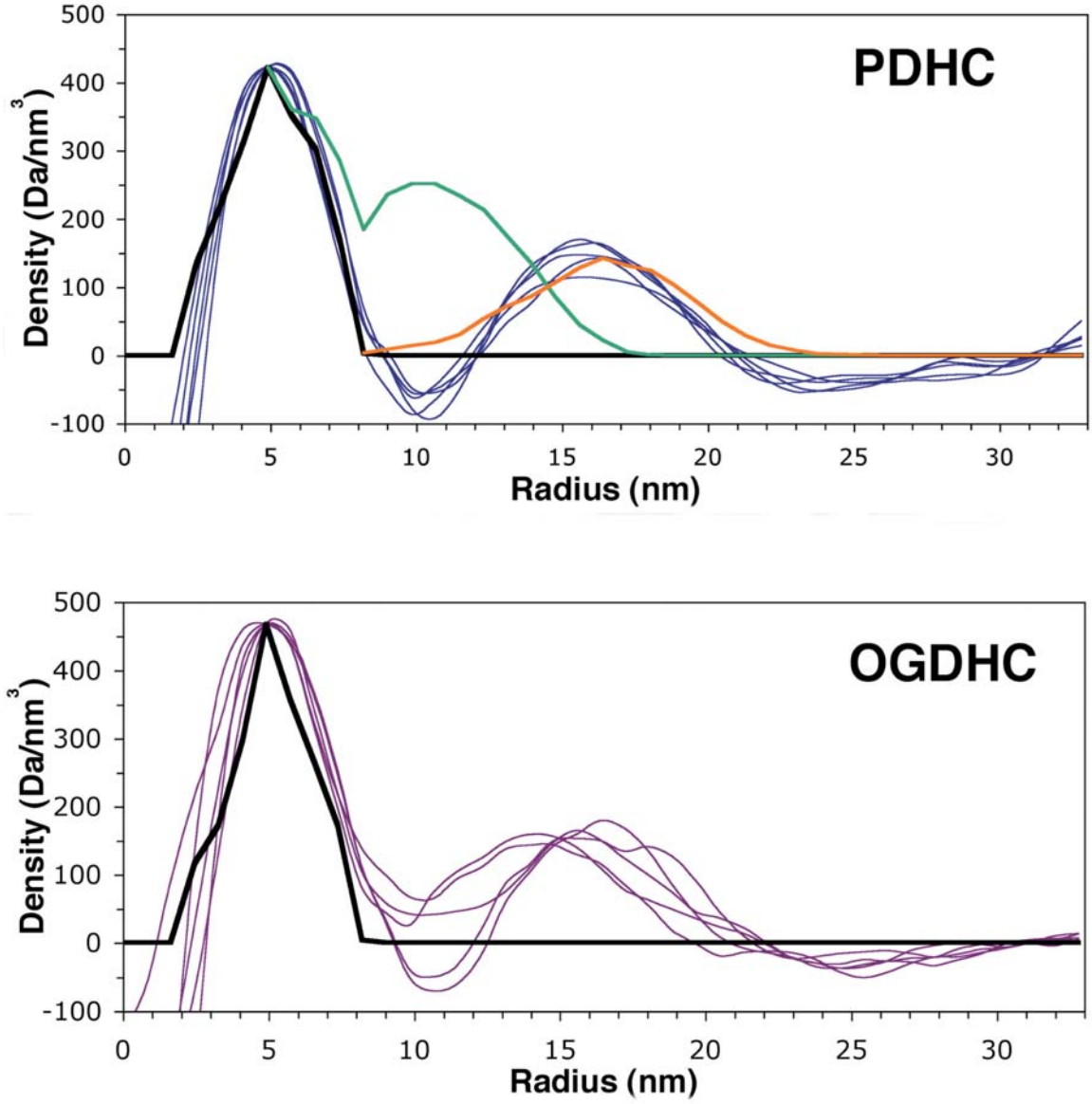

Figure II-3. Radial density plots

Radial density profiles of various atomic models and several reconstructed PDHC (top) and OGDHC (bottom) particles: (blue) five different reconstructed PDHC particles; (purple) five different reconstructed OGDHC particles; (black) the corresponding E2 core crystal structures; (green) face/edge model; (orange) the model produced by manually fitting the atomic structures of E1, E2, and E3 into a single PDHC reconstruction.

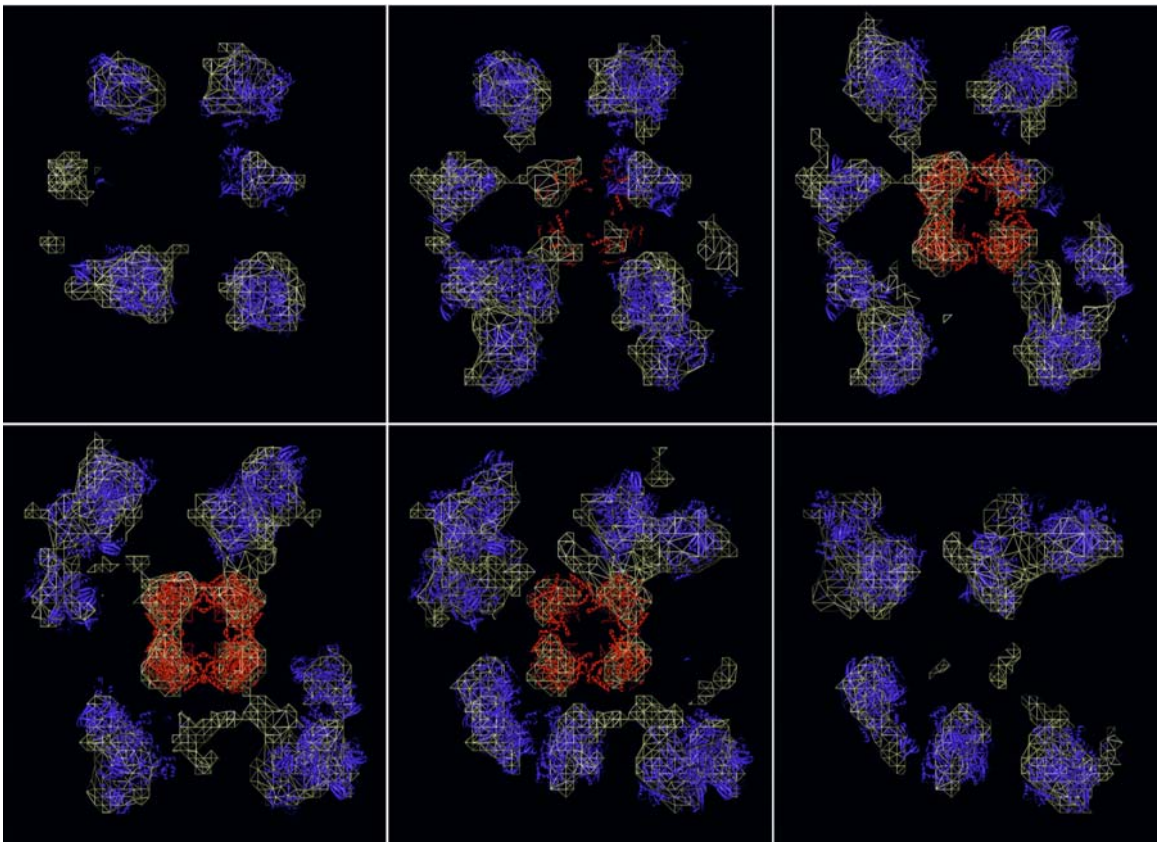

Figure II-4. Resolution as judged by similarity to X-ray crystal structures.

Serial slices through the particle in Fig. II-2a with the roughly fit crystal structures embedded. Crystal structures for the central E2 core and the peripheral E1 or E3 subunits appear in red and blue, respectively. The wire surface again encloses a volume corresponding to a complete complex. The slices are 15 nm thick and overlap each other by 7.4 nm. Note that while the crystal structure of the symmetrically arranged E2 core could be unambigously docked, the resolution was insufficient to distinguish E1 from E3 subunits or their precise orientations. Nevertheless, one set of potential fits are shown to illustrate the clarity of the reconstructions obtained here without any denoising; reconstructed subunits had generally similar sizes and shapes as the crystal structures but could not be docked uniquely.

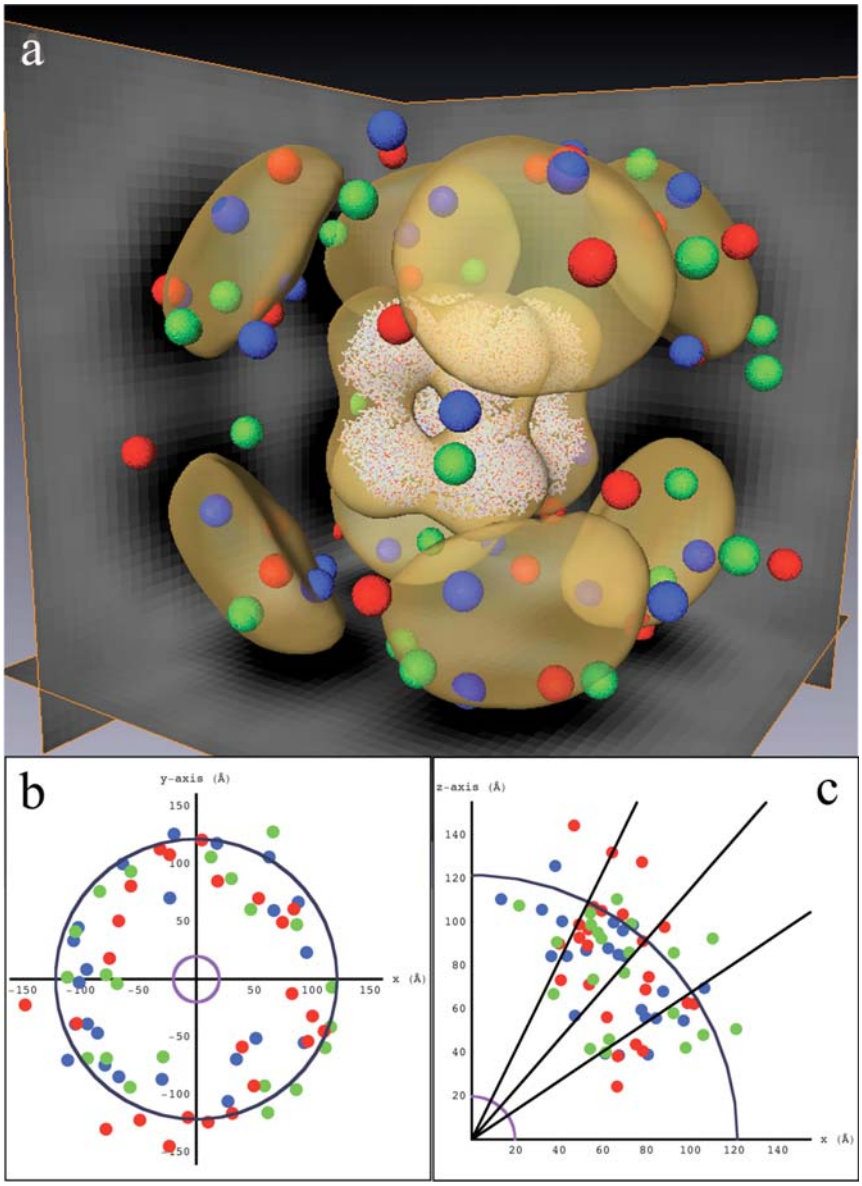

Figure II-5. Random distribution of E1 and E3 around the E2 core

Isosurface of 305 averaged and octahedrally symmetrized reconstructed PDHC particles (yellow), with the E2 crystal structure fit into the core region. Each interpreted E1 or E3 subunit is depicted by a sphere whose radius is approximately one-eighth the true size, colored according to which of the three particles it came from. Individual subunits appear randomly distributed, leading to the amorphous

density directly above the corners of the core in the reconstruction average. (b) Distance and azimuthal angles of the same subunits in relation to their nearest corner. The expected tether lengths of a fully extended polypeptide and a three-dimensional random walk are shown as blue and purple circles, respectively. (c) Distance and polar angles of the centers in relation to their nearest corner, with the same landmark circles as in panel (b). The middle ray depicts the mean polar angle of 41°, while the top and bottom rays delineate the standard deviation of ±15°.

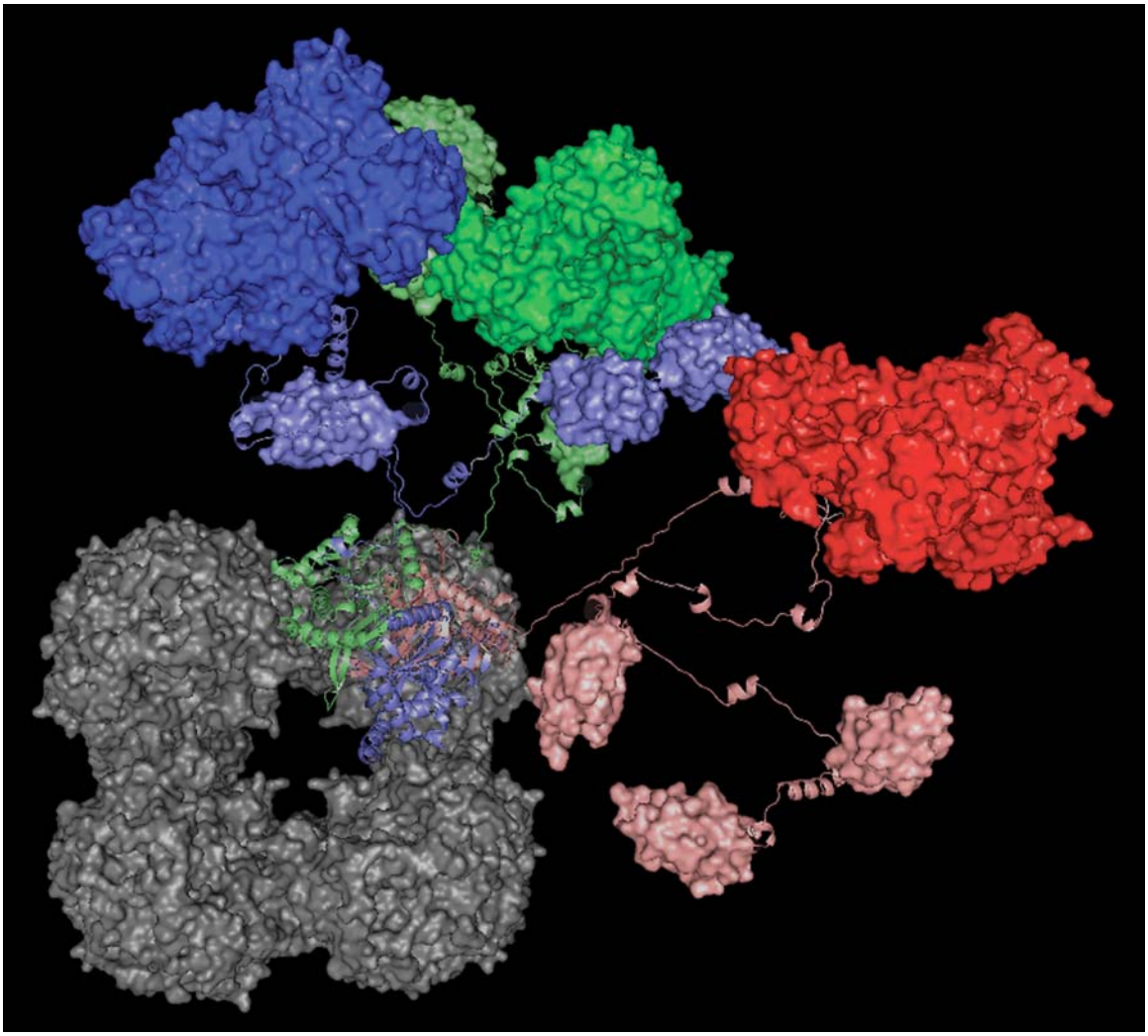

Figure II-6. Complete model of one PDHC corner

One possible conformation of a PDHC corner is depicted. The full E2 core is shown in grey, with the three particular E2 monomers involved in the corner of interest shown in light blue, light green, and pink. Three E3 dimers—correspondingly shown in dark blue, dark green, and red—were positioned according to the density seen above one corner of one particular PDHC reconstruction. The remaining nine lipoyl domains and twelve tethers were placed in reasonable but purely hypothetical positions to provide a sense of the crowdedness in a complete assembly.

Chapter III

In situ structure of the complete *Treponema primitia* flagellar motor

Gavin E. Murphy[1], Jared R. Leadbetter[2], Grant J. Jensen[1*]

Divisions of Biology[1] and Environmental Science and Engineering[2]

California Institute of Technology, Pasadena, CA 91125

*To whom correspondence should be addressed: 1200 E. California Blvd., Pasadena, CA 91125, 626-395-8827 (phone), 626-395-5730 (fax), Jensen@caltech.edu.

Published in Nature 2006 Aug 31; 442 (7106): 1062-4.

doi:10.1038/nature05015

Received 7 April 2006; Accepted 21 June 2006; Published online: 2 August 2006

http://www.nature.com/nature/journal/v442/n7106/full/nature05015.html

The bacterial flagellar motor is an amazing nanomachine: built from about 25 different proteins, it uses an electrochemical ion gradient to drive rotation at speeds of up to 300 Hz[1, 2]. The flagellar motor consists of a fixed, membrane-embedded, torque-generating stator and a typically bidirectional, spinning rotor that changes direction in response to chemotactic signals. While most structural work to date has targeted the purified rotor[3, 4], little is known about the stator and its interactions. Using electron cryotomography of whole cells, here we show the *in situ* structure of the complete flagellar motor from the spirochete *Treponema primitia* at 7 nm resolution. Twenty individual motor particles were computationally extracted from the reconstructions, aligned, and then averaged. The stator assembly, revealed for the first time, possessed 16-fold symmetry and was connected directly to the rotor, C ring, and a novel P-ring-like structure. The unusually large size of the motor suggested mechanisms for increasing torque and supported models wherein critical interactions occur atop the C ring, where our data suggest that both the C-terminal and middle domains of FliG are found.

The bacterial flagellar motor excites considerable interest because of the ordered expression of its genes, its regulated self-assembly, the complex interactions of its many proteins, and its startling mechanical abilities. Stator proteins MotA and MotB form a ring of "studs" within and above the inner membrane that couple the passage of protons across the membrane to the generation of torque[1, 2]. Above the membrane MotB has a peptidoglycan-binding domain that presumably holds the stator in place by binding to the globally cross-linked peptidoglycan layer[1, 2]. Below the membrane, the cytoplasmic loops of MotA are believed to spin a wheel of FliG molecules, which, like radial spokes, extend roughly parallel to the membrane from the rotor in the middle to just below MotA on the periphery[1]. Proteinaceous P and L rings serve as bearings to facilitate the rotation of the rod within the peptidoglycan and outer membranes, respectively[1, 2]. Inside the cell

and below FliG lies the C ring, which regulates the direction of rotation in response to the chemotactic system[1, 2].

Flagellar basal bodies containing the rotor, rod, and sometimes the C ring have been purified and reconstructed by electron cryomicroscopy-based single particle analysis[3, 5, 6]. The *Salmonella* rotor possessed 26-fold symmetry[7] while the *Salmonella* C ring possessed a mean symmetry of 34[8]. Because the stators do not co-purify with the rotor, however, little is known about their structure and interactions with the rest of the motor. Patterns of stator studs have been seen in 2D, freeze-etch images, but the interpretation of these images is difficult and the number of studs has been reported as either 12 or 16, depending on the species[9-12]. 2-D cryo-EM images of purified PomA/PomB complexes (homologs of MotA and MotB) from *V. alginolyticus* have revealed an ~ 70 Å long, thin extension above the membrane[13].

Here we report the complete structure of the flagellar motor, including the stators, obtained by electron cryotomography. Fifteen *T. primitia* cells frozen within thin layers of vitreous ice were imaged (Fig. III-1a, and Methods section). *T. primitia* was chosen for its narrow diameter and interesting periplasmic flagella that emerge from each pole. Twenty motor particles were computationally extracted from the reconstructions, mutually aligned, and averaged (Figures III-1b–e). In both individual maps (Fig. III-1d) and their average (Fig. III-1e), the stator studs were clearly sixteen-fold symmetric around the rod. We checked for symmetry computationally in the other components including the P-collar (the density above the stator as explained below), the rotor, the connections between the stators and C ring, and the C ring itself (Supplementary Fig. III-S1a and b). Presumably because of the limited resolution, only the symmetry of the stators and their connections to the C ring was apparent. This symmetry was therefore

imposed on the entire motor, effectively smoothing the other components (Supp. Fig. III-S1c and d).

For the first time, the 3-D structure of the stators was revealed in their natural position in contact with the membrane and other motor components (Fig. III-2 and Supplementary Movie). The 16 stator studs (two of which are identified by asterisks in Fig. III-2c) were 8 nm wide, which is similar to the reported values of 5–7 nm seen by other means[9, 10, 12]. Surprisingly, the volume of each stud above the membrane was ~ 20 times larger than that expected for two MotB peptidoglycan binding domains and much thicker than PomA/PomB resuspended in liposomes[13]. The identity of the rest of the stator density is unclear. The studs were spaced 7 nm apart, which is sufficient to accommodate hypothetical models for the 18 transmembrane helices in a $MotA_4MotB_2$ torque-generating unit[14]. The average stud was not vertical—instead, it leaned (dotted line in Fig. III-2a) such that its distal end was positioned clockwise relative to the proximal end as viewed from inside the cell. There were thin bridging densities connecting the stud heads around the ring (arrowhead in Fig. III-2c).

Four bridging densities (numbered in Fig. III-2b) were seen connecting the stator ("S" in Fig. III-2b) to other components of the motor (see Supp. Fig. III-S2 for contour, variance, and statistical significance maps). Bridging density #1 connected the stator to the C ring ("C" in Fig. III-2b). It is thought that a series of charged residues in a cytoplasmic loop of MotA interacts here with complementary charges in the C-terminal domain of FliG[1]. The stator-C-ring connections were also rotated with respect to the periplasmic studs, suggesting that they might perhaps be the terminus of a ~ 24 nm long and straight component that extended from the peptidoglycan layer all the way through the membrane to the C ring (see again dotted line in Fig. III-2a). Bridging densities #2 and #3 were finger-like extensions connecting the stator directly to the rotor.

Bridging density #4 linked the stator to a contrast-rich ring of density ("P" in Fig. III-2b) encircling the rod above the rotor reminiscent of the P- and L-ring bushings in *Salmonella* and *E. coli*. Sequenced *Treponema* flagellar proteins are similar to the better known *Salmonella* and *E. coli* versions (see Supplementary Data), except that the genes for the P and L ring proteins FlgI and FlgH are missing[15]. The absence of an L-ring is understandable because *Treponema*'s periplasmic flagella never exit the outer membrane, and not surprisingly, isolated *Treponema* basal bodies lack any ring structures[16]. In our *in situ* reconstructions, however, an additional ring was seen just above the stators at the level of the peptidoglycan layer, but ~ 8 nm away (surface to surface) from the rod itself. We therefore refer to it as the "P-collar" to reflect its position and loose fit around the rod, though the gene responsible for this density is unknown. This structure may serve to limit the tilt of the flagellar hook and may also further stabilize the stators.

The rotor itself ("R" in Fig. III-2b) was bowl-shaped. Unlike previous work on the isolated basal body, in which the membrane location was not certain[3, 7], here the bulk of the rotor was seen to lie just beneath the inner membrane ("IM" in Fig. III-2b) submerged within the C ring. At the bottom of the rotor there was a small ring (arrow in Fig. III-2d) that formed a funnel-like pore, which may perhaps be the insertion apparatus through which flagellin monomers are exported. Another contrast-rich density with low variance (See Supplementary Figure III-S2) was visible 4 nm below the pore and because of its proximity, has been labeled an export bundle ("E" in Fig. III-2b).

In comparison to isolated *Salmonella* basal bodies, which have been reconstructed to higher resolution by single particle analysis[3, 5], the *Treponema* stud ring, C ring, and rotor are all much larger (Fig. III-3). The rotor is also located lower within the C ring and appears bowl-shaped rather than disk-like. Interestingly, by stereo-photogrammetry the *Salmonella* rotor also appeared bowl-shaped *in situ*[17], so the shape may depend on

conditions lost during purification. The *Caulobacter* rotor has also appeared bowl-shaped in some reconstructions[6]. Other structural details are remarkably conserved, such as the small gap between rotor and rod (arrows in Fig. III-3c and III-3d).

These differences have important implications for current models of the functional and architectural relationships of the components. While the *Salmonella* motor spins just the flagellum, because *Treponema* flagella are periplasmic, it is thought that they cause the whole cell to gyrate[18]. Thus each rotation may be much slower and require greater torque. The unusually large stud ring, C ring, and rotor in *Treponema* may serve to increase torque by increasing the length of the effective lever arm through which each stator stud acts. These larger rings may also accommodate more stator studs and FliG molecules around the ring, in effect "gearing down" the *Treponema* motor so that the passage of each proton across the membrane produces a smaller angular rotation.

FliG is thought to have three domains: a C-terminal domain directly underneath the stator that forms the top of the C ring, a middle-domain whose location is uncertain, and an N-terminal region bound to the rotor[1, 2, 4, 19, 20]. In our reconstructions, the stator-C-ring connection appears on the outside edge of the C ring, and the distance between the C ring and the rotor is too large to be spanned by the 2 nm long alpha helix connecting FliG's C-terminal and middle domains (see Supplementary Data and starred gap in Fig. III-3). The simplest interpretation of these results is that the C-terminal domain forms the outside edge of the C ring; both the C-terminal and middle domains of FliG lie atop the C ring, and a portion of the N-terminus acts as an extended tether spanning the gap to the rotor, as argued elsewhere[19, 20]. It is interesting to note that while the diameters of the stud and C rings in *Treponema* are unusually large, nevertheless they still match, so that the studs appear directly above the C ring. The available data suggest that the same relationship holds in other, smaller motors as well [3, 11], supporting the idea that this

juxtaposition is important and that key functional interactions do indeed occur at this interface.

Methods

Exponential phase cultures of *T. primitia* strain ZAS-2[21] were plunge frozen with gold fiducial markers across EM grids in liquid ethane. *T. primitia* is an obligate anaerobe but can tolerate atmospheric conditions for about 20 minutes, so grids were frozen quickly in small batches. Single-axis tilt series were acquired automatically on a 300 keV FEI Polara FEG TEM. The 20 averaged motors were taken from tilt-series with underfocuses between 10 and 18 μm (first CTF zero between 4.5 and 6.0 nm^{-1}). Tomograms were low-pass filtered at the resolution of the first CTF zero and binned once (1.96 nm/pixel). No other CTF corrections were performed.

Twenty motor particles were computationally extracted from the tomograms and aligned to an arbitrarily chosen reference particle. The aligned motors were then averaged and rotated so the rod axis corresponded to the z-axis. To detect the symmetry of the components, annular masks were generated for the five different motor regions (shown in Supp. Fig. III-S1b), and then applied separately to all twenty individual particles. The only detectable symmetry in the rotational power spectrum (16-fold) was found in the two stator regions (periplasmic and cytoplasmic), so this was applied to the entire averaged motor. This initial symmetrized average was used as a reference for a further alignment, and the process was iterated a total of five times. To test potential reference bias, two alternate particles were used as a reference, and the resulting average was essentially identical. A resolution of 7 nm was estimated by separately averaging and symmetrizing two halves of the data set and correlating them using Fourier shell correlation with a threshold of 0.5. The isosurface was contoured at a level that showed the connections between stator and C ring.

References

1. Kojima, S. & Blair, D. F. The bacterial flagellar motor: structure and function of a complex molecular machine. *Int. Rev. Cytol.* **233**, 93-134 (2004).

2. Berg, H. C. The rotary motor of bacterial flagella. *Annu. Rev. Biochem.* **72**, 19-54 (2003).

3. Francis, N. R., Sosinsky, G. E., Thomas, D. & DeRosier, D. J. Isolation, characterization and structure of bacterial flagellar motors containing the switch complex. *J. Mol. Biol.* **235**, 1261-70 (1994).

4. Thomas, D., Morgan, D. G. & DeRosier, D. J. Structures of bacterial flagellar motors from two FliF-FliG gene fusion mutants. *J. Bacteriol.* **183**, 6404-12 (2001).

5. Sosinsky, G. E., Francis, N. R., Stallmeyer, M. J. & DeRosier, D. J. Substructure of the flagellar basal body of *Salmonella typhimurium*. *J. Mol. Biol.* **223**, 171-84 (1992).

6. Stallmeyer, M. J., Hahnenberger, K. M., Sosinsky, G. E., Shapiro, L. & DeRosier, D. J. Image reconstruction of the flagellar basal body of *Caulobacter crescentus*. *J. Mol. Biol.* **205**, 511-8 (1989).

7. Suzuki, H., Yonekura, K. & Namba, K. Structure of the rotor of the bacterial flagellar motor revealed by electron cryomicroscopy and single-particle image analysis. *J. Mol. Biol.* **337**, 105-13 (2004).

8. Young, H. S., Dang, H., Lai, Y., DeRosier, D. J. & Khan, S. Variable symmetry in *Salmonella typhimurium* flagellar motors. *Biophys. J.* **84**, 571-7 (2003).

9. Khan, S., Dapice, M. & Reese, T. S. Effects of mot gene expression on the structure of the flagellar motor. *J. Mol. Biol.* **202**, 575-84 (1988).

10. Khan, S., Ivey, D. M. & Krulwich, T. A. Membrane ultrastructure of alkaliphilic *Bacillus* species studied by rapid-freeze electron microscopy. *J. Bacteriol.* **174**, 5123-6 (1992).

11. Khan, S., Khan, I. H. & Reese, T. S. New structural features of the flagellar base in *Salmonella typhimurium* revealed by rapid-freeze electron microscopy. *J. Bacteriol.* **173**, 2888-96 (1991).

12. Coulton, J. W. & Murray, R. G. Cell envelope associations of *Aquaspirillum serpens* flagella. *J. Bacteriol.* **136**, 1037-49 (1978).

13. Yonekura, K. et al. Electron Cryomicroscopic Visualization of PomA/B Stator Units of the Sodium-driven Flagellar Motor in Liposomes. *J. Mol. Biol.* **357**, 73-81 (2006).

14. Braun, T. F., Al-Mawsawi, L. Q., Kojima, S. & Blair, D. F. Arrangement of core membrane segments in the MotA/MotB proton-channel complex of *Escherichia coli*. *Biochemistry* **43**, 35-45 (2004).

15. Limberger, R. J. The periplasmic flagellum of spirochetes. *J. Mol. Microbiol. Biotechnol.* **7**, 30-40 (2004).

16. Jackson, S. & Black, S. H. Ultrastructure of *Treponema pallidum* Nichols following lysis by physical and chemical methods. II. Axial filaments. *Arch. Mikrobiol.* **76**, 325-40 (1971).

17. Katayama, E., Shiraishi, T., Oosawa, K., Baba, N. & Aizawa, S. Geometry of the flagellar motor in the cytoplasmic membrane of *Salmonella typhimurium* as determined by stereo-photogrammetry of quick-freeze deep-etch replica images. *J. Mol. Biol.* **255**, 458-75 (1996).

18. Charon, N. W. & Goldstein, S. F. Genetics of motility and chemotaxis of a fascinating group of bacteria: the spirochetes. *Annu. Rev. Genet.* **36**, 47-73 (2002).

19. Brown, P. N., Hill, C. P. & Blair, D. F. Crystal structure of the middle and C-terminal domains of the flagellar rotor protein FliG. *EMBO J.* **21**, 3225-34 (2002).

20. Lowder, B. J., Duyvesteyn, M. D. & Blair, D. F. FliG subunit arrangement in the flagellar rotor probed by targeted cross-linking. *J. Bacteriol*. **187**, 5640-7 (2005).

21. Leadbetter, J. R., Schmidt, T. M., Graber, J. R. & Breznak, J. A. Acetogenesis from H2 plus CO2 by spirochetes from termite guts. *Science* **283**, 686-9 (1999).

Supplementary information is linked to online versions of the paper at www.nature.com/nature.

Acknowledgements We thank Eric Matson for growing the *T. primitia* cultures. This work was supported in part by NIH grants P01 GM66521 and R01 AI067548 to G.J.J., DOE grant DE-FG02-04ER63785 to G.J.J., a Searle Scholar Award to G.J.J., NSF grant DEB-0321753 to J.R.L., NIH graduate fellowship F31 EB 004179 to G.E.M. and gifts to Caltech from the Ralph M. Parsons Foundation, the Agouron Institute, and the Gordon and Betty Moore Foundation.

Author Contributions G.E.M. collected/analysed the data and drafted the text and figures; J.R.L. provided cells and discourse and G.J.J. guided the research and manuscript editing throughout.

Author Information The averaged and symmetrized structure has been deposited in the EM Data Bank (http://www.ebi.ac.uk/msd/index.html) with the accession code EMD-4663. Reprints and permissions information is available at npg.nature.com/reprintsandpermissions. Address correspondence to G.J.J. at jensen@caltech.edu.

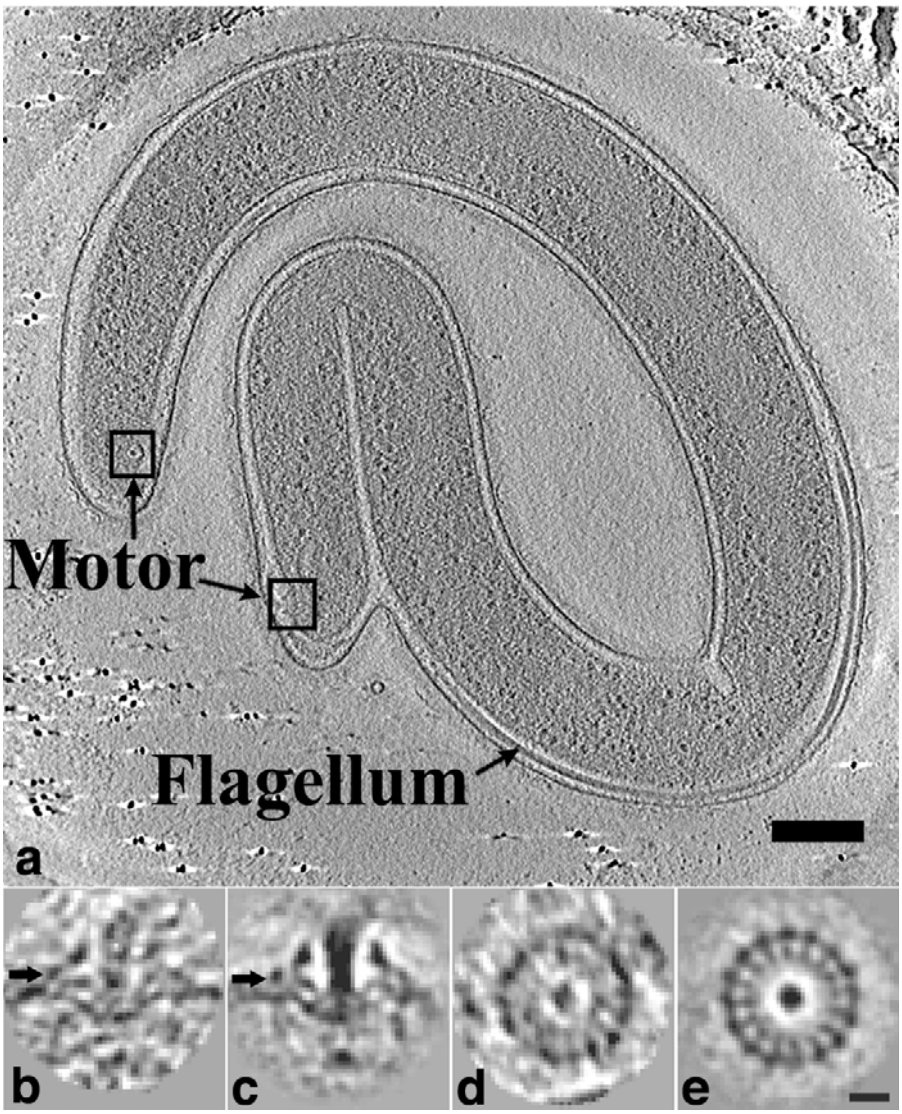

Figure III-1. Electron cryotomography of *T. primitia* and its periplasmic flagellar motor.

a) 2 nm thick central section through a tomogram of an entire *Treponema* cell. A flagellar motor is located near each cell tip and the flagella rotate in the periplasm (scale bar 200 nm). **b**) Axial slice through the center of one extracted motor particle. **c**) Axial slice through the average of twenty motor particles. **d**) Radial slice through the stator region of the same particle shown in **b**, taken at the

height indicated by the arrow. **e**) Radial slice through the average motor, taken at the height indicated by the arrow in **c** (scale bar 20 nm, for **b**-**e**).

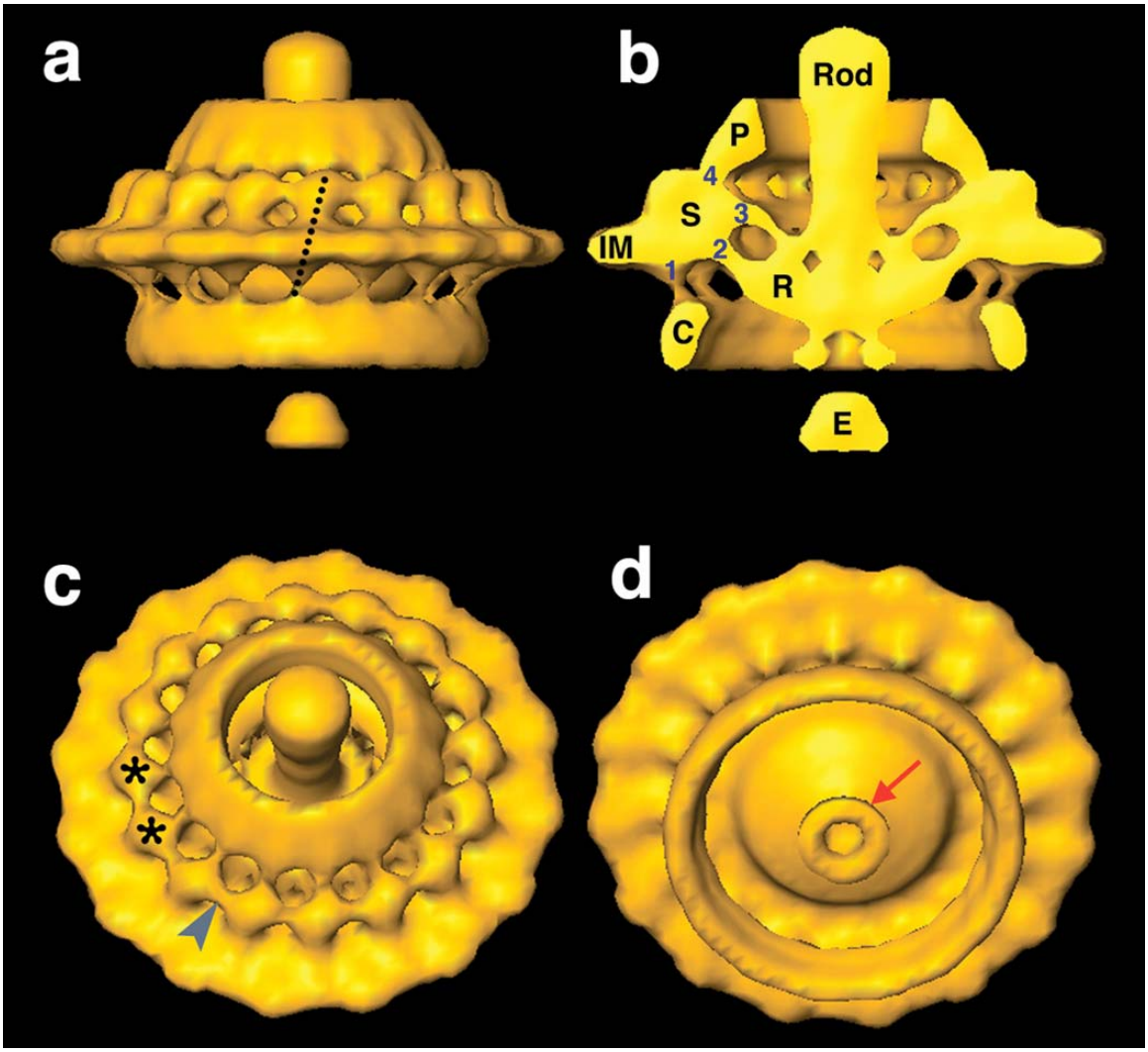

Figure III-2. Isosurface of the symmetrized average flagellar motor.

a) Side view. The dotted line indicates the tilt of the stators with respect to the membrane. **b**) Cutaway of the motor in the same orientation. The stators (S) are embedded in the inner-membrane (IM) and directly contact the C ring (C) (#1), the rotor (R) (#2 and #3) and the P-collar (P) (#4). A rod extends from the rotor, and a bundle (E) lies under the rotor's pore. **c**) Oblique view of the motor's top from within the periplasm. Note the arrangement of the stator studs (asterisks)

and their linkages (arrowhead). **d**) Oblique view of the motor's bottom from within the cytoplasm, with the bundle removed to reveal the pore ring (arrow).

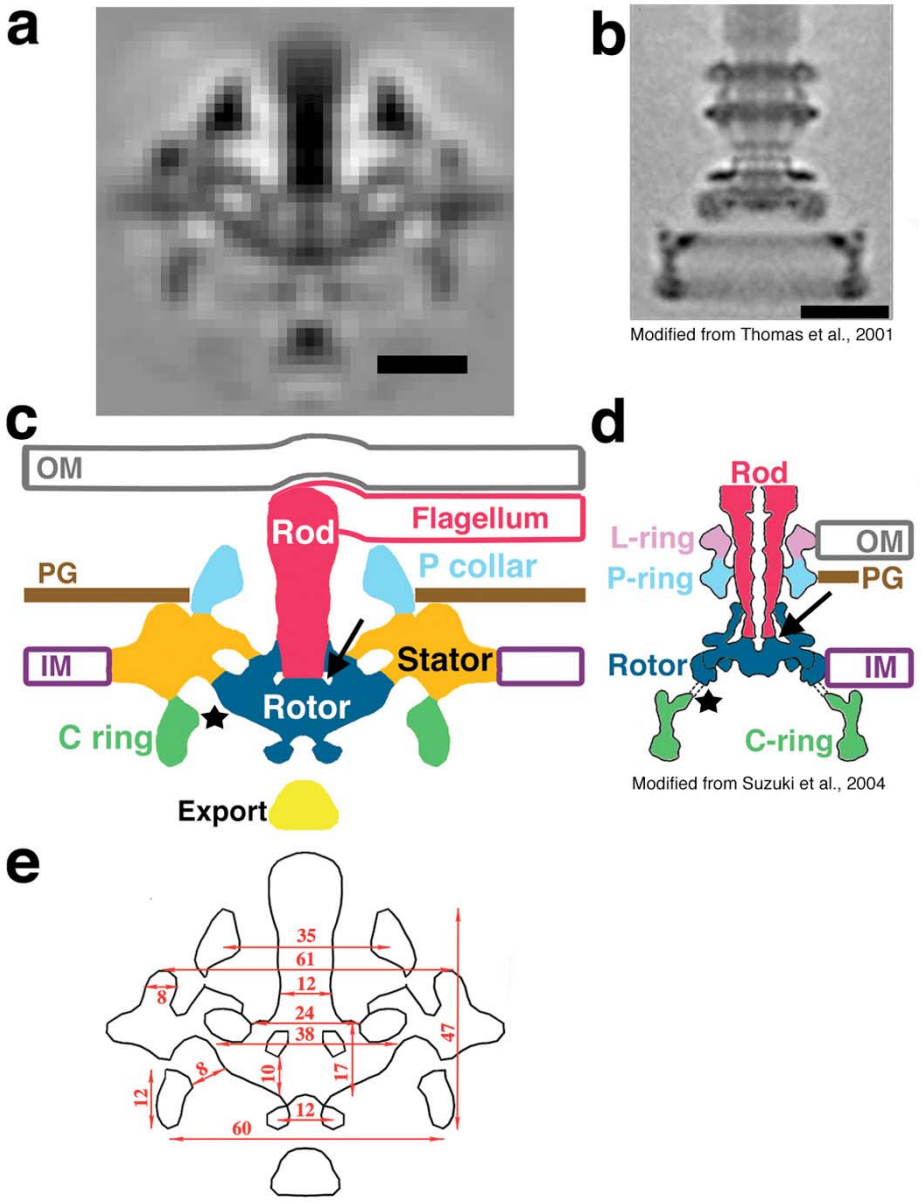

Figure III-3. The *Treponema* motor and its comparison to the *Salmonella* basal body.

All objects are at the same scale. **a**) Axial slice through the *Treponema* flagellar motor (scale bar 20 nm). **b**) Projection of the 3-D reconstruction of the *Salmonella* basal body (scale bar 20 nm). **c**) Cartoon interpretation of the *Treponema* motor with its components labeled. The arrows here and in panel **d**

point to the gap between the rotor and rod, while the stars indicate the gap between the C ring and rotor. The location of the peptidoglycan layer (PG) is conjectured. The outlined objects' locations are approximate. The flagellum actually bends more gradually over the P-collar in presumably random directions but appears straight when averaged. The inner membrane and outer membrane (OM) both bulge more widely around the motor *in situ* than is pictured. **d**) Cartoon of the *Salmonella* basal body for comparison. **e**) Measurements of various motor features.

Supplementary Information

Supplementary Figures

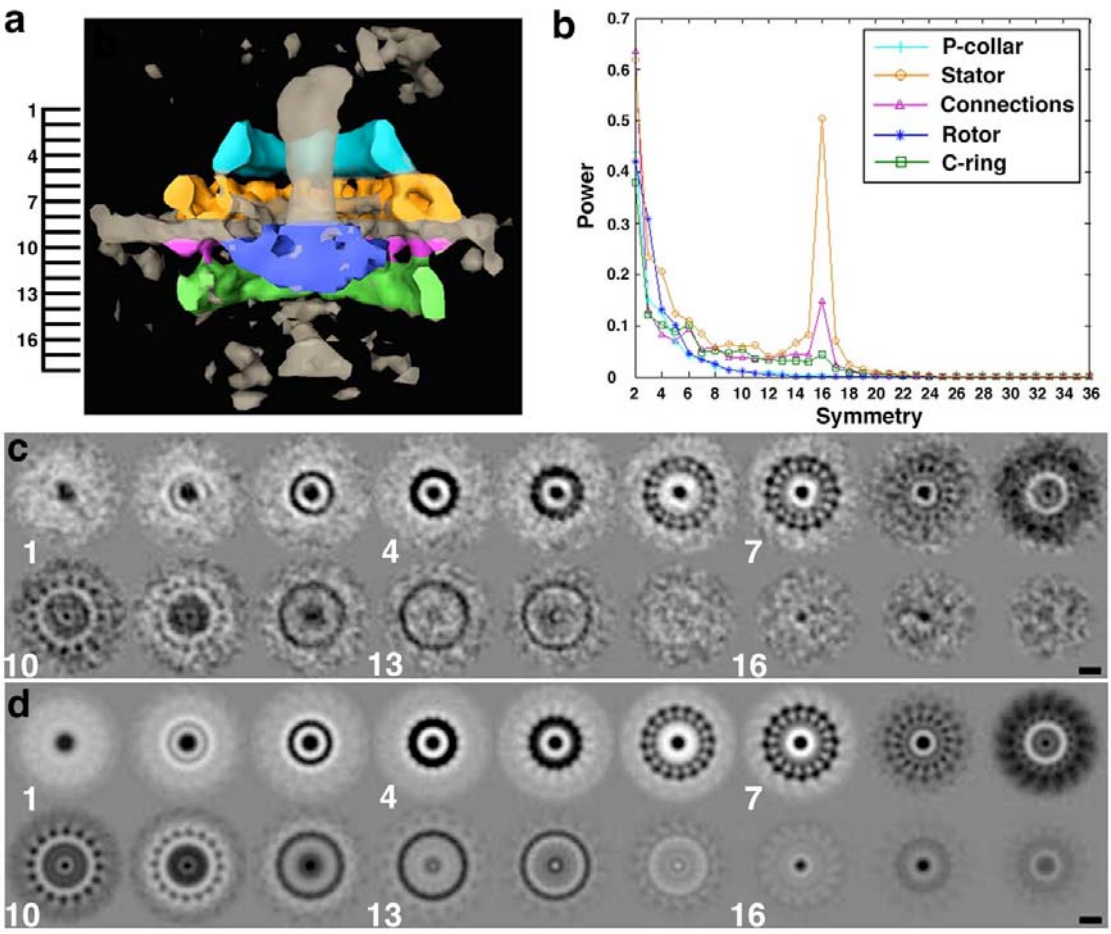

Figure III-S1. Symmetry of the motor components and 3.9-nm thick serial sections.

a) To detect the symmetry of the components in the average, annular masks were generated for the five different motor regions shown in the panel and then applied separately to all twenty individual particles. The regions that were not analyzed for symmetry are grey and transparent. The ruler on the left marks the heights of the radial sections shown in **c** and **d**. **b**) Rotational correlation coefficients were calculated by rotating each of the 100 objects (5 regions of 20 different motors) in 1° steps 360° around the z-axis and calculating the 3-D cross-correlation coefficient with the unrotated object.

The results were Fourier transformed in 1-D to produce rotational power spectra (one for each component of each motor), and then the average power spectrum for each component was plotted, as shown in the panel. The only symmetry detected was the 16-fold symmetry within the stator ring, so this symmetry was imposed on the entire motor, effectively smoothing the other components. **c)** Sections through the average motor. (Section 9 is through the membrane.) **d)** Sections through the symmetrized average. Note the symmetry of the stators both below (sections 10–11) and above (sections 6–8) the membrane (scale bar 20 nm, for **b** and **c**).

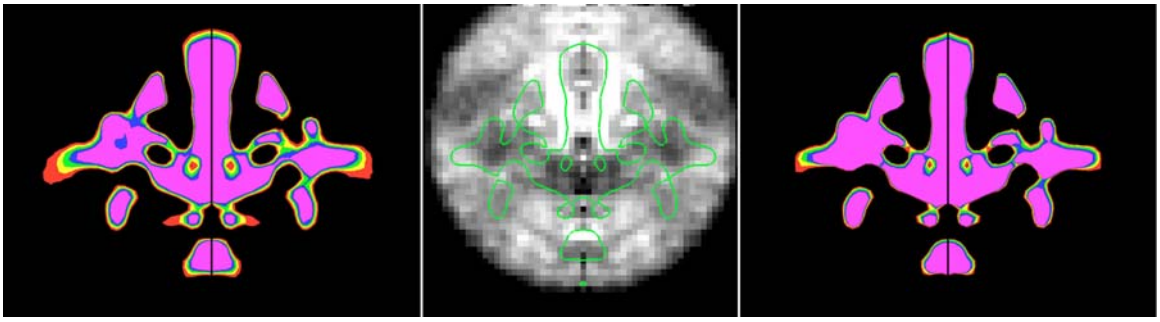

Figure III-S2. Significance maps.

a) An axial cutaway of the symmetrized average map contoured at various levels. Because the connections are not all coplanar, the left and right halves of the figure actually show different planes. The left half shows the plane that bisects connection #4 (see Fig. III-2 for numbering), while the right half bisects connection #1. The density threshold at which surface renderings of electron cryotomography maps should be contoured is usually unclear. The isosurfaces in Fig. III-2 correspond to 0.95 standard deviations above the mean. This value was chosen as the tightest contour that still manifests the connection between the stator assembly and the C ring known to exist from previous work[1]. Here four additional contours are shown as well. The colors red, yellow, green, blue and pink correspond to 0.45, 0.75, 0.95, 1.2, and 1.45 times the standard deviation, respectively. The steepest density gradients exist along the edges of the rod, while the most gradual occur at the edge of the stator assembly where the membranes of the individual motors continue outwards with somewhat variable curvature. The order of the connections in terms of density are, from largest to smallest, #2, #1 and #4, and finally #3. **b)** A 2 nm thick, axial section of the symmetrized variance map with the outline of the motor superimposed (at the favored, 0.95 standard deviation contour level, colored again in green). The highest variances occur around the

rod, as expected, since the rods in each individual motor emerge at different angles, bending over against the P-collar and underneath the outer membrane. The next highest variances are in the cytoplasm underneath the rotor. Some variance is seen in the regions of the connections, as well as on the top face of the export bundle. The rotor and stator stud regions of the map have the least variance. **c)** An axial cutaway of a symmetrized significance map, generated by subtracting from the normally distributed average map the product of 2.093 times the standard error map, which corresponds to the lower boundary of the "95% confidence" interval of a two-tailed student t-test for a sample size of 20[22]. The colors red, yellow, green, blue, and pink correspond to thresholds of 0.31, 0.41, 0.51, 0.61, and 0.71 times this map's standard deviation, respectively. The middle threshold (0.51, green) was chosen to again enclose the same favored volume as the isosurface in Fig. III-2. While the absolute numerical confidence level is not known because the "correct" threshold is still somewhat arbitrary, the order of the connections, in terms of significance from greatest to least, is #4, #1, #2, and finally #3, which alone lacks some connecting density at the favored threshold.

Supplementary figures III-S3–S5 show sequence alignments for the three key motor proteins FliG, MotA, and MotB, which argue that their domain structure is conserved throughout bacteria. Though *Treponema primitia* strain ZAS-2 has not been sequenced, its 16S rRNA shares 86% and 85% sequence identity with that of *T. pallidum* and *T. denticola*, respectively. Thus the structural inferences about the positions, sizes, and interactions of their domains made here based on our *T. primitia* reconstruction are likely generally applicable. The organisms compared are the Gammaproteobacteria *E. coli* and *Salmonella typhimurium*; the Betaproteobacteria *Bordetella bronchiseptica*; the

Spirochetes *Treponema denticola*, *Treponema pallidum*, *Leptospira interrogans*, and *Borrelia burgdorferi*; the Firmicute *Bacillus subtilis*; *Thermotoga maritima*; the Epsilonproteobacteria *Helicobacter pylori*; the Deltaproteobacteria *Geobacter sulfurreducens*; and the Alphaproteobacteria *Agrobacterium tumefaciens*, except that in Fig. III-S3, *Agrobacterium tumefaciens* has been replaced with *Caulobacter crescentus*. Amino acids with 50% conservation are shaded in gray while those with 100% identity are shaded in black. The sequences were aligned with ClustalW[23] and presented using Alscript[24].

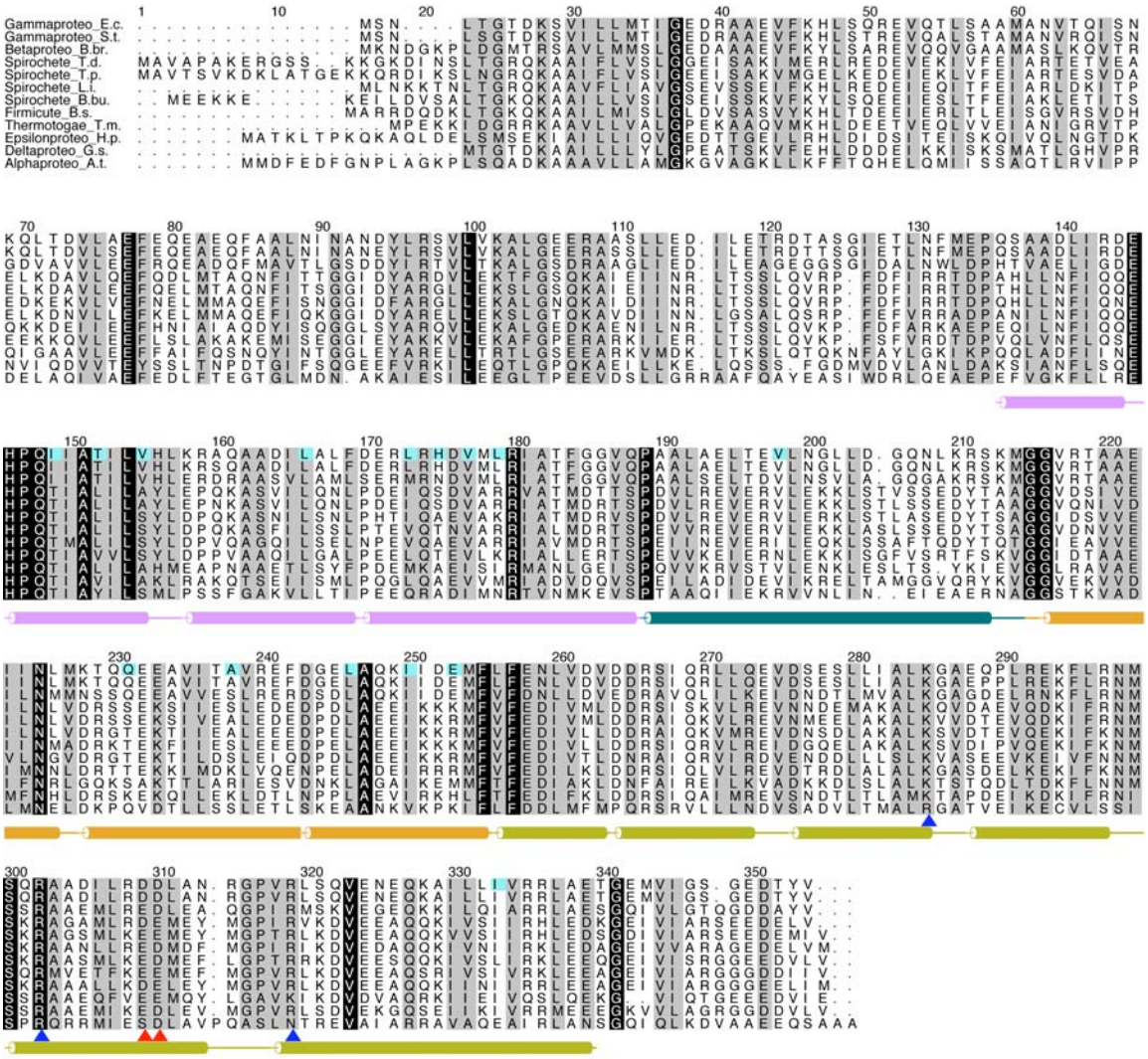

Figure III-S3. Sequence alignment of FliG.

The colored alpha-helices below the sequences are from the crystal structure of *T. maritima's* middle and C-terminal domains of FliG[19]. The pink region corresponds to the middle domain; the blue region corresponds to the 2 nm long helix that bridges the middle and C-terminal domains, and the orange and green regions correspond to the C-terminal domain. Amino acids shaded in cyan are those which, when mutated in *E. coli*, caused reduced binding to FliM in yeast 2-hybrid studies[25]. Notice they occur in both domains. The blue-colored and red-colored arrowheads are the conserved positively or

negatively charged amino acids that interact with the oppositely charged residues of MotA.[1]

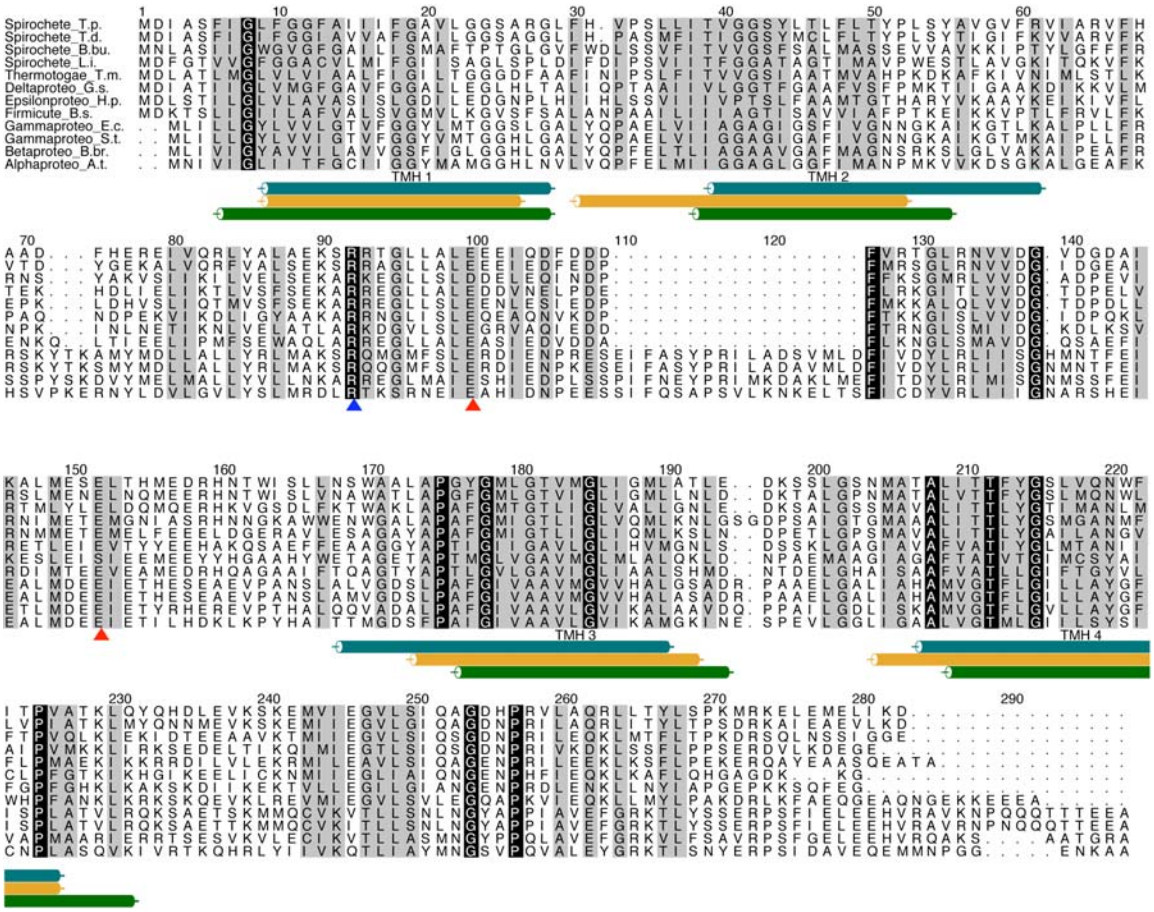

Figure III-S4. Sequence Alignment of MotA.

The colored helices correspond to the predicted transmembrane helices (TMH) generated by the TMHMM Server[26]. The blue helices correspond to the predicted helices of *T. pallidum*, the orange helices to *T. maritima*'s, and the green helices to *Salmonella*'s. The blue-colored and red-colored arrowheads are the conserved positively or negatively charged amino acids that interact with the oppositely charged residues of FliG.[1]

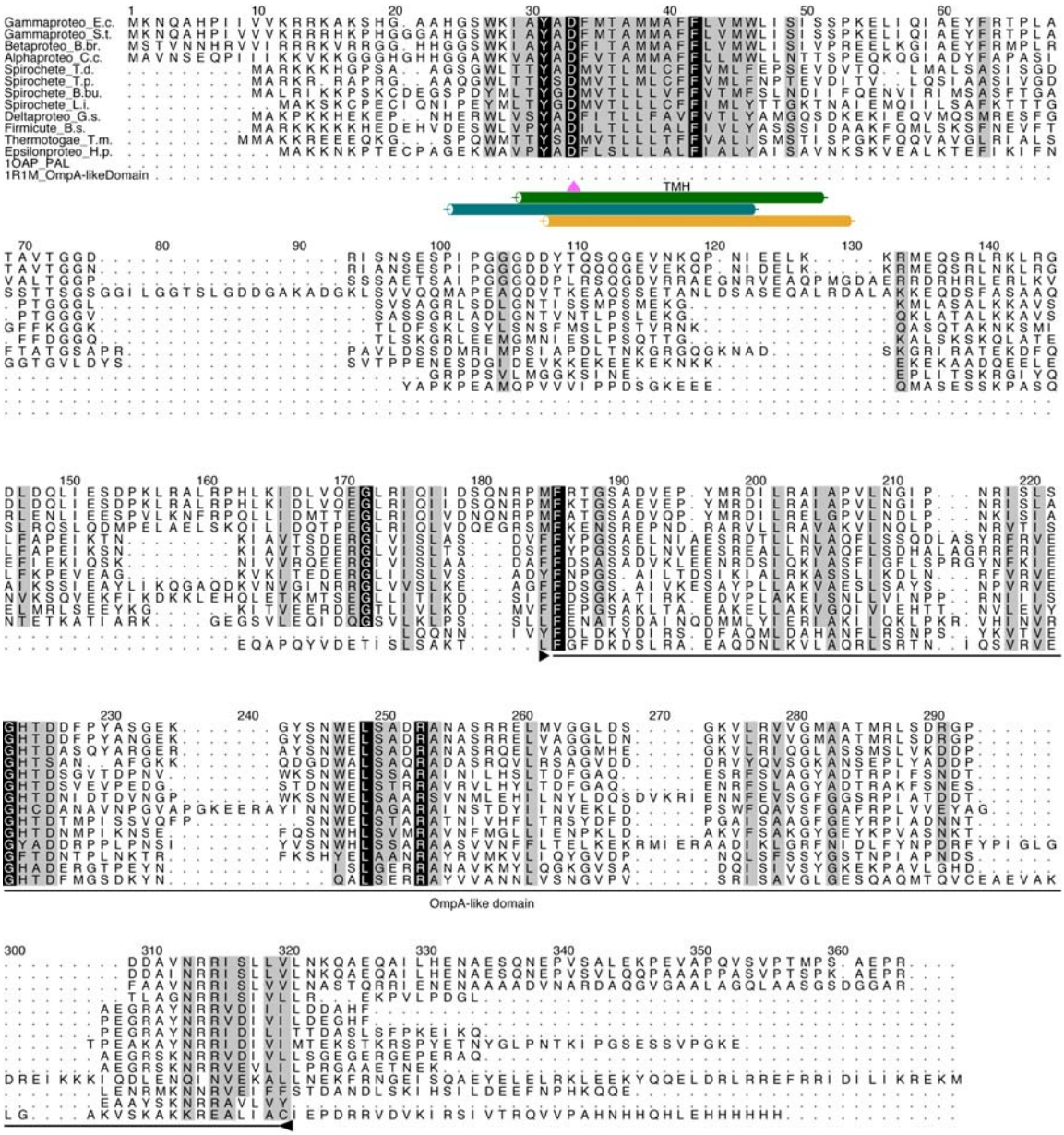

Figure III-S5. Sequence Alignment of MotB.

The colored helices are predicted and colored as in Figure III-S2. The pink arrowhead points to the conserved, protonatable aspartate residue.[1] The black line bounded by arrowheads delineates the OmpA-like domain that binds to the peptidoglycan layer. Also aligned are the chain sequences from the crystal structures of the *E. coli* Peptidoglycan-

associated lipoprotein (PDB id: 1OAP) and the OmpA-like domain from *N. meningitidis* RmpM (PDB id: 1R1M).

Supplementary Movie

The movie first shows orthoslices from top to bottom through the reconstruction of one *T. primitia* cell and then displays the segmented surfaces of tip filaments (green), the outer membrane (brown), the inner membrane (pink), the two periplasmic flagella (blue and red), and the surfaces of the motors for each flagella (blue and orange). An isosurface of the averaged, symmetrized flagellar motor is shown next (yellow), and finally the components that are thought to spin are colored in blue, while the fixed stator region is shown in yellow and orange.

Supplementary Methods

Cell Growth and Grid Preparation. Cultures were grown to an OD of ~ 0.6 at room temperature in sealed culture tubes containing 4YACo medium under a headspace of 80% H_2 and 20% CO_2 as described previously[21]. To prevent aggregation in high-salt solutions, 10 nm colloidal gold was pretreated with 5% BSA for 30 minutes. It was then concentrated five-fold and 5 ml was applied to glow-discharged, carbon-coated R 2/2 quantifoil grids, and then dried. Grids were plunge frozen in a Vitrobot (FEI Company) in 100% humidity.

Electron Tomography Data Collection and 3-D Reconstruction. Tilt series were acquired using the UCSF Tomo software[27]. Typically, tilts were incremented 1º from –63º to 63º. The magnification was 22,500 (0.98 nm/pixel) and the total dose was ~ 110 $e^-/Å^2$, distributed according to the 1/cos scheme. Tomograms were reconstructed using IMOD[28].

Image Processing. Bsoft[29] and the Peach distributed computing system[30] were used for image processing. Visualization and surface map measurements were done with Amira

(Mercury Computing Systems). The twenty extracted particles were bandpass-filtered between 200 nm and the first CTF zero. The missing wedge in reciprocal space was masked so that only measured regions of reciprocal space were used to align the particles, but no other object-specific mask was used. Course alignments were done in refine mode with an initial angular step size of 5° through all three Euler angles. Map averaging, symmetrization, and significance testing were done as described in the main text and supplementary figure legends.

Supplementary Notes

22. Frank, J. *Three-Dimensional Electron Microscopy of Macromolecular Assemblies* (Academic Press, San Diego, 1996).

23. Thompson, J. D., Higgins, D. G. & Gibson, T. J. CLUSTAL W: improving the sensitivity of progressive multiple sequence alignment through sequence weighting, position-specific gap penalties and weight matrix choice. *Nucleic Acids Res*. **22**, 4673-80 (1994).

24. Barton, G. J. ALSCRIPT: a tool to format multiple sequence alignments. *Protein Eng*. **6**, 37-40 (1993).

25. Marykwas, D. L. & Berg, H. C. A mutational analysis of the interaction between FliG and FliM, two components of the flagellar motor of *Escherichia coli*. *J. Bacteriol.* **178**, 1289-94 (1996).

26. Krogh, A., Larsson, B., von Heijne, G. & Sonnhammer, E. L. Predicting transmembrane protein topology with a hidden Markov model: application to complete genomes. *J. Mol. Biol.* **305**, 567-80 (2001).

27. Zheng, Q. S., Braunfeld, M. B., Sedat, J. W. & Agard, D. A. An improved strategy for automated electron microscopic tomography. *J. Struct. Biol.* **147**, 91-101 (2004).

28. Kremer, J. R., Mastronarde, D. N. & McIntosh, J. R. Computer visualization of three-dimensional image data using IMOD. *J. Struct. Biol.* **116**, 71-6 (1996).

29. Heymann, J. B. Bsoft: image and molecular processing in electron microscopy. *J. Struct. Biol.* **133**, 156-69 (2001).

30. Leong, P. A., Heymann, J. B. & Jensen, G. J. Peach: a simple Perl-based system for distributed computation and its application to cryo-EM data processing. *Structure* **13**, 505-11 (2005).

Chapter IV

Ultrastructure of *Treponema primitia* by electron cryotomography

Gavin E. Murphy[1], Eric G. Matson[2], Jared R. Leadbetter[2],

Howard C. Berg[3], Grant J. Jensen[1*]

Divisions of Biology[1] and Environmental Science and Engineering[2], California Institute of Technology, Pasadena, CA 91125,

Department of Molecular and Cellular Biology, Harvard University, Cambridge, MA 02138[3]

*To whom correspondence should be addressed: 1200 E. California Blvd., Pasadena, CA 91125, 626-395-8827 (phone), 626-395-5730 (fax), **Jensen@caltech.edu**.

Abstract

Members of the bacterial Phylum *Spirocheates* are generally spiral or undulate cells propelled by periplasmic flagella. The spirochete *Treponema primitia* is of particular interest because of its mutualistic role in the termite gut, where it is believed to cooperate with H_2-producing, cellulose-decomposing protozoa in the biotechnologically interesting process of converting wood into bioenergy. Here we report the ultrastructure of *T. primitia* as obtained by electron cryotomography of intact, frozen-hydrated cells. Several novel external structures were revealed including bowl-like objects decorating the outer membrane, arcades of hook-like filaments winding along the exterior, and tufts of fibrils extending from the cell tips. Inside the periplasm, cone-like structures were found at each pole. Instead of the single peptidoglycan layer typical of other Gram-negative bacteria, two distinct periplasmic layers were observed. These layers formed a central open space that contained two flagella situated adjacently to one another. In some areas, the inner membrane formed flattened infoldings that protruded into the cytoplasm. Within the cytoplasm were spherical granules, ribosome-like particles, chemoreceptor arrays, and a distinct nucleoid region. High-speed light microscopic images of swimming *T. primitia* cells showed that cell bodies remained rigid and moved in a helical rather than planar motion. These movements and ultrastructural details support the particular model for spirochete motility that posits rotation of the outer sheath with respect to the protoplasmic cylinder. The wealth of ultrastructural detail seen here by electron cryotomography suggests that there may be more complexity and diversity in bacterial ultrastructure than has yet been appreciated.

Introduction

Many members of the phylum *Spirochaetes*—such as *Treponema pallidum*, *Leptospira interrogans* and *Borrellia burgdorferi*—are important human pathogens, causing the diseases syphilis, Weil's disease, and Lyme disease, respectively. Others, however, cooperate beneficially with their animal hosts. *Treponema primitia,* for example, is a species that inhabits the hindgut of the termite *Zootermopsis angusticolis* and synthesizes acetate from H_2 and CO_2, which are intermediates generated by gut protozoa during the fermentation of wood polysaccharides. Acetate serves as the major energy source of their insect host, and up to a third of it is derived from CO_2-reducing homoacetogens like *T. primitia* [1-3]. In early microscopic studies on termite gut ecosystems, spirochetes were observed to attach to, and sometimes even propel, certain hindgut flagellate protozoa [4-6]. It has since been hypothesized that that interspecies H_2-transfer between H_2-producing protozoa and H_2-consuming spirochetes such as *T. primitia* might be promoted by such associations [4].

Spirochetes are unusual with respect to other bacteria in that their flagella are confined within the periplasm. This feature has led to the biophysical question: How do internally situated flagella impart cell motility? Rotation of periplasmic flagella is thought to drive motility by causing the entire cell body to gyrate and/or rotate [7-12]. Compared to externally flagellated bacteria, spirochetes move effectively in gel-like, viscous environments [13, 14]. Motility and its enabling ultrastructure has been linked to spirochete pathogenesis [15] and in *T. primitia*, both are likely to be important for inhabiting the termite gut.

Most of what is known about spirochete cell structure comes from conventional EM studies, which involve chemical fixation, dehydration, plastic-embedding, sectioning, and heavy metal staining. While some details are lost or distorted by these procedures, they have revealed inner and outer membranes, subterminally attached periplasmic flagella, and close associations with host protozoa [6]. More recently, it has become possible to image intact cells in three dimensions (3-D) in a nearly native state by electron cryotomography (ECT) [16, 17]. In this technique, cells are spread into thin films and frozen so quickly that ice crystals do not form, thus preserving the specimen in a life-like, "frozen-hydrated" state. A series of images is then recorded of each frozen cell as it is rotated incrementally in an electron microscope. The images are used to calculate a three-dimensional reconstruction of the entire cell and its contents with a resolution that is typically sufficient to identify and locate large macromolecular complexes *in-situ*. In this way, the first structure of a complete bacterial flagellar motor was obtained by imaging *T. primitia* cells [18]. Previous tomographic reconstructions of the spirochete *Treponema phagedenis* cells have already shown their interesting cytoskeletal architecture, although these cells were conventionally preserved rather than frozen-hydrated [19].

By imaging *T. primitia* cells in a frozen-hydrated state by ECT, several surprising ultrastructural features have been discovered including bowls, arches, and fibrils on the outer surface; a multi-layered and capped periplasmic space; and a subdivided cytoplasm with internal membrane sacs and other large structures. Together with high-speed, light microscopic video of swimming *T. primitia* cells, these ultrastructural features support the particular model of motility wherein the flagella cause rotation of a flexible outer

sheath about a rigid, helical, protoplasmic cylinder [11]. The features of *T. primitia* identified in this study also suggest that the complexity and diversity of bacterial ultrastructure may have been underestimated by previous imaging technologies.

Results

Examination of T. primitia *in the near-native state reveals novel ultrastructural features.*

Although *T. primitia* is an anaerobic organism that can survive for only a short time in the atmosphere, it is still a favorable specimen among spirochetes for high resolution ECT because it is thin and can be cultured relatively easily. *T. primitia* cells are fragile and tended to lyse when centrifuged or when blotted during the robotic vitrification process. To reduce this problem, cells were quickly frozen directly from their culture media using a manual blotting procedure that reduced trauma. Eighteen 3-D reconstructions were calculated that together included one complete cell and twenty-three magnified cell tips. Three of these cells were intact but the others had ruptured outer membranes on one side of the cell. The different cell reconstructions referred to below are numbered 1–7.

Fig. IV-1 shows a 10 nm thick, 700 nm long (~ 10% of the cell length) slice through the reconstruction of cell #1. Several novel features were observed, including structures we refer to as “surface bowls,” “surface hook arcades,” and "polar fibrils." A polar "cone" was seen inside the periplasm as well as the two expected flagella and flagellar motors. Ribosome-like particles were visible in the cytoplasm. Surface views of the manually segmented cell #1 are shown in Fig. IV-2 and Supp. Movie IV-S1.

Because samples can only be tilted to ~ 65˚, the resolution of the reconstructions is anisotropic, and surfaces parallel to the grid are difficult to resolve. Thus the tops and bottoms of the cell are missing in the segmentations. Nevertheless, the width of the cells perpendicular to the beam was ~ 350 nm. The flagella and hook arcades wrapped right-handed about the cell. The flagella from both poles were seen at this tip lying side-by-side beneath the surface hook arcade: the motor for the flagellum colored red was found ~ 100 nm away from the tip of the inner membrane, and the flagellum colored green (which emanated from the opposite cell pole) ended about 500 nm away.

Fig. IV-3 and Supp. Movie IV-S2 show similar surface views of cell #2, in which two cells were seen attached to each other. The cell in the lower half of the figure (#2b) was located in an ice-filled hole in the carbon supporting film, while the upper cell (#2a) lay on the carbon. Cell #2b's outer membrane was lysed, but #2a's was not. This happened several times, suggesting that the outer membrane was fragile, but it could be protected somewhat from the blotting and plunge-freezing procedure by the supporting carbon film. The side views (Fig. IV-3B and 3D) show how the carbon film apparently also pushed the cells slightly out of alignment. Other connected cells were observed in the light microscope and they were still motile.

Bowl-like structures arrayed the exterior surface of the outer membrane.

Novel "surface bowls" were present on the outer membranes of all the cells. While they usually appeared to be randomly arranged, in one case they formed 2 or 3 rows of right-handed helices (Fig. IV-3G). Sometimes the bowls were present underneath the surface hooks (Fig. IV-2B, 5A, and 5B). Fifty-six individual bowls were extracted, aligned,

averaged, and circularly symmetrized to produce a higher signal-to-noise density map (Fig. IV-4). The bowls were 16 nm high, 45 nm wide, and their bottoms were 8 nm above the membrane (measured from the center of each feature). In the symmetrized average the membrane just below the bowl appeared "dimpled," probably because the point-spread function of the microscope produces an inverse halo around dense objects. In this case, the halos around the bowl and the membrane are expected to slightly reduce the apparent density of the top of the membrane, the bottom of the bowl, and the "stalk" that connects them.

Arcades of counter-opposing hook-like structures lined the surface.

Long series of arches (arcades) were seen decorating the outside of eighteen of the twenty-four partially- or fully-reconstructed cells, including both lysed or unlysed cells. In cell #1, an arcade began over the motor and apparently wrapped right-handed around the cell directly above the flagella along the entire reconstructed region (Fig. IV-2, and panel B in particular). There were four arcades on cell #2a and a partial arcade on cell #2b. A pair of arcades ran above cell #2a's flagella, but it did not wrap directly over them (Fig. IV-3D–G). Another arcade was located a quarter arc from the pair, and the fourth was located opposite the pair. Fig. IV-5 highlights a particularly well-reconstructed pair of ~ 600 nm long arcades that ran atop lysed cell #3. The possible relationship between the arcades and the flagella was puzzling. In many cases there were arcades on cell surfaces far away from the flagella, and most of the flagella were not covered by arcades, but there were a few stunning instances where the hook arcades were seen directly over the flagella for long distances, as if they were associated (as in cell #1).

The arches appeared to be composed of two symmetric hooks that joined at the top. Several sections of a hook arcade were aligned together and averaged, then positioned onto their probable two-fold symmetry axis and symmetrized. The two-fold symmetrized average (Fig. IV-5D) shows the meeting of individual hooks at the top, where adjacent arches touched each other to form a continuous roof. The pillar area did not emerge from the averaging because the density was weak and apparently non-uniform. The arches were seen to be angled 35˚ from the long axis of the arcade, so that each hook abutted the one two positions away from it at the base (Fig. IV-5E). The hooks were ~ 4 nm wide; the pillars were 29 nm apart, and the arcades were 40 nm wide and 43 nm high.

Polar fibrils projected from the cell tips.

Tufts of 6 nm thick fibrils extended from the tips of twenty-two of the cells (Fig. IV-6), including both poles of cell #6 (Fig. IV-6G). Some tips had one tuft (Fig. IV-3, Fig. IV-6 A-D and G), others two (Fig. IV-2 and 6E), and still others were forked (Fig. IV-6H). Some fibrils were short and fairly straight and others were long and curved, but it is unclear whether they were fundamentally different. The longest straight fibril was 350 nm and the shortest curvy fibril was 370 nm, so perhaps beyond a certain persistence length they bend. Both types were sometimes seen bundled together in the same tuft. An exceptional 1.6 micrometer long fibril was seen on cell #1 (Fig. IV-6E). In some cases, density could be traced from the fibrils through the periplasmic cone all the way to the inner membrane (Fig. IV-6C).

Cone-shaped material occupied the periplasmic poles.

Cone-shaped, apparently porous, periplasmic structures were present at the tips of all but one of the reconstructed cells (Fig. IV-7 and Supp. Movie IV-3). The cones lay underneath the outer membrane region from which the fibrils extended. In the two reconstructions of connected cells, each cell had its own periplasmic cone, and the two cones abutted tip-to-tip. Since these densities were still cone-shaped, even in connected cells where the outer membrane did not limit them (Fig. IV-7C), the conical shape is probably inherent to the structure rather than imposed by the outer membrane.

Periplasmic flagella lay between two distinct periplasmic cell wall layers.

Two clear layers were visible between the inner and outer membranes in some reconstructions (Fig. IV-8A and Supp. Movie IV-S4). In order to confirm this visual observation, density profiles along normals to the surface (like "core samples") were calculated and averaged in regions where the periplasm was approximately uniformly thick (Fig. IV-8E). This excluded the area around flagella and especially the flagellar motor, where the periplasm was wider (also visible in Fig. IV-1A). Four peaks emerged, corresponding, respectively, to the outer membrane at the top/origin, an “outer periplasmic layer” 9 nm below, the “inner periplasmic layer” 12 nm deeper, and finally the inner membrane another 7 nm lower. Densities were measured as a function of distance from the outer membrane, so structural variability increasingly blurred features towards the interior. This is why the peaks corresponding to the inner membrane and inner periplasmic layers are broader than their outer counterparts. The flagellum was 20

nm thick and in some views was clearly seen to lie between the two periplasmic layers, pushing them apart (see also Supp. Movie IV-4).

Cytoplasmic structures

Flattened membrane sacs were visible in several reconstructed cells. They were always close to the inner membrane and appeared to be membrane invaginations (Fig. IV-9). Spherical bodies ~ 30 nm wide with smooth and uniform internal textures reminiscent of polymer storage granules were seen in the cytoplasm of several of the cells (Fig. IV-7C). Strips of density resembling chemotaxis receptor arrays were present ~ 20 nm from the inner membrane close to flagellar motors at the cell poles (Fig. IV-9A) [20, 21]. In all the reconstructions the cytoplasm was divided into two regions with different textures: a more punctuated, cylindrical shell on the outside filled with ribosome-like particles; and a smoother, inner tube roughly half the diameter of the inner membrane (~ 125 nm) without ribosome-like particles. The inner tube was likely the nucleoid region that houses the genome (Fig. IV-9A).

T. primitia *appeared to be a rigid helix as it swam.*

High-speed movies were recorded of cells swimming in a buffered salt solution containing 0.175% methyl cellulose (viscosity = 4 cP), which is only slightly more viscous than water (Fig. IV-10 and Supp. Movie IV-5). Because motility models for other spirochetes such as *Leptospira* and *Borrelia* involve cell shape changes and/or planar waves, we looked carefully for evidence of these possibilities. *T. primitia* cells looked like rigid helices at all times, and no evidence of polar hooks or gyrations was

seen. Projections of planar-wave-shaped cells like *Borrelia* appear as straight lines and then later as sine waves of varying amplitude as the plane of the wave rotates in and out of the projection direction. Here, the cells always appeared sinusoidal with constant amplitude, consistent with a rigid helical rotation. Further, the relative height of each section along the cell was discernable by the sharpness of its focus. Again, unlike a planar cell but consistent with a rigid helix, points of similar focus were seen to move steadily down the cell (arrowheads, Fig. IV-10). The helical pitch (wavelength) of the cell was ~ 2.5 μm; the radius was ~ 0.6 μm, and the cell moved at ~ 12 μm/s. In Fig. IV-10, it can be seen that a complete helical revolution occurred every ~ 60 ms (i.e., the shape is nearly identical at 0 and 60, 10 and 70, 20 and 80 ms), but the cell translated just ~ 0.7 μm, or 29% of a wavelength, per revolution. Thus there was substantial circumferential slip, as expected for propulsion in a dilute aqueous medium. For comparison, *E. coli* swims at 30 μm/s in aqueous solutions [22].

Discussion

The ultrastructure of *T. primitia* was examined here using electron cryotomography and the results are summarized in Fig. IV-11A. Unique surface bowls dotted the outer membrane exterior. Novel hook-shaped appendages were aligned in parallel, face-to-face rows, generating macromolecular arcades striping the length of the cell's OM—sometimes, but not always, directly above the two juxtaposed periplasmic flagella. Fibrils extended from the cell tips. Periplasmic cones were found at the cell poles between the two membranes, and the flagella lay between two distinct periplasmic

layers. Cytoplasmic structures like membrane invaginations, chemotaxis strips and ribosome-excluded zones were visible.

In other organisms, familiar surface structures like S-layers, fimbriae, and fibrils serve as protective coats, as platforms for adhesion and interaction with neighbors and hosts, and in motility [23, 24]. The surface bowls and hook arcades seen here may perform similar functions. A "goblet" structure slightly taller and narrower than the surface bowls was seen to coat the outer membrane of *Flexibacter polymorphus* [25, 26]. However, the incomplete coverage of the surface bowls argues against a protective role. The positioning of some hook arcades over the flagella suggests a potential role in motility.

Symbiotic spirochetes are already known to use their cell tips to attach to protozoa [4, 6]. The fibrils seen here might similarly attach *T. primitia* to its protozoan hydrogen supplier. Most fibrils are known to extend from the outer membrane, but some originate from the inner membrane [27]. Here some fibrils were seen to extend into and perhaps all the way through the periplasmic cones, which may serve as anchor points for cell attachment or stabilizers for the poles during motility.

Normally gram-negative bacteria have only one peptidoglycan layer linked to proteins from both the outer and inner membrane. The unique motility strategy of spirochetes, however, presents a structural challenge because the rotation of the periplasmic flagella introduces unusual forces. If there were only one periplasmic layer in spirochetes, the flagella would have to rotate between the outer membrane and peptidoglycan layer, producing two potential problems: at least some of the outer membrane would be unsupported by peptidoglycan, and the forceful rotation of the

flagella might rupture the outer membrane. The discovery of two periplasmic layers in *T. primitia* offers an elegant solution. The flagella rotate within an apparently structurally reinforced space, and the whole outer membrane is supported. The inner periplasmic layer probably consists of peptidoglycan, since MotB of the flagellar stators (which is present in *Treponema*) is known to bind to peptidoglycan for stability [28]. The composition of the outer periplasmic layer is unknown, but the presence of such a layer may help explain the formation of patterns seen previously in the outer membranes of the related species S. *aurantia*, *S. litoralis*, and *T. microdentium* [6].

Spirochete motility is complex. Two classes of motility models exist, but only one of them is consistent with our observations of *T. primitia*. The first class is for spirochetes like *Leptospira interrogans* and *Borrelia burgdorferi*, for which the periplasmic flagella (PF) are stiffer than the "protoplasmic cylinder" (PC) [7, 8, 10, 12]. For *T. primitia,* the PC includes the inner membrane and the inner periplasmic layer. The second class is for spirochetes like *Cristispira balbianii* and *Spirocheta aurantia,* where the PF are less stiff than the PC [11, 13]. In both models, the PF rotate in place relative to the PC, because they are tethered to the PC. In the first model, bending and changes in the shape of the PC, i.e., propagation of a helical wave for *L. interrogans* and propagation of a planar wave for *B. burgdorferi*, are driven by the rotation of the PF. In the second model, the PC remains rigid but the whole cell is made to roll about the body axis by circumferential flow of the "outer sheath" (OS), which for *T. primitia* includes the outer membrane and the outer periplasmic layer. Since *T. primitia* appears to maintain a constant helical shape, only the second model is viable.

The flagellar motors at opposite ends of the cell are opposed, so when the PF rotate in opposite directions (one clockwise when viewed from outside the cell as it emerges from the inner periplasmic layer and the other counter-clockwise), they rotate in the same direction when viewed in transverse section (Fig. IV-11A). Friction between the PF and the OS causes the OS to rotate around the PC (counter-clockwise in Fig. IV-11B, as depicted by the brown arrow), and viscous shear between the OS and the external medium causes the entire cell (the PC and PF, and concomitantly, the OS) to roll in the opposite direction (clockwise, as depicted by the blue arrow in Fig. IV-11B and red arrows in Fig. IV-11C). If the body of the cell rolls clockwise and the PC is right-handed, this will cause the cell to drill (swim) into the page and to the upper right (as depicted by the straight green arrow in Fig. IV-11C). If the cell swims in a dilute aqueous medium rather than in a gel-like medium, thrust is generated by the slantwise slip of segments of the helical body relative to the external medium, just as thrust is generated by slantwise slip of segments of flagellar filaments for ordinary flagellated bacteria [29]. If the cell swims in a gel-like medium, e.g., 1% methylcellulose or dilute agar, it will bore its way through the medium like a corkscrew through a cork [13]. The medium used for the experiment shown in Fig. IV-10 by comparison is not nearly as gel-like and as expected, significant slippage was observed. In completing one revolution about its axis, this cell translated less than a third of its wavelength. In any event, if both flagellar motors change their directions of rotation, the cell will back up. If only one motor changes its direction of rotation, the cell will stop; and if the PC is sufficiently pliable, the cell might flex.

In the case of *T. primitia*, the OS did not appear to be wrapped tightly around the PC, consistent with this model in which the OS flows around the PC. Problems emerge, however, when reconciling the model with the ultrastructure. Hook arcades were seen over the flagella in the best-preserved cells. Counter rotation of the OS and PC (and its attached PF) would not permit alignment of the two except once per cycle. Also, counter rotation of the two membranes would presumably prevent efflux channels from forming. Efflux channels are either transitory or longer-lived alignments of inner and outer membrane channels and periplasmic adaptors to create “stovepipes” that expel cytoplasmic contents [30]. Sequence similarity using the Entrez database reveals that some efflux channels like NorM and AcrB, AcrA, and TolC are present in *Leptospira*, *Borrelia* and *Treponema* species (data not shown). If the OS and PC counter rotate, such channels would break. Also, if the fibrils connect to the periplasmic cone and inner membrane, then counter rotation would strain this connection.

These potential problems disappear if the OS does not move as a rigid body but instead flows and shears differently in different areas over the cell. The cone might stabilize the periplasm at the ends of the cell so that fibrils and efflux channels could assemble and function there. The cone would then not connect rigidly to the outer periplasmic layer, but rather "cap" it at the poles. The purpose of the outer periplasmic layer might be to roll over the flagella and support the outer membrane in the midcell region between the stable cones. The presumably fluid outer membrane would rotate with the outer periplasmic layer at the midcell, but move less at the cell poles above the cones, shearing as necessary in between to maintain its integrity. Perhaps the fragility of the OS, as exemplified by its lysis after blotting or mild centrifugation, is evidence of its

fluidity. In this scenario, the purpose of the hook arcade and surface bowls might be to enhance friction between the OS and the environment.

These hypotheses suggest specific experiments. The sequence of the *T. primitia* genome is nearing completion. The fibrils, surface bowls, and hook arcades should be identifiable as major components of purified outer sheaths. Once methods to introduce genetic alterations are established, deletion mutants may elucidate the functions of these structures. Single-molecule fluorescence experiments tracking tags on both the surface bowls or other external structure and simultaneously an inner membrane protein or the flagellum may confirm whether and where the OS rotates with respect to the PC. Fluorescent tags on efflux channels should reveal whether or not they are in fact confined to the poles. Overexpression of efflux channels might cause them to mislocalize to the midcell, linking the OS and PC there and disrupting motility. In any case, the remarkable structures seen here suggest that bacterial ultrastructure and motility may be more complex and diverse than anticipated.

Experimental Procedures

Cell Growth and Grid Preparation

Cultures of *T. primitia* strain ZAS-2 were grown at 23° C in sealed culture tubes containing 4YACo medium under an atmosphere of 80% H_2 and 20% CO_2 as described previously [3] and harvested during log-growth at an OD of ~ 0.6. To prevent aggregation in high-salt solutions, 10 nm colloidal gold was pretreated with 5% BSA for 30 minutes. It was then concentrated five-fold and 5 ml was applied to glow-discharged, carbon-coated R 2/2 quantifoil grids and dried. ZAS-2 is an obligate anaerobe but can

tolerate atmospheric conditions for about 20 minutes, so grids were frozen in small batches. A small volume of cell solution was removed with a syringe. 5 ml of the uncentrifuged solution was applied to a grid. When cells were centrifuged at a mild setting of 4000 x *g*, the outer membranes lysed, so centrifugation was avoided. Initially, grids were plunge frozen in liquid ethane on a Vitrobot (FEI Company) in 100% humidity using a 2 s blot time, a –2 offset, and a 1 s drain. Blotting on both sides of the grid by the Vitrobot caused catastrophic rupture of the outer membrane, so in order to minimize trauma, grids were manually blotted on the reverse side of the applied liquid and frozen using a gravity plunger.

Electron Tomography Data Collection and 3D Reconstruction

The data collection and reconstruction process was described previously [18]. Single-axis tilt series were collected using a 300 keV FEI Polara FEG TEM automated by UCSF Tomo [31]. Typically, tilts were incremented 1º from –63º to 63º. The magnification was 22,500 (0.98 nm/pixel) and the total dose was ~ 110 $e^-/Å^2$, distributed according to the 1/cos scheme. Tomograms were reconstructed using IMOD [32] and binned twofold (1.96 nm/pixel).

Image Processing

Reconstructions were segmented manually using Amira (Mercury Computing Systems). To display the fibrils, the region of the fibrils was segmented to create a mask, which was then applied to the volume file. The fibrils were displayed as an isosurface. Surface bowls and hooks were averaged by computationally extracting individual particles,

aligning, and averaging them using the Bsoft image processing package [33]. Two-fold symmetry was imposed on the surface hooks, and hundred-fold symmetry was imposed on the surface bowls to smooth the reconstructions. The true symmetry of the surface bowls, if any, is unknown. Amira was used to estimate all measurements. To measure periplasmic density, the volume of one cell interior to the outer membrane was segmented. A surface map was generated and then smoothed. Density normal to this one surface was measured at each vertex of the surface triangles using a customized Amira module. The density was averaged to display density versus periplasmic depth. Measurements were taken over more than 25,000 pixels, corresponding to about 1% of the total surface area of a cell.

Light Microscopy

Phase-contrast images of swimming cells were captured using a high speed AxioCamHS digital camera mounted on an AxioPlan 2 microscope (Carl Zeiss, Inc.).

Acknowledgements

We thank H. Jane Ding for creating an Amira module for analysis. This work was supported in part by NIH grants P01 GM66521 and R01 AI067548 to G.J.J., DOE grant DE-FG02-04ER63785 to G.J.J., a Searle Scholar Award to G.J.J., NSF grants DEB-0321753 and EF-0523267 to J.R.L., NIH grant AI016478 to H.C.B., NIH graduate fellowship F31 EB 004179 to G.E.M., and gifts to Caltech from the Ralph M. Parsons Foundation, the Agouron Institute, and the Gordon and Betty Moore Foundation.

References

1. Breznak, J. A., and Switzer, J. M. Acetate synthesis from H(2) plus CO(2) by termite gut microbes. *Appl Environ Microbiol*. **52**, 623-630 (1986).
2. Graber, J. R., Leadbetter, J. R., and Breznak, J. A. Description of *Treponema azotonutricium sp. nov*. and *Treponema primitia sp. nov*., the first spirochetes isolated from termite guts. *Appl Environ Microbiol*. **70**, 1315-20 (2004).
3. Leadbetter, J. R., Schmidt, T. M., Graber, J. R., and Breznak, J. A. Acetogenesis from H_2 plus CO_2 by spirochetes from termite guts. *Science*. **283**, 686-9 (1999).
4. Bloodgood, R. A., and Fitzharris, T. P. Specific associations of prokaryotes with symbiotic flagellate protozoa from the hindgut of the termite *Reticulitermes* and the wood-eating roach *Cryptocercus*. *Cytobios*. **17**, 103-22 (1976).
5. Cleveland, L. R., and Grimstone, A. V. The fine structure of the flagellate *Mixotricha paradoxa* and its associated micro-organisms. *Proc Roy Soc London*. **B159**, 668-686 (1964).
6. Holt, S. C. Anatomy and chemistry of spirochetes. *Microbiol Rev*. **42**, 114-60 (1978).
7. Goldstein, S. F., Buttle, K. F., and Charon, N. W. Structural analysis of the *Leptospiraceae* and *Borrelia burgdorferi* by high-voltage electron microscopy. *J Bacteriol*. **178**, 6539-45 (1996).
8. Goldstein, S. F., and Charon, N. W. Motility of the spirochete *Leptospira*. *Cell Motil Cytoskeleton*. **9**, 101-10 (1988).
9. Goldstein, S. F., and Charon, N. W. Multiple-exposure photographic analysis of a motile spirochete. *Proc Natl Acad Sci USA*. **87**, 4895-9 (1990).

10. Goldstein, S. F., Charon, N. W., and Kreiling, J. A. *Borrelia burgdorferi* swims with a planar waveform similar to that of eukaryotic flagella. *Proc Natl Acad Sci USA*. **91**, 3433-7 (1994).

11. Berg, H. C. How spirochetes may swim. *J Theor Biol*. **56**, 269-73 (1976).

12. Berg, H. C., Bromley, D. B., and Charon, N. W. Leptospiral Motility. *Symp Soc Gen Microbiol*. **28**, 285-294 (1978).

13. Berg, H. C., and Turner, L. Movement of microorganisms in viscous environments. *Nature*. **278**, 349-51 (1979).

14. Nakamura, S., Adachi, Y., Goto, T., and Magariyama, Y. Improvement in motion efficiency of the spirochete *Brachyspira pilosicoli* in viscous environments. *Biophys J*. **90**, 3019-26 (2006).

15. Li, C., Motaleb, M. A., Sal, M., Goldstein, S. F., and Charon, N. W. Gyrations, rotations, periplasmic flagella: the biology of spirochete motility in *The Spirochetes Molecular and Cellular Biology*. (Saier, M. H., Jr & Garcia-Lara, J., eds.), Horizon Press, Norfolk, (2001).

16. Jensen, G. J., and Briegel, A. How electron cryotomography is opening a new window into prokaryotic ultrastructure. *Curr Opin Cell Biol*. **in press** (2007).

17. Lucic, V., Forster, F., and Baumeister, W. Structural studies by electron tomography: from cells to molecules. *Annu Rev Biochem*. **74**, 833-65 (2005).

18. Murphy, G. E., Leadbetter, J. R., and Jensen, G. J. In situ structure of the complete *Treponema primitia* flagellar motor. *Nature*. **442**, 1062-4 (2006).

19. Izard, J., et al. Tomographic reconstruction of treponemal cytoplasmic filaments reveals novel bridging and anchoring components. *Mol Microbiol*. **51**, 609-18 (2004).

20. Lefman, J., et al. Three-dimensional electron microscopic imaging of membrane invaginations in *Escherichia coli* overproducing the chemotaxis receptor Tsr. *J Bacteriol*. **186**, 5052-61 (2004).

21. Zhang, P., et al. Direct visualization of receptor arrays in frozen-hydrated sections and plunge-frozen specimens of *E. coli* engineered to overproduce the chemotaxis receptor Tsr. *J Microsc*. **216**, 76-83 (2004).

22. Purcell, E. M. Life at low Reynolds number. *Am J Phys*. **45**, 3-11 (1977).

23. Fernandez, L. A., and Berenguer, J. Secretion and assembly of regular surface structures in Gram-negative bacteria. *FEMS Microbiol Rev*. **24**, 21-44 (2000).

24. Moissl, C., Rachel, R., Briegel, A., Engelhardt, H., and Huber, R. The unique structure of archaeal 'hami', highly complex cell appendages with nano-grappling hooks. *Mol Microbiol*. **56**, 361-70 (2005).

25. Ridgway, H. F. Ultrastructural characterization of goblet-shaped particles from the cell wall of *Flexibacter polymorphus*. *Can J Microbiol*. **23**, 1201-13 (1977).

26. Ridgway, H. F., Wagner, R. M., Dawsey, W. T., and Lewin, R. A. Fine structure of the cell envelope layers of *Flexibacter polymorphus*. *Can J Microbiol*. **21**, 1733-50 (1975).

27. White, D. *The Physiology and Biochemistry of Prokaryotes*. Oxford University Press, New York (2007).

28. Berg, H. C. The rotary motor of bacterial flagella. *Annu Rev Biochem.* **72**, 19-54 (2003).

29. Berg, H. C. *Random Walks in Biology*. Princeton University Press, Princeton (1993).

30. Piddock, L. J. Multidrug-resistance efflux pumps - not just for resistance. *Nat Rev Microbiol.* **4**, 629-36 (2006).

31. Zheng, Q. S., Braunfeld, M. B., Sedat, J. W., and Agard, D. A. An improved strategy for automated electron microscopic tomography. *J Struct Biol.* **147**, 91-101 (2004).

32. Kremer, J. R., Mastronarde, D. N., and McIntosh, J. R. Computer visualization of three-dimensional image data using IMOD. *J Struct Biol.* **116**, 71-6 (1996).

33. Heymann, J. B. Bsoft: image and molecular processing in electron microscopy. *J Struct Biol.* **133**, 156-69 (2001).

Supplementary material

The following supplementary material is available for this article:

Movie IV-S1. Segmented cell #1 with labeled components.

Movie IV-S2. Segmented cell #2 with labeled components.

Movie IV-S3. A focus on the periplasmic cones.

Movie IV-S4. Series of cross-sections through cell #8 showing two periplasmic layers.

Movie IV-S5. Light microscopy video of a single *T. primitia* cell swimming.

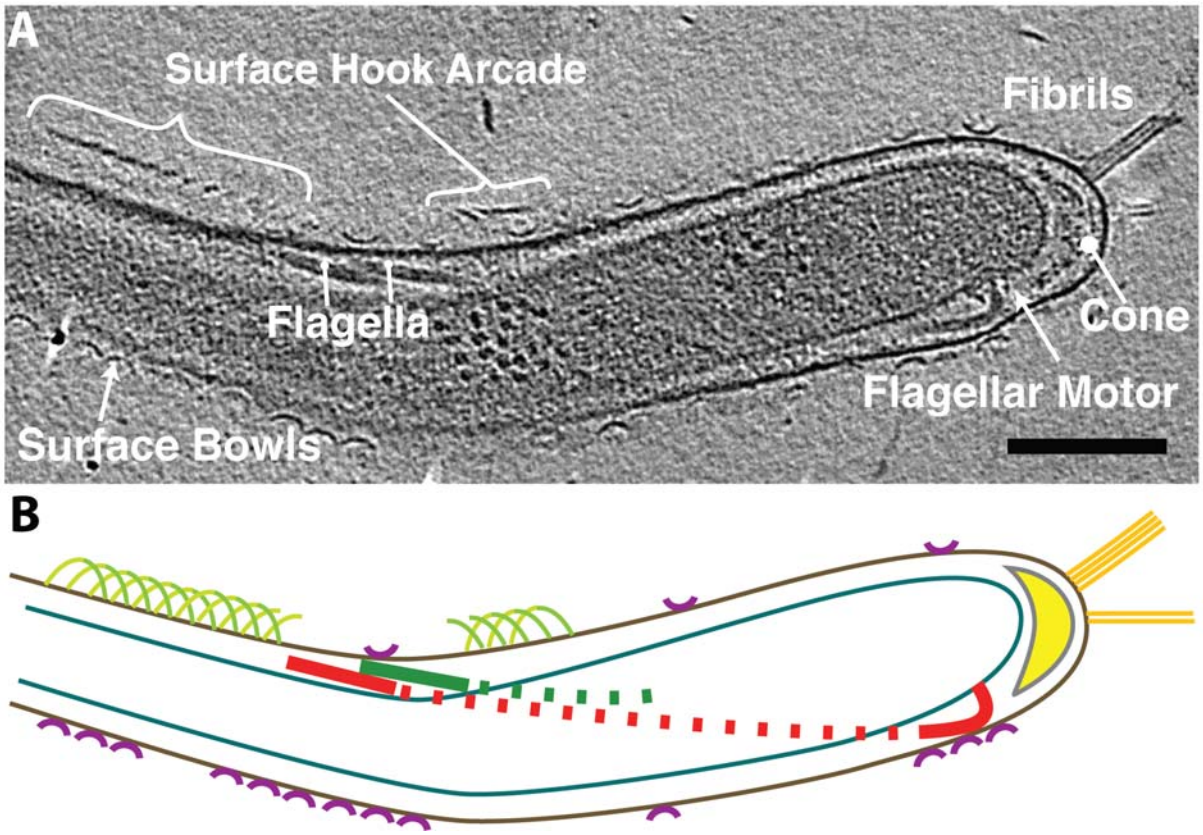

Fig. IV-1. Electron cryotomographic reconstruction of *T. primitia*

A. 10 nm section through the reconstruction of a frozen-hydrated *T. primitia* cell (cell #1). Surface bowls (magenta) dot the outer membrane surface. The surface hook arcades (chartreuse) wind atop the cell. Fibrils (orange) extend from the cell tip above a periplasmic cone (yellow). Periplasmic flagella (red and green) wrap around the cell. (Scale bar 200 nm.) B. Cartoon rendering of panel A. The same colors are used for all the figures and movies.

Fig. IV-2. Surface views of cell #1

A-D. Four side views of cell #1, incrementally rotated by 90˚. E. View of the cell tip showing the periplasmic cone underlying the fibrils. F. View from the midcell region.

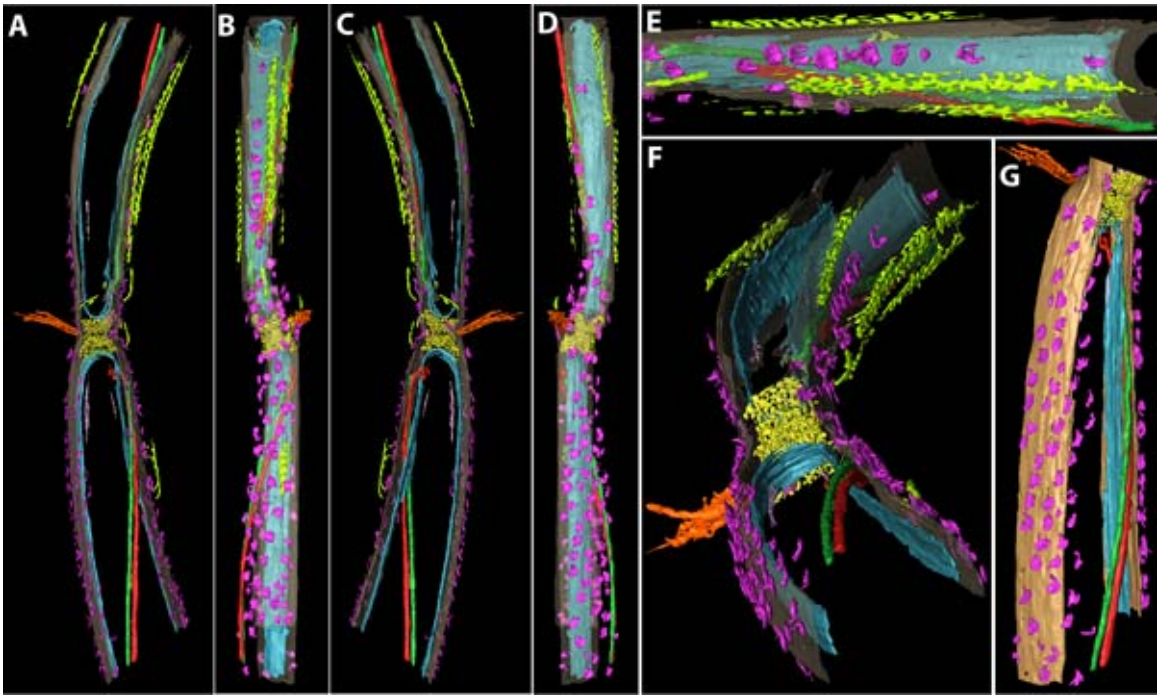

Fig. IV-3. Surface views of a connected cell

A-D. Four side views of a connected cell (cell #2), incrementally rotated by 90˚. E. A magnified view of the top cell showing the nearly matched winding of the hook arcades over the flagella. F. Oblique view similar to panel A showing multiple arcades around the cell, including one pair over the flagella and two others not above flagella. G. Oblique view similar to panel D, showing the only instance in segmented cells where the surface bowls appeared in helical rows around the cell.

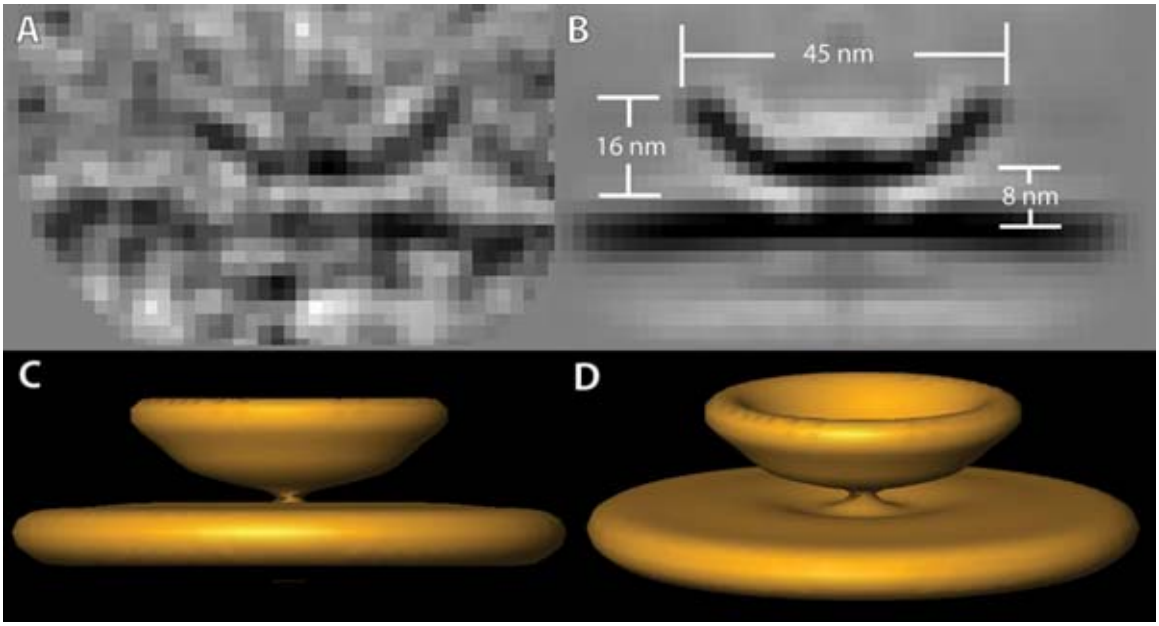

Fig. IV-4. Surface bowls

A. Axial section through the 3-D reconstruction of a single surface bowl. B. Axial slice through the symmetrized average of many bowls. C–D. Different views of an isosurface of the symmetrized average.

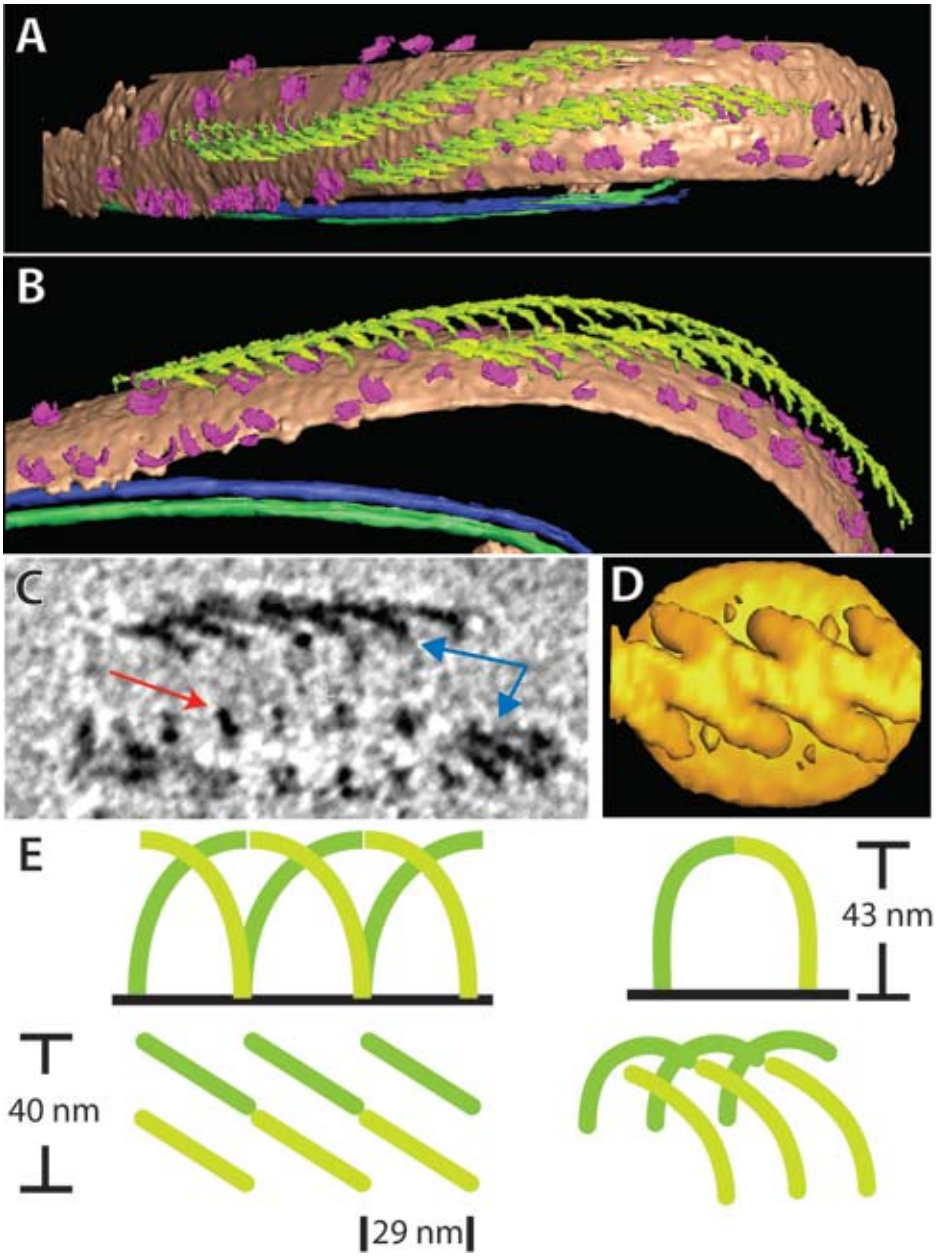

Fig. IV-5. The Hook Arcade

A. Top view of cell #3 (partially lysed) showing a pair of hook arcades. B. Oblique view of the same hook arcades. C. 4 nm section through the 3-D reconstruction, showing individual hook pillars (red arrow) and elsewhere the top of the arcade (blue arrows). D. A top view of the two-fold, symmetrized average of several hook arcade sections. E.

Cartoon drawing of the individual hooks that constitute an arcade. A hook arches over and abuts an opposite hook two pillars down.

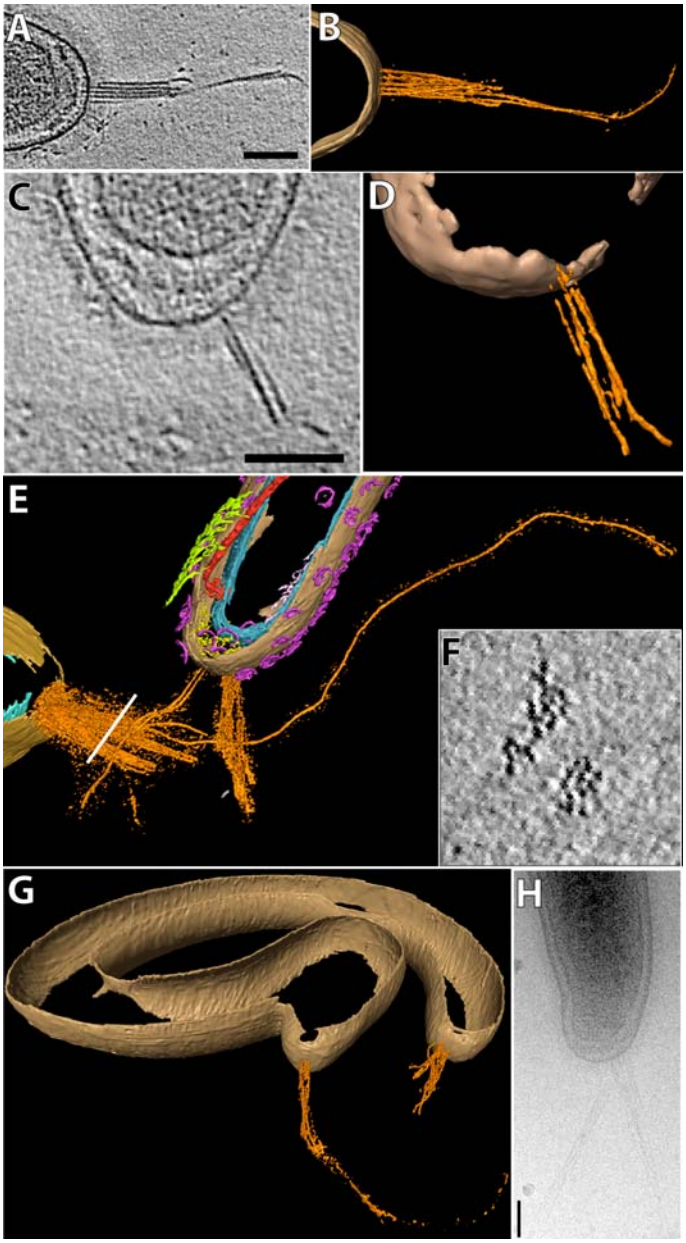

Fig. IV-6. Polar Fibrils

A. 2 nm section through the tip of cell #4, showing several fibrils extending from the tip. B. 3-D view of cell #4, showing an isosurface of the fibrils and a manual segmentation of the outer membrane. C. 2 nm section through the tip of cell #3, showing what appears to be continuous density from the fibrils through the periplasmic cone to the inner

membrane. D. 3-D view of cell #4 as in panel B. E. Isosurface of the fibrils extending from cell #1 (top) and from an additional cell (#1a, lower left) present in the same reconstruction. The fibrils in cell #1a are much more numerous, touch each other, and one fibril is ~ 1.6 μm long. F. Cross section through the bundle of fibrils from cell #1a taken at the white line in panel E. The individual fibrils are ~ 6 nm thick. G. 3-D view of cell #5, showing fibrils extending from both tips. H. Projection image of the tip of cell #6, showing forked fibrils. (All scale bars are 100 nm.)

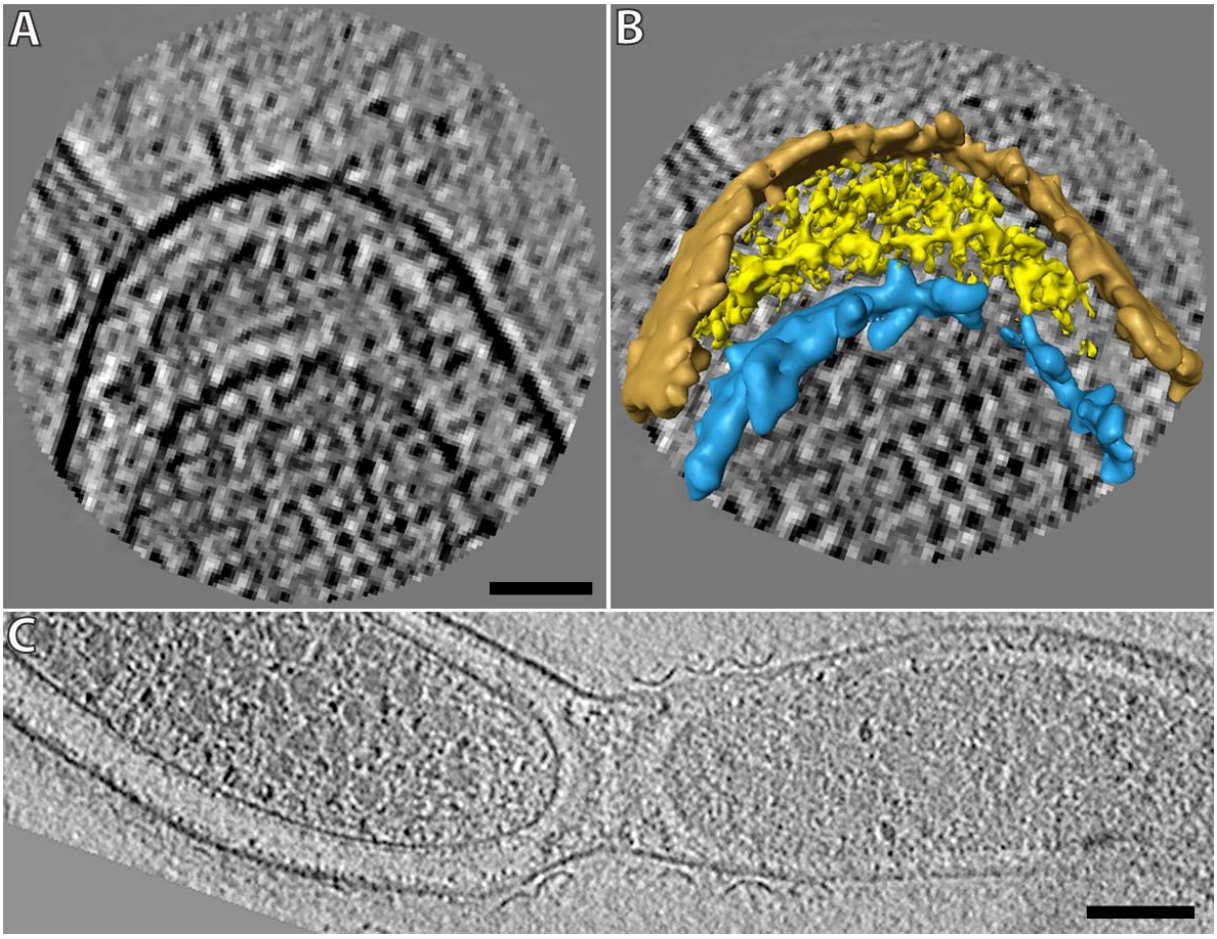

Fig. IV-7. Periplasmic cone

A. 2 nm section through the periplasmic cone of cell #1. (Scale bar is 40 nm.) B. 3-D view of cell #1, showing an isosurface of the periplasmic cone and manual segmentations of the outer and inner membranes. C. 6 nm section through two connected cells (#7 left and #7a right). The two periplasmic cones abut each other in the shape of an hourglass. Cell #7 was also remarkable because its cytoplasm was packed with ~ 30 nm wide, spherical bodies. (Scale bar is 100 nm.)

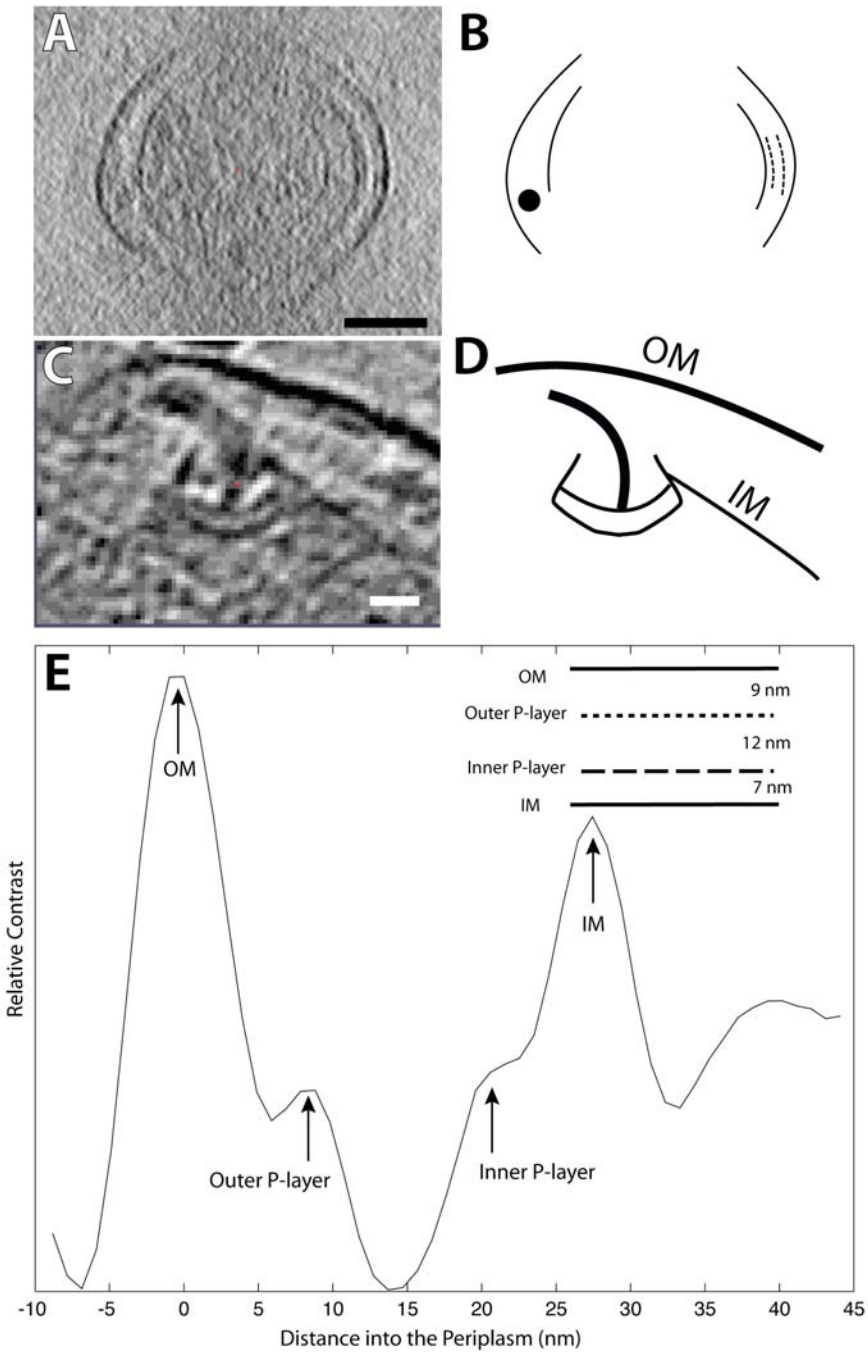

Fig. IV-8. Inner and outer periplasmic layers

A. 10 nm section through cell #8, showing two distinct periplasmic layers on the right side. The flagellum is at the bottom left. (See Sup. Mov. IV-4. Scale bar is 100 nm.) B. Cartoon guide to panel A. C. 10 nm section through a region around the flagellar motor,

showing the bulge of the periplasm near the motor. (Scale bar is 20 nm.) D. Cartoon guide to panel C. E. Average density of the periplasm as a function of distance into the cell from the outer membrane. The outer and inner periplasmic layers ("P-layers") are manifest by the smaller peaks between the two membranes.

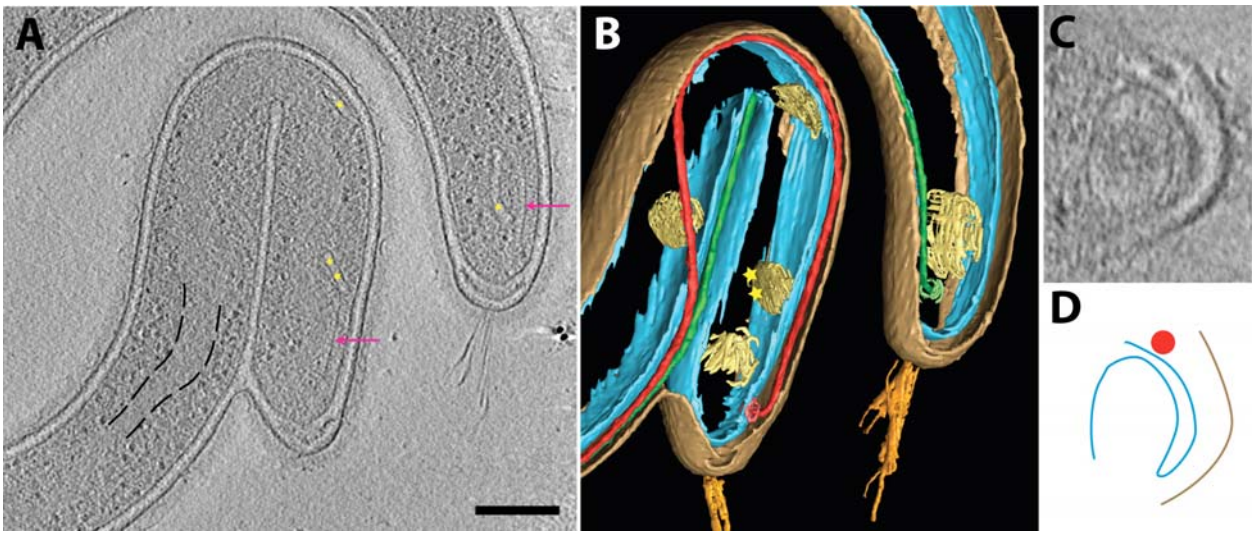

Figure 9. Cytoplasmic structures

A. 6 nm section through cell #5 showing internal membranes (gold stars), probable chemotaxis receptor arrays (pink arrows), and ribosome-excluding regions (one example region delineated by black dashed lines). (Scale bar is 200 nm.) B. Manual segmentation of cell #5. The membranes in the cytoplasm are flattened sacs near the inner membrane. C. Inclined, interpolated 6 nm section through the membrane sac marked with double gold stars in panels A and B that appears to be an infolding of the inner membrane. D. Cartoon tracing of the membranes in panel C.

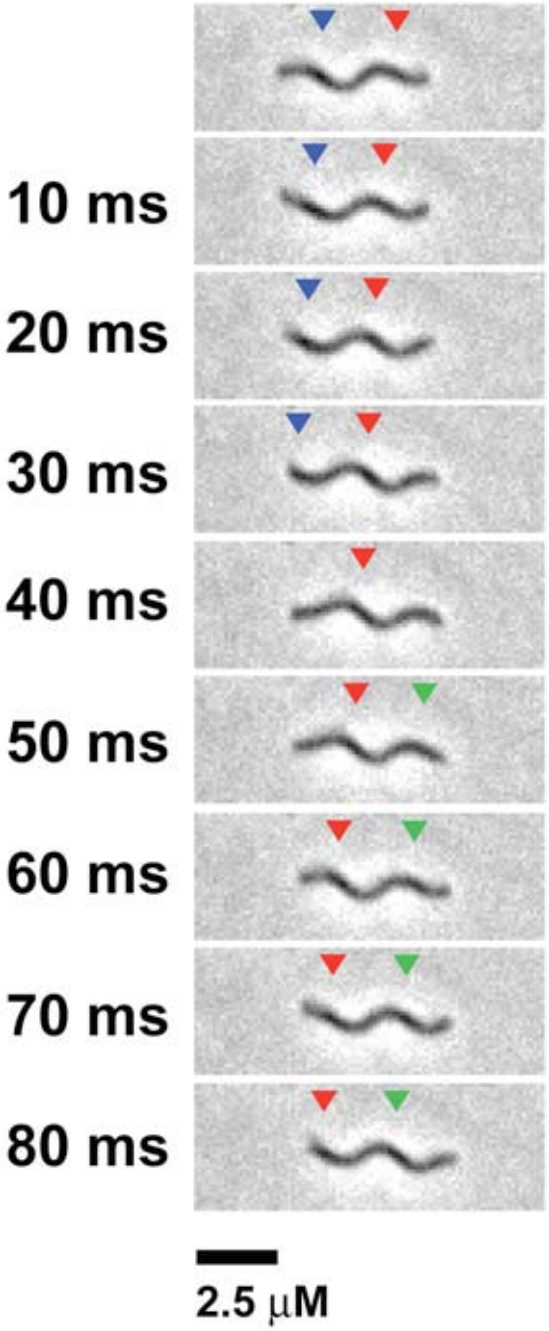

Fig. IV-10. A swimming *T. primitia* cell

Swimming cells were observed in a light microscope. Sequential frames of a single cell are pictured, showing that the cell maintains a constant helical shape as it swims. Arrows point to cell segments located in the focal plane. The cells swim at 12 μm/s in this buffer. See also Supp. Movie IV-5 for the complete movie.

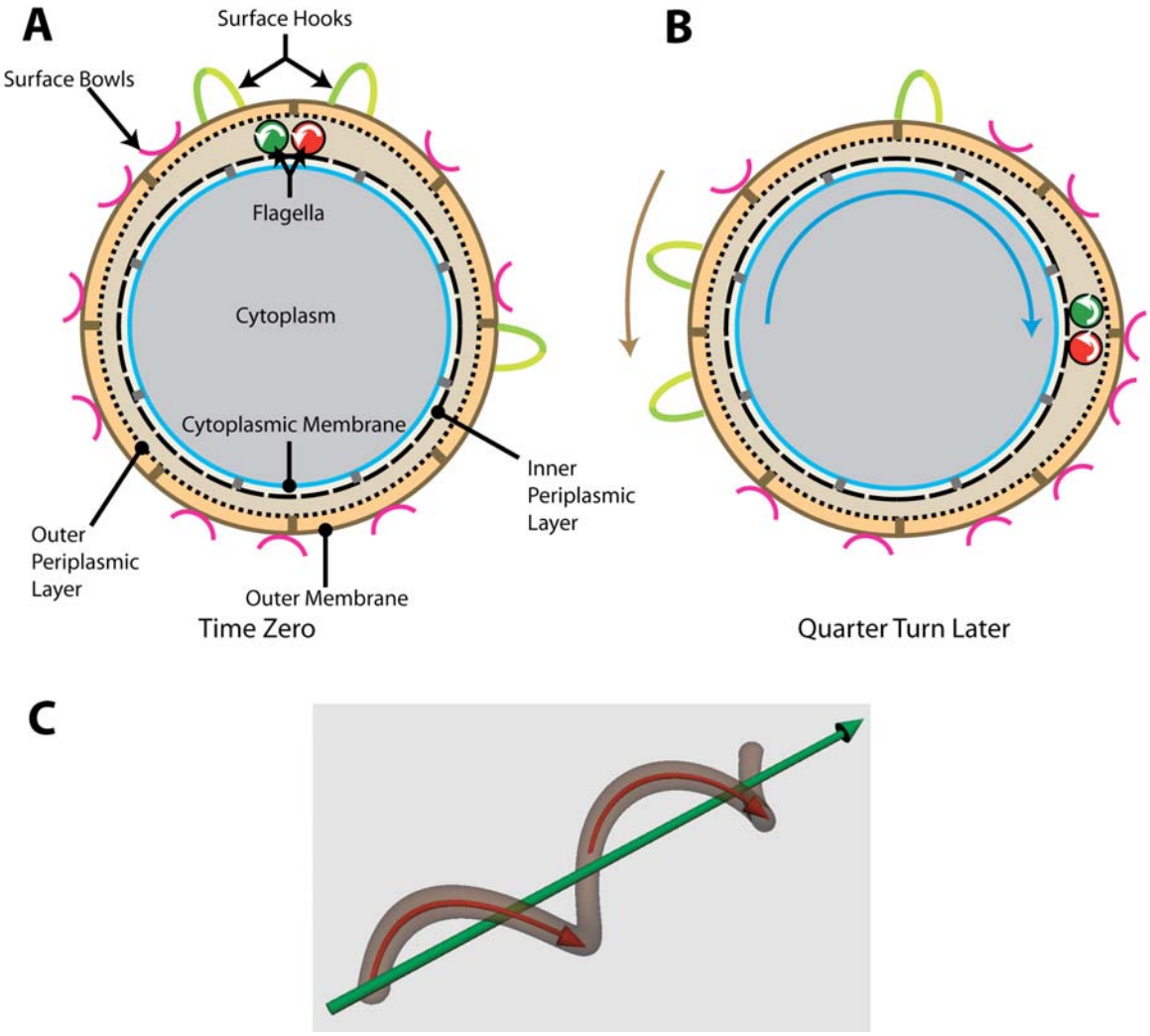

Fig. IV-11. Model of *T. primitia* ultrastructure and motility

A. Schematic cross section with labeled components at an imagined point (time "zero") when the flagella are rotating counter-clockwise (white arrows). The relative sizes of the cell thickness and the surface structures are to scale. B. Same cross section a quarter turn later. C. Oblique view of whole cell. Friction between the flagella and the outer sheath (outer periplasmic layer and outer membrane) may cause the outer sheath to rotate counter-clockwise (brown arrow). In contrast, the protoplasmic cylinder (the inner

periplasmic layer and inner membrane) must remain approximately fixed with respect to the flagella because they are attached at the position of the motor. Friction of the outer sheath against the environment may then cause the entire cell to roll clockwise (blue arrow). The helical cell would then drill itself forward like a corkscrew (red and green arrows).

Chapter V

In situ structure of the complete *Hylemonella gracilis* flagellar motor

Gavin E. Murphy[1], Eric G. Matson[2], Jared R. Leadbetter[2], Grant J. Jensen[1*]

Divisions of Biology[1] and Environmental Science and Engineering[2]

California Institute of Technology, Pasadena, CA 91125

*To whom correspondence should be addressed: 1200 E. California Blvd., Pasadena, CA 91125, 626-395-8827 (phone), 626-395-5730 (fax), Jensen@caltech.edu.

Abstract

The bacterial flagellar motor is an amazing nanomachine: Built from about 25 different proteins, it uses an electrochemical ion gradient to drive rotation at speeds normally around 60 Hz[1-3] in *E. coli.* The flagellar motor consists of a fixed, membrane-embedded, torque-generating stator and a typically bidirectional, spinning rotor that changes direction in response to chemotactic signals. While previous structural work has targeted the purified rotor from proteobacteria[4-6] or the *in situ* spirochete flagellar motor[7], little is known about the more typical stator from extracellular flagellar motors. Using electron cryotomography of whole cells, here we show the *in situ* structure of the complete flagellar motor from the betaproteobacteria *Hylemonella gracilis* at 6.5 nm resolution. Fifty-nine individual motor particles were computationally extracted from the reconstructions, aligned, and then averaged. The stator assembly possessed 11-, 12-, and 13-fold symmetry; lay next to the rotor; and was connected directly to the C ring. The stator studs were as large as the expected volume of two OmpA domains. Two novel structures were observed: an extended E collar around the P ring, and a transport (TA) ring under the rotor.

Introduction

The bacterial flagellar motor excites considerable interest because of the ordered expression of its genes, its regulated self-assembly, the complex interactions of its many proteins, and its startling mechanical abilities. Stator proteins MotA and MotB form a ring of "studs" within and above the inner membrane that couple the passage of protons across the membrane to the generation of torque[1, 2]. Above the membrane, MotB has a

peptidoglycan-binding domain that presumably holds the stator in place by binding to the globally cross-linked peptidoglycan layer[1, 2]. Below the membrane, the cytoplasmic loops of MotA are believed to spin a wheel of FliG molecules, which like radial spokes extend roughly parallel to the membrane from the rotor in the middle to just below MotA on the periphery[1]. Proteinaceous P and L rings serve as bearings to facilitate the rotation of the rod within the peptidoglycan and outer membranes, respectively[1, 2]. Inside the cell and below FliG lies the C ring, which regulates the direction of rotation in response to the chemotactic system[1, 2].

Flagellar basal bodies containing the rotor, rod, and sometimes the C ring have been purified and reconstructed by electron cryomicroscopy-based single particle analysis[4, 8, 9]. The *Salmonella* rotor possessed a mean symmetry of 25[6] or 26[10] while its C ring possessed a mean symmetry of 34[6, 11]. Because the stators do not co-purify with the rotor, however, little is known about *Salmonella*'s stator structure and interactions with the rest of the motor. Patterns of stator studs have been seen in 2D, freeze-etch images, but the interpretation of these images is difficult and the maximum number of studs has been reported as either 12 or 16, depending on the species[12-15]. For the former group, the number of studs ranged between 10 and 12. *T. primitia* had 16 studs, whose volumes were each twenty times larger than MotB's 2 OmpA domains[7]. The number of torque-generating units has been reported as either 8 or at least 11[2, 3, 16]. 2-D cryo-EM images of purified PomA/PomB complexes (homologs of MotA and MotB) from *V. alginolyticus* have revealed an ~ 70 Å long, thin extension above the membrane[17].

Results and Discussion

Here we report the complete structure of the *Hylemonella gracilis* flagellar motor obtained by electron cryotomography. *H. gracilis* was chosen because it is 250 nm wide and is a bipolar, lophotrichous spirillum with one to four flagella per tip, which maximizes the number of motors per reconstruction. It is also a betaproteobacteria and so is more related to the motors of the gammaproteobacteria *Salmonella* and *E. coli* than *T. primitia* is. Fifteen tomographic reconstructions were made from tilt-series of cells that were frozen in vitreous ice (Fig. V-1). The cell had flagellar motors, probable chemotaxis receptor arrays, a ribosome-free region that may be the nucleoid, ribosome-like particles and oddly, some cells had flagella-like filaments mistakenly located in their cytoplasm (Fig. V-1). The tilt-series were CTF corrected[18] (see Supp. Fig. V-S1), but no improvement in the resolution of the final structure was detected compared to uncorrected reconstructions. From the tomograms, fifty-nine flagellar motor particles were computationally extracted, aligned, and averaged (Fig. V-2). In some individual particles, symmetry elements were visible (Fig. V-2a), but clearer results emerged from the average (Fig. V-2e).

Several components of the individual, aligned particles were tested for rotational symmetry. With one method, the rotational correlation of 3-D volumes containing the motor components was calculated in real-space, and in their averaged 1-D power spectrum, only 13-fold symmetry was detected and only in the stator regions both above and below the inner membrane (See Supplementary Fig. V-2a). The symmetry of the other components was presumably undetectable because of the low resolution. The

average of all particles was thus 13-fold symmetrized (Fig. V-2f). The isosurface of this final "homogenous" structure is shown in Fig. V-3. The contour plot of the homogeneous motor and its 99% confidence interval is shown in Supp. Fig. V-S5 and V-S6. At the lower limit, the stator studs and stator connection regions disappear, so they have lower significance than other features.

Using the program ROTASTAT[19], the rotational correlation of individual 2-D images made by binning 3-D volumes in z was calculated in reciprocal space and judged for statistical significance. 11-, 12-, and 13-fold symmetry was detected with significance in the stator stud region above and in the membrane, and 12- and 13-fold symmetry was detected in the stator connections region below the membrane. The particles displaying strong symmetry were classified according to their stator symmetry. The 1-D power spectrum of the three symmetry classes and the unclassified group is shown in Supplementary Fig. V-2b. 13-fold symmetry appears to be dominant. The strongly 12-fold and 13-fold symmetric classes were then separately aligned, averaged, and symmetrized accordingly. The 12-fold class had eighteen members and the 13-fold class fifteen. The separate averages and symmetrized averages are shown in Supp. Fig. V-S3. The 13-fold class had more contrast-rich stator symmetry elements than the 12-fold group (cf. slices 8 and 9 in each panel of Supp. Fig. V-S3). The isosurfaces of the two "heterogeneous" final structures are shown in Supp. Fig. V-S4. In line with recent functional studies[3], the stator symmetry was at least 11. 8-fold symmetry was not detected.

The final, homogeneous, *H. gracilis* structure has thirteen studs emerging from its stator region (marked S in Fig. V-3b) that each fill a volume expected for the two OmpA domains of the two MotB proteins, unlike *T. primitia*, whose sixteen stator studs were each twenty times larger[7]. The separate 13-fold class also has prominent stator stud density that resembles the homogeneous structure, but the studs of the 12-fold class do not extend much from the membrane (Supp. Fig. V-S4). Either the 12-fold class happens to lack density, or perhaps they are truly 13-fold but have been misclassified because of low contrast. Henceforth, the homogeneous structure will be the focus. The studs extend ~ 8 nm from the membrane (Fig. V-4c), which is similar to the 7 nm length seen with *Vibrio alginolyticus* stators embedded in liposomes[17]. The center-to-center diameter of the studs above the IM is ~ 48–51 nm and the diameter of the stator connections below the IM is 42 nm, so the stators lean out ~ 16º from the center axis. The central arc length per stator is ~ 12 nm, which is large enough to accommodate the predicted dimensions of one $(MotA)_4(MotB)_2$ stator unit[20]. The center-to-center diameter of the 12-fold studs has nearly identical dimensions. The studs are right above the stator connection density (bridging density #1 in Fig. V-3b) and do not lean CCW like *T. primitia*'s[7].

The stators interact with the C ring (C in Fig. V-3b) and at least lie next to, if not interact with, the rotor (R). It is at connection #1 where the predicted, force-generating interaction between MotB and FliG of the C ring probably occurs. As in *T. primitia*, the bridging density links the stators to the outer, not the inner, rim of the C ring, in line with predictions about the position of FliG upon FliM of the C ring[21]. The C ring dimensions are comparable to those of *Salmonella*[6], but narrower in diameter than *T. primitia*'s (Fig. V-4). It is more bulbous at its bottom, thin in the middle, and wider at its

top. It sits ~ 4 nm below the IM. The bulk of the stator and the rotor (R in Fig. V-3b) is embedded in the membrane and so its borders are indistinguishable from the IM and each other, so no discrete connections are seen between stator and rotor. The edges of these components in Fig. V-4a are conjectured. The *H.g.* rotor is disk-shaped and has a smoother bottom than *Salmonella*'s. Perhaps some loosely bound proteins were removed during the biochemical isolation of *Salmonella*'s basal body to make the rotor's bottom bumpy. The approximate dimensions of the *H.g.* rotor (see Figs. 3b and 4c) are more comparable to *Salmonella*'s isolated basal body than are *T. primitia*'s. The rotor has both a supermembranous S ring and a membrane-embedded M ring, and in *Salmonella*, its respective dimensions are 24 nm and 29 nm[6], while in *T. primitia* they are 24 and 38 nm[7].

From the top of the rotor emerges the rod, which extends through the P ring (P) and presumably the L ring (L), though its density is continuous with the outer membrane (OM) and thus indistinguishable. In individual particles, the OM puckers inward toward the L ring (See Fig. V-2 b–d and Supp. Fig. V-S6), but in the average, the density is spread, presumably by randomly oriented hooks. A novel extended (E) collar lies beside the P ring and above the stator studs. At a more generous density threshold, a peptidoglycan-like density is visible between the membranes and is in line with the E collar (see Supp. Fig. V-S5). The E collar may serve as an additional bushing to aid rotation in the PG layer or as a spacer to prevent crowding of the numerous flagellar motors located at each narrow cell tip.

Below the rotor are two features with high density and low variance but with no noticeable connecting densities: a novel transport (TA) ring and an export mass. The export mass may be a ribosome parked below the rotor feeding flagellin monomers through the TA ring and rotor. The TA ring and export mass may be loosely bound to the C ring or rotor or both because they are absent from the *in vitro* basal body. Both are also present in the reconstructed flagellar motors from *T. primitia* and *Vibrio cholerae* (see Chapter 6) so their presence is not unusual. Many of the flagellar export apparatus proteins are thought to be embedded in the rotor, but FliH, I and J are located in the cytoplasm[22, 23]. FliM and FliN of the C ring bind FliJ and FliH, which in turn bind FliI. FliI is the principal export ATPase and each monomer is 50 kDa and forms a hexameric ring[24]. Assuming typical densities for proteins, were the monomer spherical, it would have a diameter of 5 nm, which is comparable to the TA ring's height. Dividing the ring into six sections, the arc length taken at the radius of the densest TA ring center is 5.5 nm, so it is plausible that the TA ring consists of a hexamer of FliI plus additional bound proteins.

The gap between the rotor and the tip of the inner face of the C ring is 6.5 nm, which is comparable to the 8 nm distance seen in *T. primitia,* but which is approximately three times longer than the ~ 2 nm gap seen in the *in vitro Salmonella* basal body[4] (see star in Fig. V-4a–b). It is believed that the rotor is connected to the C ring by FliG, whose N-terminal domain binds the rotor and whose middle and C-terminal domains bind atop FliM of the C ring[21]. Others place the middle domain on the rotor and have the 2 nm gap spanned by one alpha helix[6], but the gap seems too large in *in situ* motors to be connected that way. The similarity of FliG proteins across species[7] would suggest that

the principle cause of the discrepancy is that without the stators, whatever tether connects rotor and C ring slackens, whereas with the stators, the MotA cytoplasmic domains may push the C ring down and stretch the tether taut (Fig. V-4a–b). Illustrative of this is the manual-fitting of the *Salmonella* basal body[6] into the *H. gracilis* map in Fig. V-5, where the C ring only fit after it was lowered 4 nm from the rotor. Perhaps taut connections are necessary to insure rapid rotation and switching rates.

Methods

Hylemonella gracilis was cultivated from a rotten lily taken from a Caltech pond by placing a drop of liquid upon a 0.22 micron filter resting atop agar containing 10 mM MOPS pH 7. 0 and 0.5 g tryptone and 0.5 g yeast extract per liter. Colonies appeared several weeks later. The 16S rRNA was sequenced from a liquid culture and found to be identical to *Hylemonella gracilis*. Cultures were grown in the above media without MOPS for two days and only reached an O.D. of 0.05. The cells were checked for motility with a light microscope. The cells were then centrifuged and concentrated ten-fold in the same media, then frozen in vitreous ice with a Vitrobot (FEI Company).

Tilt series were collected using a 300 keV FEI Polara FEG TEM automated by UCSF Tomo [25]. The step size was 0.9º and ranged on average from –63º to 60º. The magnification was 34,000 (0.67 nm/pixel) and the total dose was typically ~ 78 $e^-/Å^2$, distributed according to the 1/cos scheme. The nominal defocus was 12 μm. TOMOCTF was used to estimate the experimental defocus by creating a periodogram to which a theoretical CTF was fit[18]. The tilt-series were CTF corrected using phase flipping. The actual defocus ranged from 7.5 μm to 12 μm with a mean of 10 μm (first CTF zero at 4.5 nm). Supplementary Figure V-S1 shows a CTF curve fit to one periodogram. Both the corrected and uncorrected tilt-series were reconstructed and were filtered with a

Gaussian falloff starting either at the first CTF zero or where the experimental CTF amplitude fell below 0.1. The tilt-series were binned two-fold (1.34 nm/pixel) and the tomograms were reconstructed using IMOD [26].

Fifty-nine good motor particles were computationally extracted from fifteen reconstructions in an 88 pixel, cubic volume. All were aligned in reciprocal space to the best-looking particle, using a missing-wedge mask and no object-specific real-space mask, using Bsoft's bfind program[27] and the Peach distributed computing system[28]. Alignments took around a day per particle. Each aligned particle was then refined to each particle to create fifty-nine separate averages, which were then refined to the best-looking average to create a second average, which was oriented upon the z-axis. All particles were then refined to this average to generate a third average. The dominating stator symmetry was visually 13-fold.

Rotational symmetry was detected in two ways. The E collar, P ring, rotor, stator, C ring, and TA ring components were computationally extracted with annular masks. The rotational correlation of the 3-D volumes was computed in real space for all six components of all particles, and from the matrix of coefficients versus angle, a 180 point, 1-D power spectrum was calculated. The individual spectra were then averaged for each component. Only 13-fold symmetry was detected and only in the stator regions. See Supplementary Fig. V-S2. Subsequently, the third average was 13-fold symmetrized, effectively smoothing all other apparently symmetry-less components. This symmetrized average was used as a template to again refine the alignment of all particles to create the final homogeneous average.

Rotational symmetry was also determined using ROTASTAT[19]. 2D images were generated by binning in z certain regions of the third average containing the different motor components. The "background" to which the sample images were compared was

taken from the relatively empty region between the E collar and OM. The rotational symmetry was calculated in reciprocal space and tested for statistical significance. Only the stator regions above and below the membrane had symmetry. The region above showed 11-, 12-, and 13-fold symmetry and the region below showed 12- and 13-fold symmetry. The region above was used to classify particles. Only those particles that displayed strong symmetry (more than 2-fold intensity ratio of foreground to background for a certain symmetry compared to other symmetries) were classified. The 11-fold class had 4 members, the 12-fold 18, the 13-fold 15, and those not strongly symmetric had 22 members. The symmetry of the two stator regions should match, but only 9 of 32 stator-connection predictions were identical to the stator stud region. In order to plot the symmetry of these different classes, the 1-D power spectrum was calculated as above (see Supplementary Fig. V-S2). The 12-fold class had a weaker intensity than the others. The unclassified group also had peak intensity at a symmetry of 13. Separate alignments of the 12- and 13-fold groups were made and symmetrized accordingly. Since the 12-fold group had lower intensity and lacked stator stud features, the homogeneous 13-fold group was focused upon.

In order to determine the resolution, even and odd particles were again separately aligned as above, averaged, and symmetrized 13-fold. The resolution of the entire map, including the variable membrane and cytoplasmic areas, was estimated to be 6.5 nm using the 0.5 criterion of the FSC test. The resolution of the stator and rotor region isolated with a cylindrical mask with a 3-pixel Gaussian falloff edgewidth was 5 nm, so the stator and rotor region probably has a higher resolution than the whole map. CTF correction did not improve the resolution because averages generated from particles taken from the same cells but without corrected tilt-series had the same resolution. In order to determine the statistical significance of features, a 99% confidence interval was calculated (Supplementary Fig. V-S6)[29]. The standard error map for the final

alignment average was generated. The student t-test equation was rearranged so that the true mean lies between two extremes: the experimental mean ± the standard error map times t, whose value for 59 particles for a two-tailed test at a 99% confidence level is 2.662. The extremes were then symmetrized and rescaled to have the same mean and standard deviation as the final structure, then contoured at the same level. Isosurfaces were created and distances measured with Amira (Mercury Computing Systems).

References

1. Kojima, S., and Blair, D. F. The bacterial flagellar motor: structure and function of a complex molecular machine. *Int Rev Cytol*. **233**, 93-134 (2004).
2. Berg, H. C. The rotary motor of bacterial flagella. *Annu Rev Biochem*. **72**, 19-54 (2003).
3. Reid, S. W., et al. The maximum number of torque-generating units in the flagellar motor of Escherichia coli is at least 11. *Proc Natl Acad Sci U S A*. **103**, 8066-71 (2006).
4. Francis, N. R., Sosinsky, G. E., Thomas, D., and DeRosier, D. J. Isolation, characterization and structure of bacterial flagellar motors containing the switch complex. *J Mol Biol*. **235**, 1261-70 (1994).
5. Thomas, D., Morgan, D. G., and DeRosier, D. J. Structures of bacterial flagellar motors from two FliF-FliG gene fusion mutants. *J Bacteriol*. **183**, 6404-12 (2001).

6. Thomas, D. R., Francis, N. R., Xu, C., and DeRosier, D. J. The three-dimensional structure of the flagellar rotor from a clockwise-locked mutant of Salmonella enterica serovar Typhimurium. *J Bacteriol*. **188**, 7039-48 (2006).

7. Murphy, G. E., Leadbetter, J. R., and Jensen, G. J. In situ structure of the complete *Treponema primitia* flagellar motor. *Nature*. **442**, 1062-4 (2006).

8. Sosinsky, G. E., Francis, N. R., Stallmeyer, M. J., and DeRosier, D. J. Substructure of the flagellar basal body of Salmonella typhimurium. *J Mol Biol*. **223**, 171-84 (1992).

9. Stallmeyer, M. J., Hahnenberger, K. M., Sosinsky, G. E., Shapiro, L., and DeRosier, D. J. Image reconstruction of the flagellar basal body of Caulobacter crescentus. *J Mol Biol*. **205**, 511-8 (1989).

10. Suzuki, H., Yonekura, K., and Namba, K. Structure of the rotor of the bacterial flagellar motor revealed by electron cryomicroscopy and single-particle image analysis. *J Mol Biol*. **337**, 105-13 (2004).

11. Young, H. S., Dang, H., Lai, Y., DeRosier, D. J., and Khan, S. Variable symmetry in Salmonella typhimurium flagellar motors. *Biophys J*. **84**, 571-7 (2003).

12. Khan, S., Dapice, M., and Reese, T. S. Effects of mot gene expression on the structure of the flagellar motor. *J Mol Biol*. **202**, 575-84 (1988).

13. Khan, S., Ivey, D. M., and Krulwich, T. A. Membrane ultrastructure of alkaliphilic Bacillus species studied by rapid-freeze electron microscopy. *J Bacteriol*. **174**, 5123-6 (1992).

14. Khan, S., Khan, I. H., and Reese, T. S. New structural features of the flagellar base in Salmonella typhimurium revealed by rapid-freeze electron microscopy. *J Bacteriol*. **173**, 2888-96 (1991).

15. Coulton, J. W., and Murray, R. G. Cell envelope associations of Aquaspirillum serpens flagella. *J Bacteriol*. **136**, 1037-49 (1978).

16. Blair, D. F., and Berg, H. C. Restoration of torque in defective flagellar motors. *Science*. **242**, 1678-81 (1988).

17. Yonekura, K., et al. Electron cryomicroscopic visualization of PomA/B stator units of the sodium-driven flagellar motor in liposomes. *J Mol Biol*. **357**, 73-81 (2006).

18. Fernandez, J. J., Li, S., and Crowther, R. A. CTF determination and correction in electron cryotomography. *Ultramicroscopy*. **106**, 587-96 (2006).

19. Kocsis, E., Cerritelli, M. E., Trus, B. L., Cheng, N., and Steven, A. C. Improved methods for determination of rotational symmetries in macromolecules. *Ultramicroscopy*. **60**, 219-28 (1995).

20. Braun, T. F., Al-Mawsawi, L. Q., Kojima, S., and Blair, D. F. Arrangement of core membrane segments in the MotA/MotB proton-channel complex of Escherichia coli. *Biochemistry*. **43**, 35-45 (2004).

21. Brown, P. N., Terrazas, M., Paul, K., and Blair, D. F. Mutational analysis of the flagellar protein FliG: sites of interaction with FliM and implications for organization of the switch complex. *J Bacteriol*. **189**, 305-12 (2007).

22. Ferris, H. U., and Minamino, T. Flipping the switch: bringing order to flagellar assembly. *Trends Microbiol*. **14**, 519-26 (2006).

23. Gonzalez-Pedrajo, B., Minamino, T., Kihara, M., and Namba, K. Interactions between C ring proteins and export apparatus components: a possible mechanism for facilitating type III protein export. *Mol Microbiol*. **60**, 984-98 (2006).

24. Claret, L., Calder, S. R., Higgins, M., and Hughes, C. Oligomerization and activation of the FliI ATPase central to bacterial flagellum assembly. *Mol Microbiol*. **48**, 1349-55 (2003).

25. Zheng, Q. S., Braunfeld, M. B., Sedat, J. W., and Agard, D. A. An improved strategy for automated electron microscopic tomography. *J Struct Biol*. **147**, 91-101 (2004).

26. Kremer, J. R., Mastronarde, D. N., and McIntosh, J. R. Computer visualization of three-dimensional image data using IMOD. *J Struct Biol*. **116**, 71-6 (1996).

27. Heymann, J. B., and Belnap, D. M. Bsoft: image processing and molecular modeling for electron microscopy. *J Struct Biol*. **157**, 3-18 (2007).

28. Leong, P. A., Heymann, J. B., and Jensen, G. J. Peach: a simple Perl-based system for distributed computation and its application to cryo-EM data processing. *Structure*. **13**, 505-11 (2005).

29. Frank, J. *Three-Dimensional Electron Microscopy of Macromolecular Assemblies.* Oxford University Press, Inc., New York (2006).

Acknowledgements We thank Eric Matson for guiding and performing the identification of the strain. This work was supported in part by NIH grants P01 GM66521 and R01 AI067548 to G.J.J., DOE grant DE-FG02-04ER63785 to G.J.J., a Searle Scholar Award to G.J.J., NSF grant DEB-0321753 to J.R.L., NIH graduate fellowship F31 EB 004179 to G.E.M., and gifts to Caltech from the Ralph M. Parsons Foundation, the Agouron Institute, and the Gordon and Betty Moore Foundation.

Author Contributions G.E.M. collected/analysed the data and drafted the text and figures; J.R.L. provided the cell culture and discourse, E.G.M. identified the species and G.J.J. guided the research and manuscript editing throughout.

Author Information The averaged and symmetrized structure will be deposited in the EM Data Bank (http://www.ebi.ac.uk/msd/index.html).

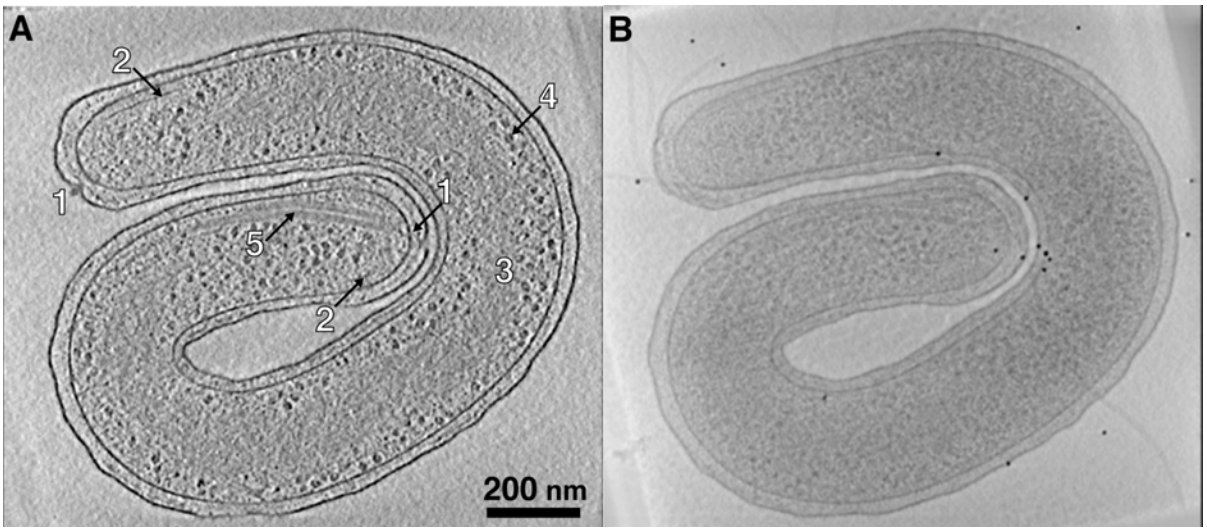

Figure V-1. A reconstructed *H. gracilis* bacteria

A. The flagellar motors (1) are located at the cell tips, as are the chemotaxis arrays (2). A ribosome-excluded region snakes through the middle (3). Ribosome-like particles are more common near the periphery (4). Some cells had flagellar-like filaments in their cytoplasm (5). B. Projection of the whole reconstruction. One to four flagella extend from *H. gracilis'* tip.

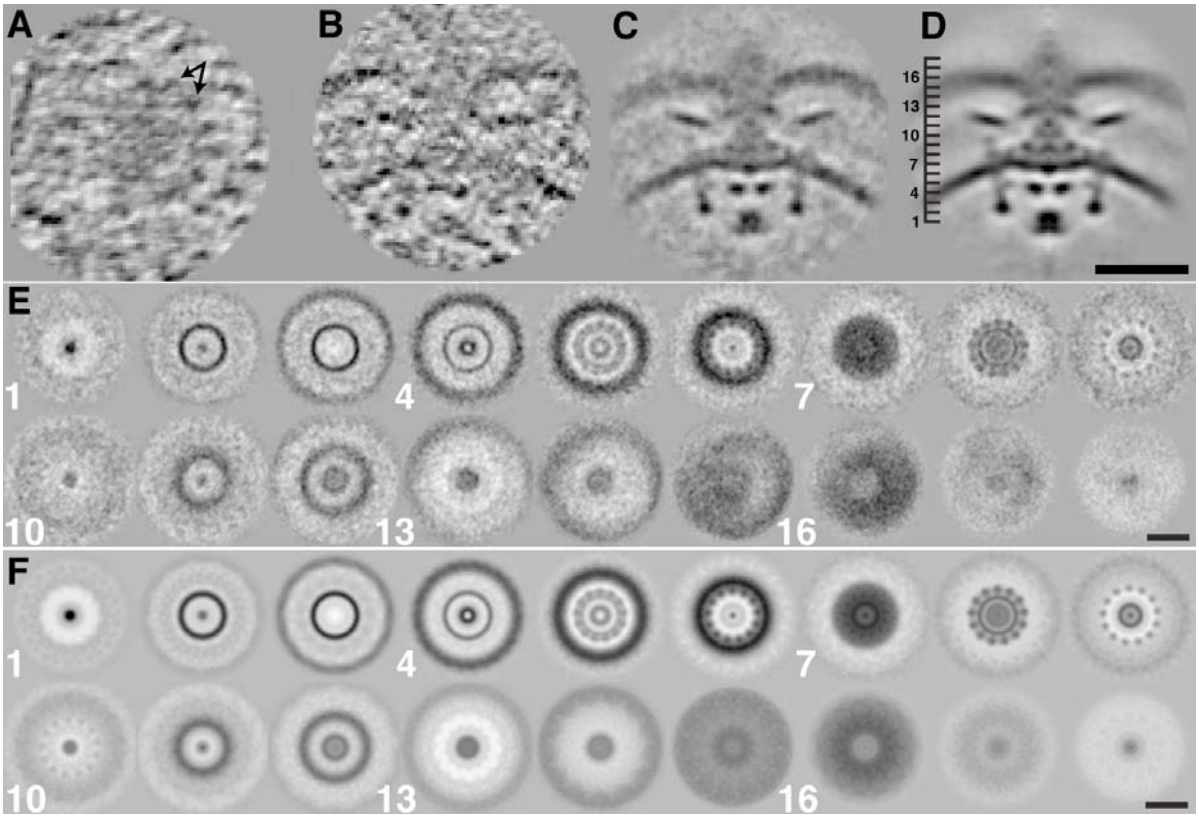

Figure V-2. Sections through the average and 13-fold symmetrization of all particles.

A. Radial section through the stator region of an individual particle at ruler height 8. Arrows point to stator symmetry elements. B. Axial section through another individual particle. C. Axial section through the “homogeneous” mean. D. Symmetrized mean. The sections in panels A through D are 1.34 nm-thick. E. 4 nm-thick serial sections through the mean structure. The numbered slices correspond to the ruler beside panel D. F. 4 nm-thick serial sections through the 13-fold symmetrized mean. (All scale bars are 40 nm.)

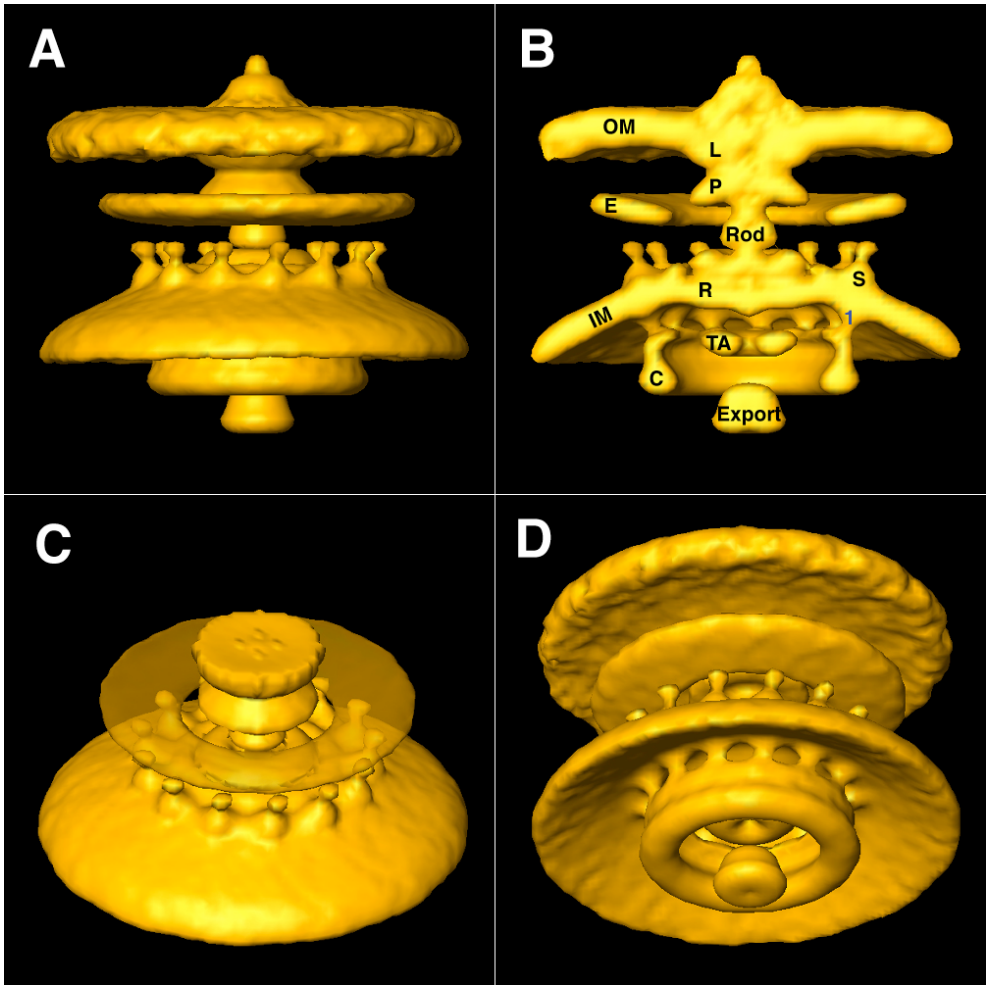

Figure V-3. Isosurface of the averaged and 13-fold symmetrized flagellar motor.

A. View along the membrane. B. Cutaway. The rotor (R) and stators (S) are embedded in the inner membrane (IM) and the C ring (C) connects to the stators through bridging density 1. The rod extends up through the P ring (P) and presumably the L ring (L), though its density is continuous with the outer membrane (OM). The extended collar (E) is novel and lies in the expected plane of the peptidoglycan layer. The transport ring (TA) is also novel and may function in assembly. The export mass may be a ribosome. C. View from the periplasm with the OM removed and the E collar transparent. D. View from the

cytoplasm. Notice that the stator studs and connections are both 13-fold symmetric.

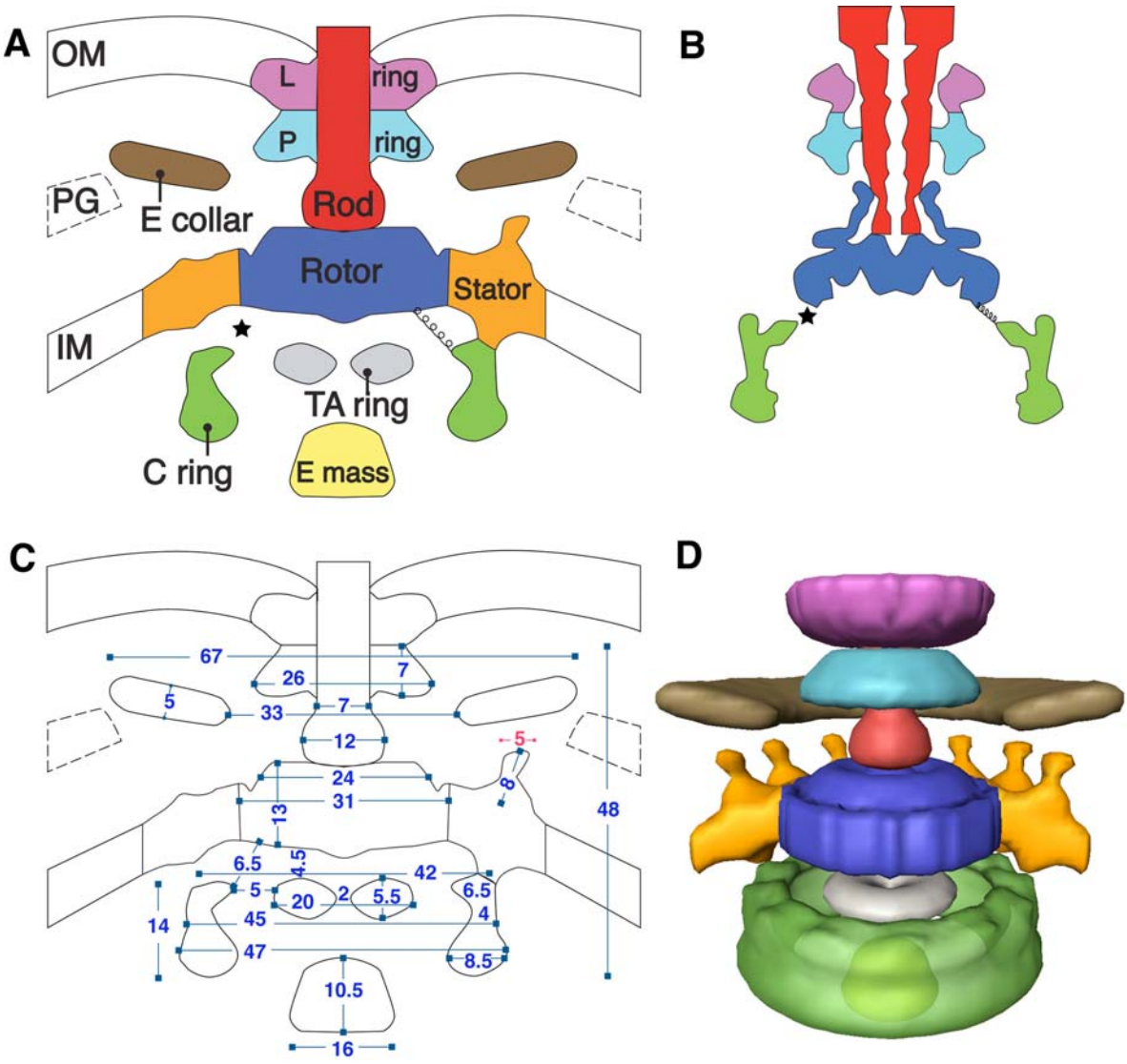

Figure V-4. The components of the flagellar motor

A. Cartoon of the *in situ*, *H. gracilis* motor. The shape of the L ring and the borders of the rotor and stators are conjectured because density was continuous and inseparable from the membranes. B. The similarly colored and scaled motor components of the *in vitro*, *Salmonella* basal body. The starred gap between rotor and C ring is expected to be bridged by some tether, though the gap is about three times longer in the *in situ* motor than the *in vitro* one. C. Measurements of interesting features of the *H. gracilis* motor. The pink

dimension is not to scale, but the stator studs are 5 nm wide. D. The masked-out motor components of the *H. gracilis* map.

Figure V-5. The *Salmonella* basal body fit into *H. gracilis'* motor

The basal body fits plausibly into the *in situ* map only after the C ring is lowered 2.8 nm from the rotor.

Supplementary Information

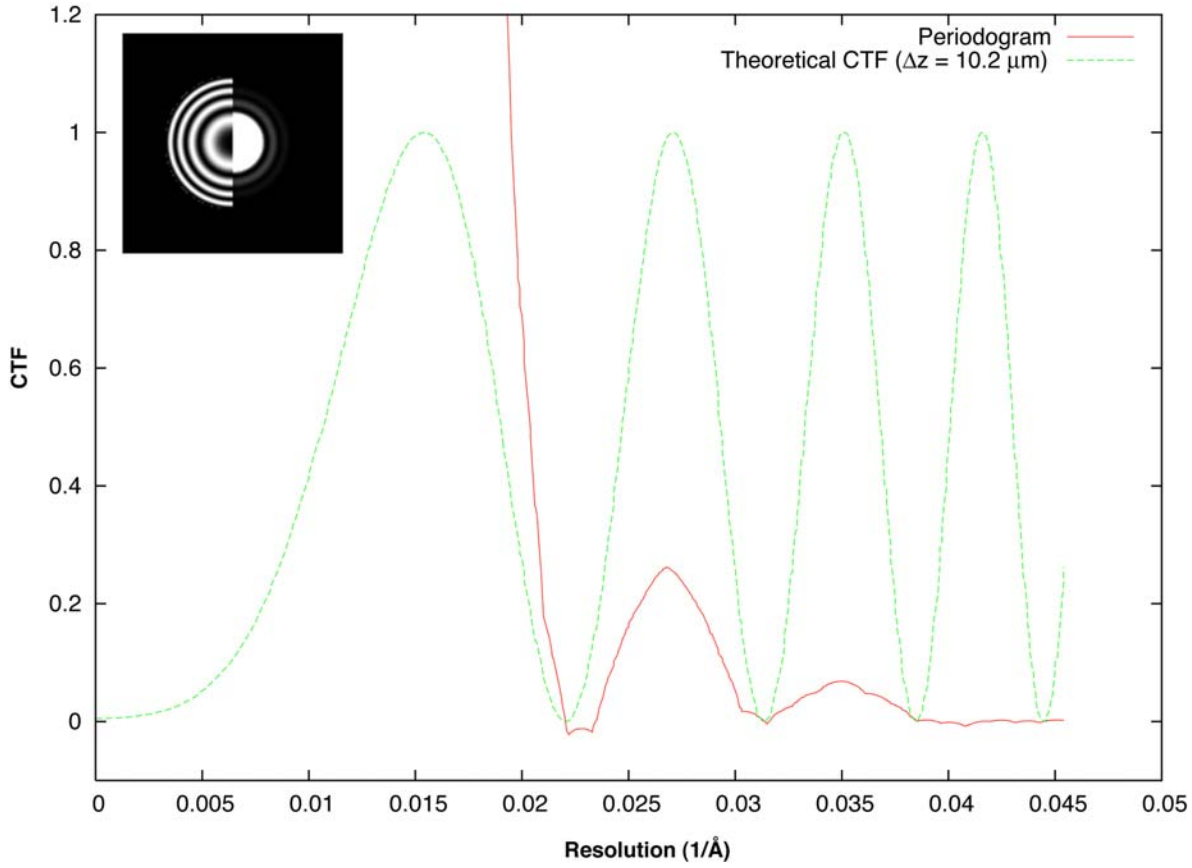

Supplementary Figure V-S1. CTF fitting of a tilt series

From a periodogram generated from a tomographic tilt series, a theoretical CTF curve was fit. The defocus was determined to be 10.2 μm. The information content past the first zero is low, however. The inset shows the theoretical CTF beside the experimental periodogram.

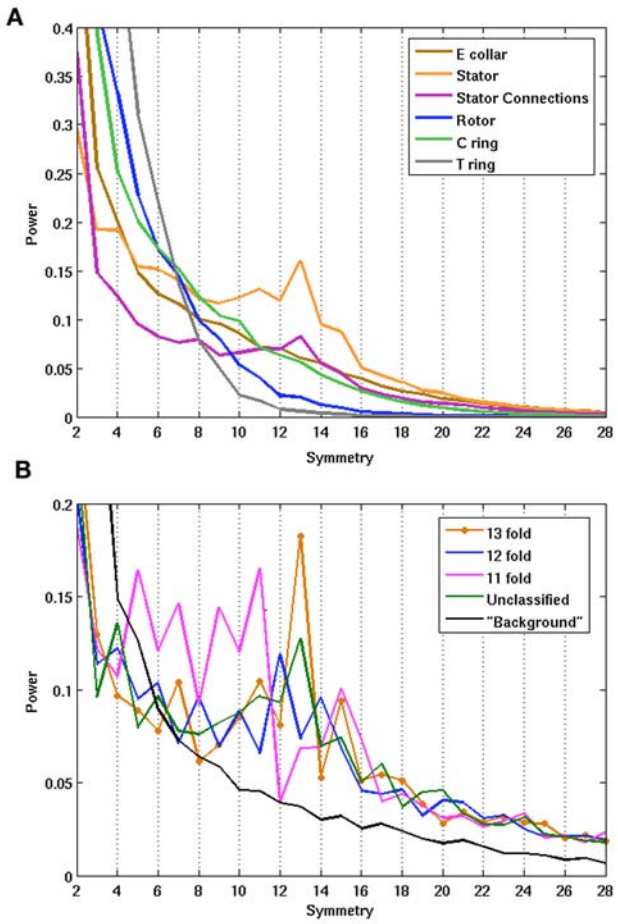

Supplementary Figure V-S2. Rotational power spectrum of motor parts to determine symmetry

A. When the rotational correlation of several excised, 3-D motor regions was calculated in real space, only 13-fold symmetry was detected, and it resided in the stator regions. B. When the rotational power spectrum was calculated in reciprocal space on binned, 2-D images of the same regions using Rotastat, 11-, 12-, and 13-fold symmetry was detected only in the stator regions. The power of the stator stud region from separately classified particles is plotted individually and compared to the power of the "background," which came from an empty periplasmic region from as many particles. (n.b.: Ordinates are scaled differently.)

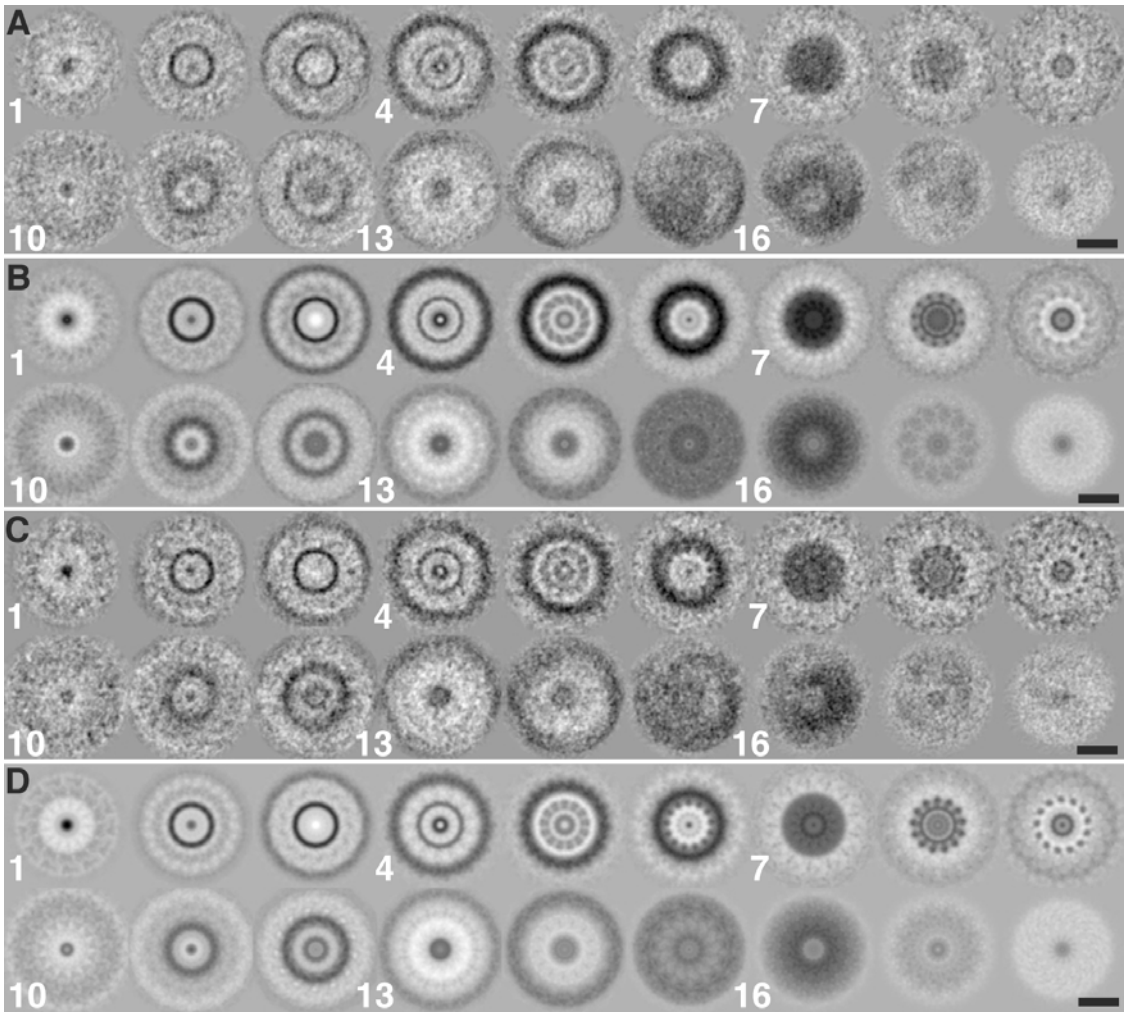

Supplementary Figure V-S3. Serial sections through the 12-fold and 13-fold class means

All sections are 4 nm thick and the numbers correspond to the ruler of Figure V-2 D. A. The 12-fold class mean. B. The 12-fold symmetrized class mean. C. The 13-fold class mean. D. The 13-fold symmetrized class mean. (All scale bars are 40 nm.)

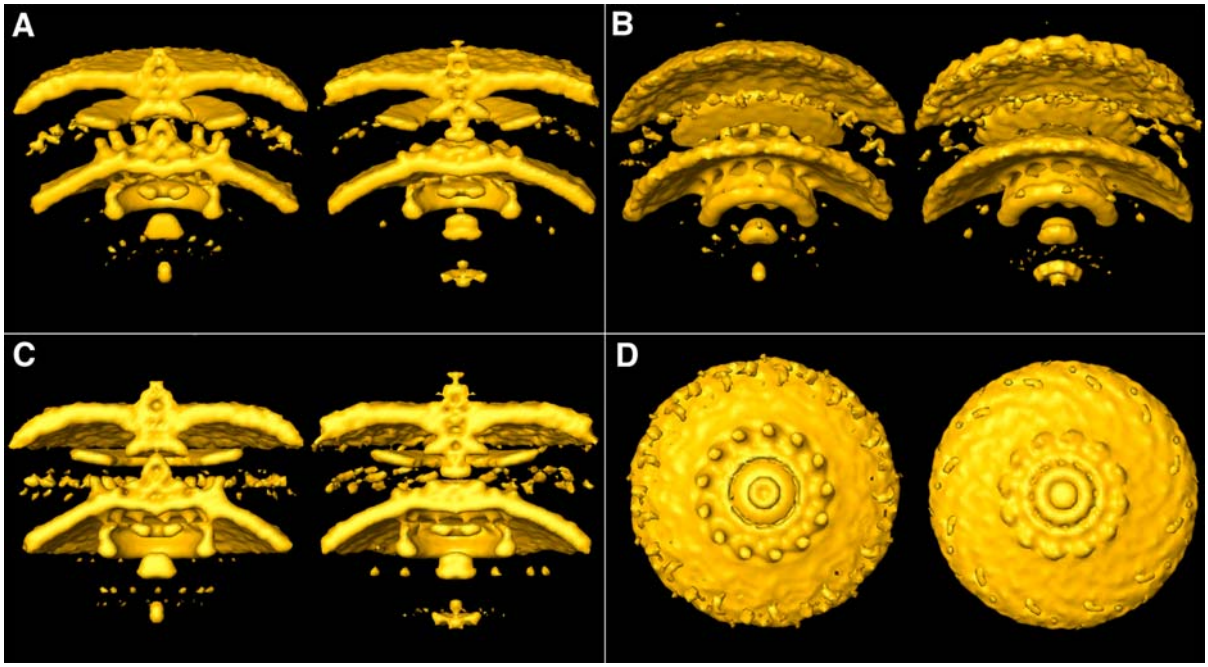

Supplementary Figure V-S4. Comparative isosurfaces of the 13-fold and 12-fold classes

The 13-fold class is on the left, the 12-fold class on the right. A. View from the periplasm. Notice that the 12-fold class lacks as much stator stud density. B. View from the cytoplasm. The respective symmetry is maintained in the stator region both above and below the membrane. C. View along membrane. D. View from above. Notice the pronounced stator stud density in the 13-fold class.

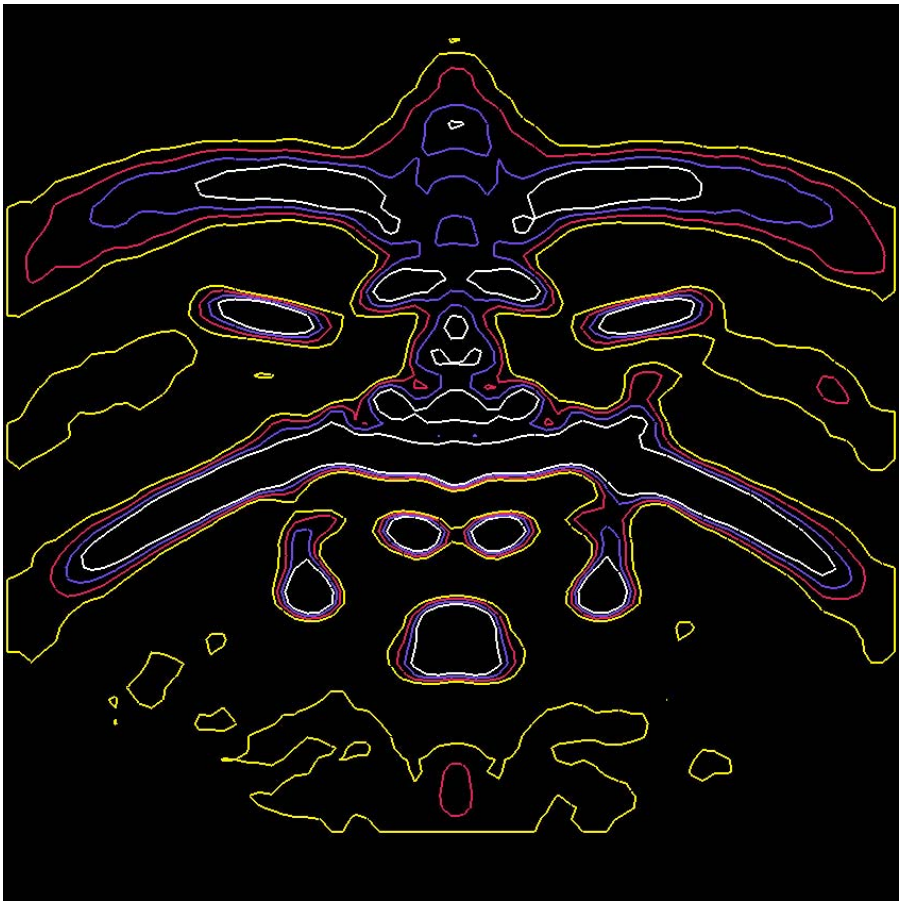

Supplementary Figure V-S5. Isolines of the *H. gracilis* flagellar motor

The high and low densities of the symmetrized mean are represented from white to yellow contours. The red line is the chosen contour for the presented isosurfaces. The blue and white contours are 2 and 3 times less generous in density, and the yellow line is 100% more generous. Notice the density in the PG region contacts the E collar and points towards the stator studs.

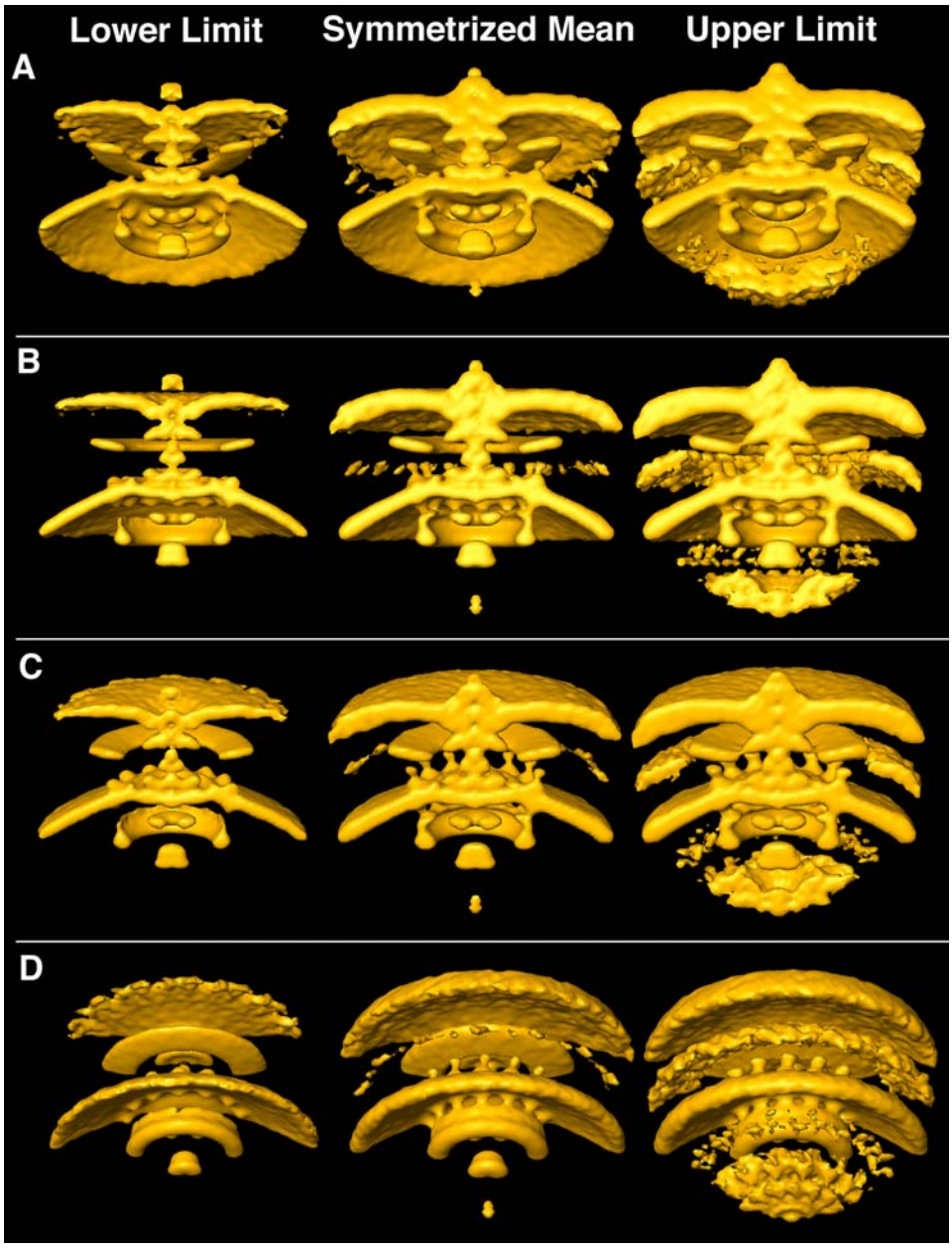

Supplementary Figure V-S6. Statistical confidence interval of the homogeneous final structure

A-D show different views of three maps: the experimental, symmetrized mean and the (subsequently symmetrized) lower and upper limits of the 99% confidence interval. The true mean lies within these limits with the stated confidence.

Chapter VI

Comparison of several *in situ* flagellar motors

Gavin E. Murphy, Ariane Briegel, Zhuo Li, D. Prabha Dias,

Gregory P. Henderson, Bingni Wen, Grant J. Jensen

Abstract

The flagellar motor is a tiny nanomachine that can spin at speeds of 60 to 1000 Hz yet occupies a space boxed by a 50 to 70 nm sided cube. Most of our information of it either comes from reconstructions of the *in vitro Salmonella* basal body or traditional electron microscopy images of stained, sectioned, or frozen-etched cells: on one end, a high-resolution, 3-D structure of the basal body stripped from its context; and on the other end, low-resolution, 2-D structure-pieces taken from traumatized cells and fraught with artifacts. Filling this gap are cryoelectron reconstructions of *in situ* flagellar motors. From few particles, the *Vibrio cholerae* and *Caulobacter crescentus* motor structures are presented in 3-D and compared to the better resolved *Treponema primitia* and *Hylemonella gracilis* motors. The variability suggests that structures taken from other bacterial species may display more novel or unusual features.

Introduction

The flagellar motor is interesting not just to scientists but to the public as well, because its remarkable abilities and beautiful structural components inspire the question of design. Darwinian evolution's explanation that such pieces gradually took shape and gradually came together seems unlikely initially because the finished product is so perfect-looking[1]. Experts conflict over whether the flagellar motor came from the type III secretion system (T3SS), which it resembles, or vice versa. Perhaps the gradualist explanation seems insufficient because only two structures are often compared: *Salmonella*'s basal body and T3SS[2, 3]. The structure determination of *T. primitia*'s flagellar motor and that of others shows that the flagellar motor is different across

species[4]. Divergence, if not emergence, can be shown graphically by comparison. Three-dimensional information is necessary to determine the true differences in structure.

Over the decades, traditional electron microscopists have extracted flagellar basal bodies from many organisms, displayed their best images and measured the heights and diameters of the salient motor components[5-16]. Their measurements are compiled in Table VI-1, along with the author's. The images suffer from variability of stain and their 2-D nature. The measurements are just estimates, and some stand out as unusually small or large.

Electron cryotomography is a better technique, because with several tilt series a reconstruction of several complete bacterial cells can be generated and, what is more, identical macromolecular machines—too labile to purify or crystallize—can be computationally-extracted and averaged together to produce a higher resolution structure. This has been done with reconstructions of *Vibrio cholerae* and *Caulobacter crescentus* obtained from lab coworkers.

Results

Five good motor particles were extracted from five reconstructions of *Caulobacter crescentus*, aligned and averaged. No symmetry was detectable in the stator region, but 12-fold symmetry was applied to boost the signal-to-noise ratio. The final structure is shown in Figure VI-1. The low density of many features is visible in Figure VI-1B, where the contours are incremented in units of 78% of the standard deviation, with the white contour representing three times the standard deviation. The red contour was chosen for the isosurfaces in Figures VI-1C–D.

Instead of discrete stator studs, a ring of density was seen above the membrane over the C ring with a central diameter of 41 nm ("S" in Figure VI-1D). The outer diameter of the C ring ("C") is 42 nm, which supports the identity of the stator ring, since it is expected and (so far) always seen by the author, that the stator studs are right above the C ring. The resolution is insufficient to separate the C ring from the membrane. The density below the rotor is noisier than *H. gracilis*' but may contain an export (E) mass. The rotor ("R") density is continuous with the stator and inner membrane (IM) densities so its size is not measurable. Delineating the P and L ring is difficult because their density is continuous with each other and the outer membrane (OM), but there is a narrower ring in the expected peptidoglycan layer under a wider membranous ring. This is similar to the single particle reconstruction of the *Caulobacter* basal body, whose P ring appears slightly narrower than the L ring[17]. The rod extends upwards past the OM because it must transit the proteinaceous S layer.

Four good motor particles were extracted from four reconstructions of *V. cholerae*, aligned and averaged. No stator density was present, but the reconstruction was 12-fold symmetrized to improve the signal-to-noise ratio. The final structure is shown in Figure VI-2. The contours of the structure are shown in Figure VI-2B, which show that the *V. cholerae* motors are more contrast-rich than *Caulobacter*'s. The contours are incremented in standard deviation units, with the white contour representing 3.5 times the standard deviation. The red contour was chosen for the isosurfaces in Figures VI-1C–D. The outer diameter of the C ring is 46 nm. The resolution is insufficient to separate the C ring from the membrane. Below the rotor are two connected densities. These resemble the TA ring and export mass of *H. gracilis* (Chapter

5). The rotor is embedded in the membrane, so its borders are indeterminable. The bushings of *V. cholerae* are unusual compared to other species'. Negatively-stained images of the *V. alginolyticus* basal body revealed that the two P and L rings are half as high (3 nm) as *Salmonella*'s and are positioned over a novel T ring 31 nm in diameter[18]. In the same paper, they identified the T ring as consisting of MotX and MotY. A similar umbrella-shaped overhang is present in *V. cholerae*, but its outer diameter is 38 nm. It has been labeled a T ring in Figure VI-2D. Also unusual is the depression in which the rings sit in the outer membrane (OM). This may be an artifact of the low sample size or perhaps the L ring is truly small in height and connects with a tiny fraction of the OM to produce such a depression.

Discussion

The four *in situ* flagellar motors are compared to the *Salmonella* basal body[3, 19-21] in Figure VI-3. Each one is different: either a new structure is present or their dimensions are wider or narrower than *Salmonella*. The general features are tabulated in Table VI-2. Where previous research has made measurements of the four species, they will be compared. The chief insight is that the motors will need to be classified into groups: some may have wide bowl rotors, others narrower disk rotors; some will have P and L rings, others P collars. More discoveries await.

The principle discovery is the stator region and its symmetry. With ECT, 16 stator studs were seen in *T. primitia*[4] and 11–13 in *H. gracilis*. With freeze-etch microscopy, the maximum number of studs was either 12 or 16. The average number of studs in *Aquaspirillum serpens* and *Streptococcus* was 15 and ranged between 14 to 16[6,

10]. *E. coli* had an average of 11 and a range between 10 and 12[10]. *Bacillus firmus* had an average of 9 and a maximum of 12[11], and *Salmonella* had about 12 also[12]. The central diameters of the ring of stators give us an idea of the arc length per stator unit. For *T.p.*, *H.g.*, and *C.c.*, the central diameters are approximately 61, 48–51 and 41 nm, respectively, varying by 10 nm around *H.g.* The arc length per stud, where known, is ~ 12 nm for *T.p.* and *H.g.* Each stator unit is made from a complex of 4 MotA proteins, each containing 4 transmembrane (TM) alpha helices, and 2 MotB proteins, each having 1 TM helix. If one assumes a transmembrane helix is 1 nm in width, and that the MotA/B complex is arranged as predicted[22], with the 4 transmembrane helices of MotA surrounding the two transmembrane helices of MotB, then the complex is about 6 nm in diameter. Estimates of the stator dimensions from negatively stained, freeze-etch images seem too narrow given *Salmonella*'s standard rotor diameter of 31 nm. The outer and inner diameters of the stator studs in *B. firmus*, *E. coli*, and *Streptococcus* were 33 and 23 nm, 34 and 20 nm, and 40 and 26 nm, respectively[10, 11]. The inner diameter of the stator studs in *Salmonella* was 28 nm[12]. The dimensions of the stator studs should conform to the rough dimensions of the two OmpA domains of MotB. The height and girth of the studs were measured in *T.p.* and *H.g.* to be 9 and 7 nm, and 8 and 5 nm, respectively. Compared to the volume two OmpA domains, the *T.p.* stud volume was twenty times larger, but *H.g.*'s was approximately equal. They were 7 nm in girth in *B. firmus*, *E. coli*. and *Streptococcus* and 5 nm in *A. serpens*[6, 10, 11].

The *T.p.* stators are the most unusual. Their studs have connecting density between them and the presence of the P collar on the stators might suggest that all are needed to be present to support the P collar. This does not seem likely though, as

functional studies of *E. coli* and *Streptococcus* motors have proven that a full-complement of stators is not required to turn the rotor[23], and the number of stator studs in freeze-etch images even varies between motors within the same cell. Another oddity of *T.p.* is that the MotA/B complex is expected to be 2-fold symmetric[22], but the connecting, finger-like density between the stators and the top rim of the rotor is not, or else such density would be visible on the outer diameter of the studs. This suggests there are unknown adaptor proteins between the stators and the rotor, which might also serve to connect the P collar and stators.

In all reconstructions there is either symmetric or continuous connecting density between the C ring and the stator region of the IM. Three of the *in situ* motors had C ring diameters near *Salmonella*'s except *T.p.*, which had a 64 nm wide C ring. The C rings extended about 15–20 nm into the cytoplasm from the IM.

A dense structure labeled an export mass is present below the rotor in all structures and may be a ribosome feeding flagellin monomers through either a transport apparatus (TA) ring present in nearly all structures or perhaps through the rotor. In older EM images, "insertion pores" were seen under the rotor with a diameter of ~ 10 nm in *Caulobacter*, *Salmonella*, and *Spirochaeta aurantia* rotors[17, 24, 25]. The TA rings in *T.p.* and *H.g.* are wider, at ~ 20 nm.

The rotor is embedded in the IM and so its borders are indistinguishable except in *T.p.* There are two clear rims that may correspond to the membrane (M) and supermembranous (S) rings. It is unclear whether the stators in narrower motors also have connecting density to the rotor. The chief difference in rotors is the wide bowl rotor in *T.p.* and the normal-sized, disk rotors in everything else. *T. primitia*'s top rim diameter

of 24 nm is comparable to the S ring values in other organisms, but its bottom rim is much wider, at 38 nm. In *Salmonella* and *Caulobacter* reconstructions, the M and S rings have diameters of 26.5 and 27.5 nm, and 24 and 28 nm, respectively[17, 26]. In 2D EM images of the basal bodies in *A. serpens*, *Campylobacter fetus*, *Wolinella succinogenes*, and *E. coli*, the M and S rings have diameters of 31 and 28 nm, 26 and 26 nm, 30 and 30 nm, and 22.5 and 22.5 nm, respectively[6, 10, 14]. One unexpected discovery is the distance between the C ring and rotor in *in situ* versus *in vitro* reconstructions. There is no visible connecting density even in the higher-resolution *in vitro* reconstruction, and the gap is ~ 2 nm[3]. See the star and tethers drawn in Figure VI-3. In *H.g.* and *T.p.* the gap is ~ 3 times longer, so whatever tether connects them must be stretched in the *in situ* motor.

Another difference resides in the peptidoglycan and outer membrane bushings: the P and L rings. Although their density is continuous with each other and the OM, the general outline reveals small differences between the gram negative bacteria, and large differences between them and *T.p.* In *C.c.*, the L ring is wider than the P ring in both the *in situ* reconstruction and the *in vitro* one[17]. The L and P rings in *Vibrio* are thinner, and underneath them is an overhanging T ring[18]. In *H.g.*, the P ring appears to be supplemented with an extended E collar. The biggest difference is the P collar in *T.p.* The presence of a P collar instead of a P ring is a manifestation of the lack of FlgI in the genomes of *Treponema*, but the gene responsible for the P collar is unknown[27]. The P ring would restrict the tilt of the flagellum rod to a nearly vertical orientation, but the P collar would permit a wider range of bending of the rod and hook. In addition to genetic evidence, there are two images of *Spirochaeta stenostrepta* insertion pores which show a

shape resembling a P collar[7]. Interestingly, Firmicutes also lack FlgI, so it is tempting to speculate that Firmicutes have a P collar also. Since the P collar is twice as high as *Salmonella*'s P ring, maybe the P collar would suffice to create a pore opening in the thicker peptidoglycan layer of gram positive bacteria.

The motors probably do not partition into two neat categories with wide rotors and P collars or narrow rotors and P rings. *Borrelia* and *Leptospira* both appear to have wide rotors in EM images but both have the P ring gene[27]. Curiously, *Leptospira* also has an L ring gene even though its flagella never exit the periplasm. It may be that there are a wide variety of motor attachments and component versions present in the bacterial world.

Methods

Image processing was carried out as described before[4].

References

1. Pallen, M. J., and Matzke, N. J. From The Origin of Species to the origin of bacterial flagella. *Nat Rev Microbiol.* **4**, 784-90 (2006).
2. Marlovits, T. C., et al. Structural insights into the assembly of the type III secretion needle complex. *Science.* **306**, 1040-2 (2004).
3. Thomas, D. R., Francis, N. R., Xu, C., and DeRosier, D. J. The three-dimensional structure of the flagellar rotor from a clockwise-locked mutant of Salmonella enterica serovar Typhimurium. *J Bacteriol.* **188**, 7039-48 (2006).

4. Murphy, G. E., Leadbetter, J. R., and Jensen, G. J. In situ structure of the complete Treponema primitia flagellar motor. *Nature*. **442**, 1062-4 (2006).

5. Abram, D., Vatter, A. E., and Koffler, H. Attachment and structural features of flagella of certain bacilli. *J Bacteriol*. **91**, 2045-68 (1966).

6. Coulton, J. W., and Murray, R. G. Cell envelope associations of Aquaspirillum serpens flagella. *J Bacteriol*. **136**, 1037-49 (1978).

7. Holt, S. C., and Canale-Parola, E. Fine structure of Spirochaeta stenostrepta, a free-living, anaerobic spirochete. *J Bacteriol*. **96**, 822-35 (1968).

8. Hovind-Hougen, K., Birch-Andersen, A., and Jensen, H. J. Ultrastructure of cells of Treponema pertenue obtained from experimentally infected hamsters. *Acta Pathol Microbiol Scand [B]*. **84**, 101-8 (1976).

9. Jackson, S., and Black, S. H. Ultrastructure of Treponema pallidum Nichols following lysis by physical and chemical methods. II. Axial filaments. *Arch Mikrobiol*. **76**, 325-40 (1971).

10. Khan, S., Dapice, M., and Reese, T. S. Effects of mot gene expression on the structure of the flagellar motor. *J Mol Biol*. **202**, 575-84 (1988).

11. Khan, S., Ivey, D. M., and Krulwich, T. A. Membrane ultrastructure of alkaliphilic Bacillus species studied by rapid-freeze electron microscopy. *J Bacteriol*. **174**, 5123-6 (1992).

12. Khan, S., Khan, I. H., and Reese, T. S. New structural features of the flagellar base in Salmonella typhimurium revealed by rapid-freeze electron microscopy. *J Bacteriol*. **173**, 2888-96 (1991).

13. Khan, S., Zhao, R. B., and Reese, T. S. Architectural features of the Salmonella typhimurium flagellar motor switch revealed by disrupted C-rings. *Journal Of Structural Biology*. **122**, 311-319 (1998).

14. Kupper, J., Wildhaber, I., Gao, Z., and Baeuerlein, E. Basal-body-associated disks are additional structural elements of the flagellar apparatus isolated from Wolinella succinogenes. *J Bacteriol*. **171**, 2803-10 (1989).

15. Nauman, R. K., Holt, S. C., and Cox, C. D. Purification, ultrastructure, and composition of axial filaments from Leptospira. *J Bacteriol*. **98**, 264-80 (1969).

16. Paster, B. J., and Canale-Parola, E. Involvement of periplasmic fibrils in motility of spirochetes. *J Bacteriol*. **141**, 359-64 (1980).

17. Stallmeyer, M. J., Hahnenberger, K. M., Sosinsky, G. E., Shapiro, L., and DeRosier, D. J. Image reconstruction of the flagellar basal body of Caulobacter crescentus. *J Mol Biol*. **205**, 511-8 (1989).

18. Terashima, H., Fukuoka, H., Yakushi, T., Kojima, S., and Homma, M. The Vibrio motor proteins, MotX and MotY, are associated with the basal body of Na-driven flagella and required for stator formation. *Mol Microbiol*. **62**, 1170-80 (2006).

19. Francis, N. R., Sosinsky, G. E., Thomas, D., and DeRosier, D. J. Isolation, characterization and structure of bacterial flagellar motors containing the switch complex. *J Mol Biol*. **235**, 1261-70 (1994).

20. Thomas, D., Morgan, D. G., and DeRosier, D. J. Structures of bacterial flagellar motors from two FliF-FliG gene fusion mutants. *J Bacteriol*. **183**, 6404-12 (2001).

21. Thomas, D. R., Morgan, D. G., and DeRosier, D. J. Rotational symmetry of the C ring and a mechanism for the flagellar rotary motor. *Proc Natl Acad Sci U S A*. **96**, 10134-9 (1999).

22. Braun, T. F., Al-Mawsawi, L. Q., Kojima, S., and Blair, D. F. Arrangement of core membrane segments in the MotA/MotB proton-channel complex of Escherichia coli. *Biochemistry*. **43**, 35-45 (2004).

23. Berg, H. C. The rotary motor of bacterial flagella. *Annu Rev Biochem.* **72**, 19-54 (2003).

24. Katayama, E., Shiraishi, T., Oosawa, K., Baba, N., and Aizawa, S. Geometry of the flagellar motor in the cytoplasmic membrane of Salmonella typhimurium as determined by stereo-photogrammetry of quick-freeze deep-etch replica images. *J Mol Biol*. **255**, 458-75 (1996).

25. Brahamsha, B., and Greenberg, E. P. Biochemical and cytological analysis of the complex periplasmic flagella from Spirochaeta aurantia. *J Bacteriol*. **170**, 4023-32 (1988).

26. Sosinsky, G. E., Francis, N. R., Stallmeyer, M. J., and DeRosier, D. J. Substructure of the flagellar basal body of Salmonella typhimurium. *J Mol Biol.* **223**, 171-84 (1992).

27. Pallen, M. J., Penn, C. W., and Chaudhuri, R. R. Bacterial flagellar diversity in the post-genomic era. *Trends Microbiol.* **13**, 143-9 (2005).

Author Contributions G.E.M. collected some data, analyzed all the data, and drafted the text and figures. A.B., Z.L., D.P.D., G.P.H. and B.W. provided most of the data. G.J.J supervised all the work.

Figures

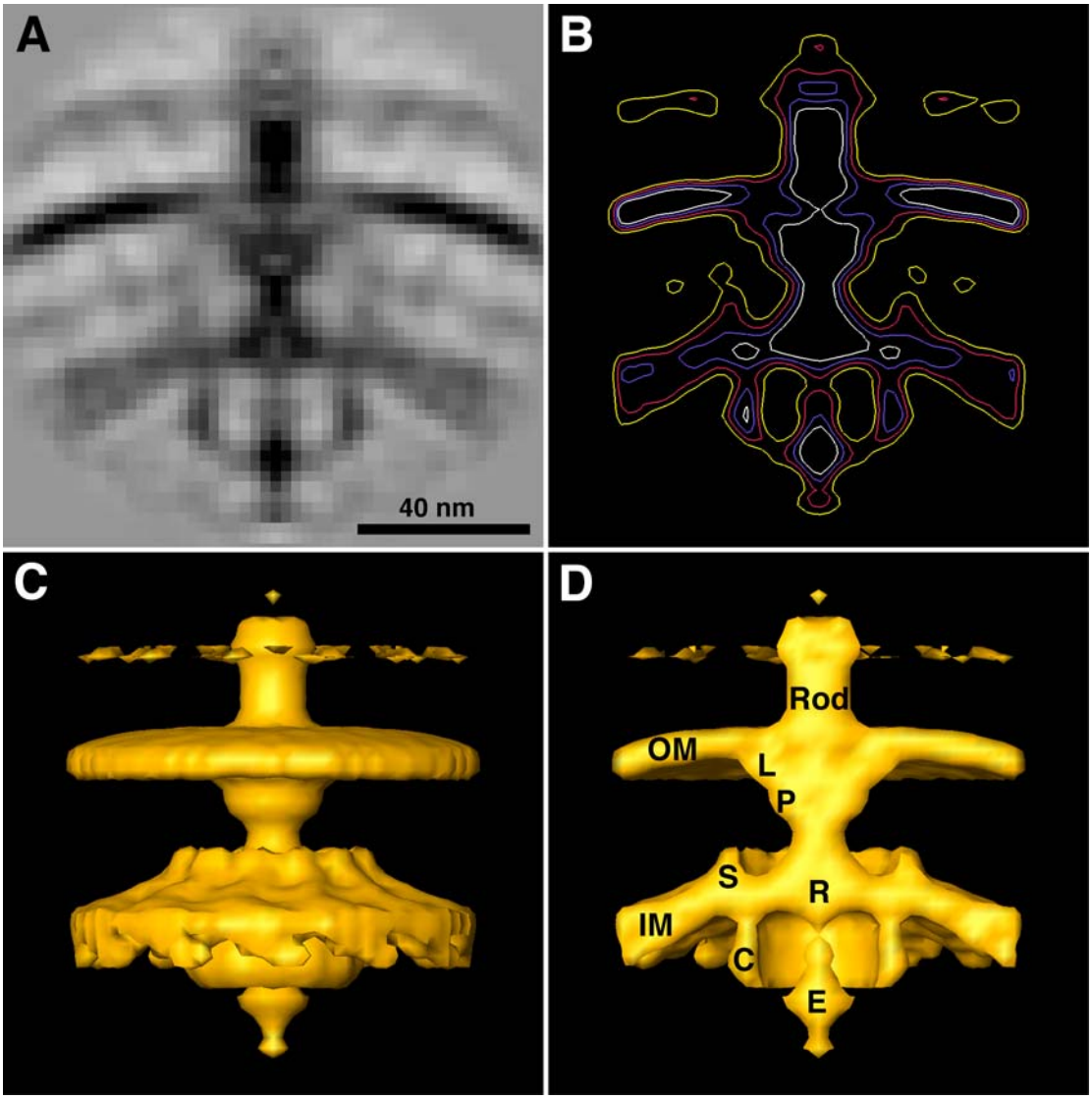

Figure VI-1. ***Caulobacter crescentus*** **flagellar motor**

A. 2.4 nm-thick axial section through the 12-fold symmetrized motor. B. Contours through the symmetrized motor. The red contour was chosen for isosurfacing. C. Side view isosurface of the motor. D. Cutaway of the motor.

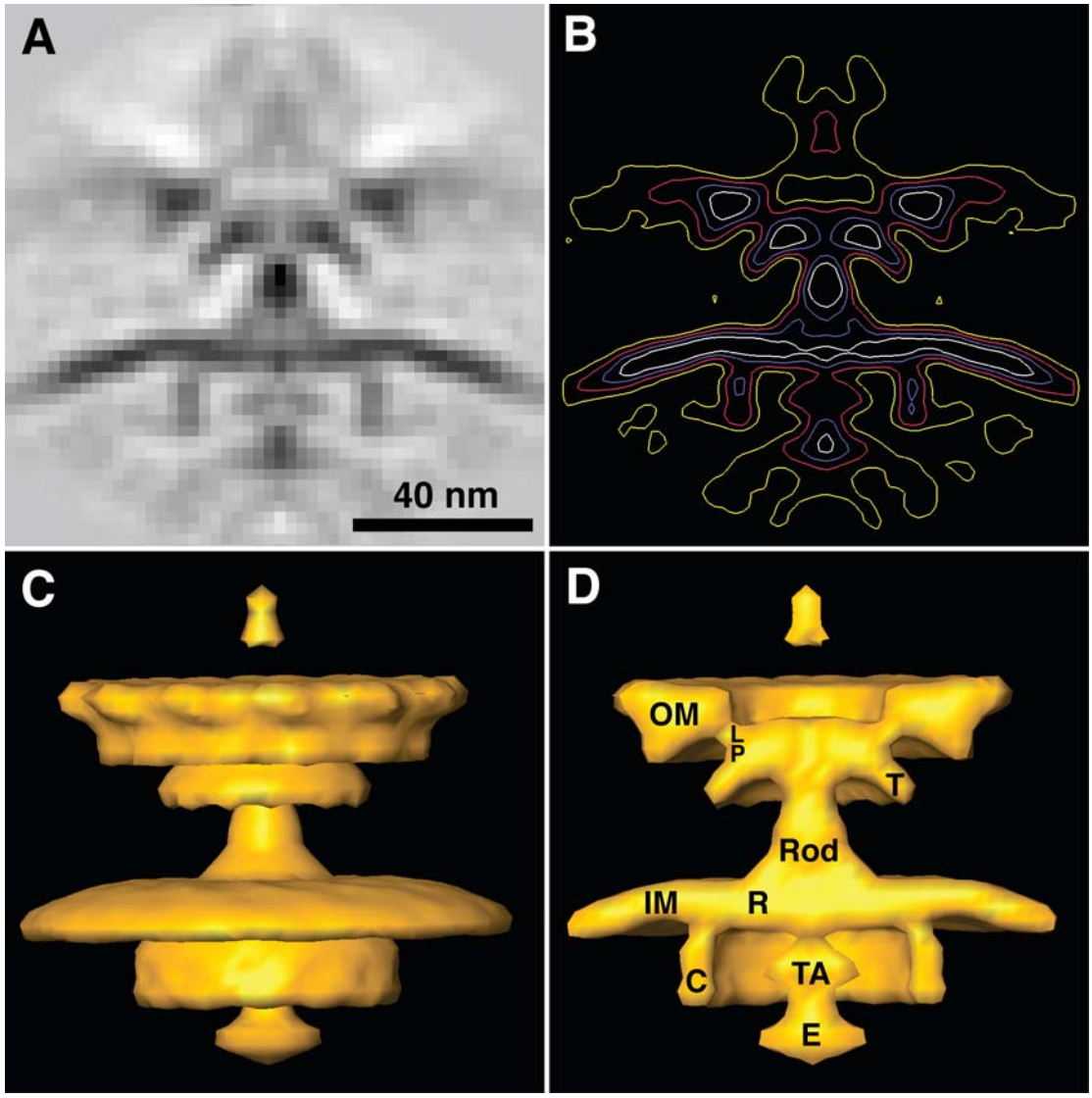

Figure VI-2. ***Vibrio cholerae*** **flagellar motor**

A. 2.4 nm-thick axial section through the 12-fold symmetrized flagellar motor. B. Contours through the symmetrized motor. The red contour was chosen for isosurfacing. C. Side view isosurface of the motor. D. Cutaway of the motor.

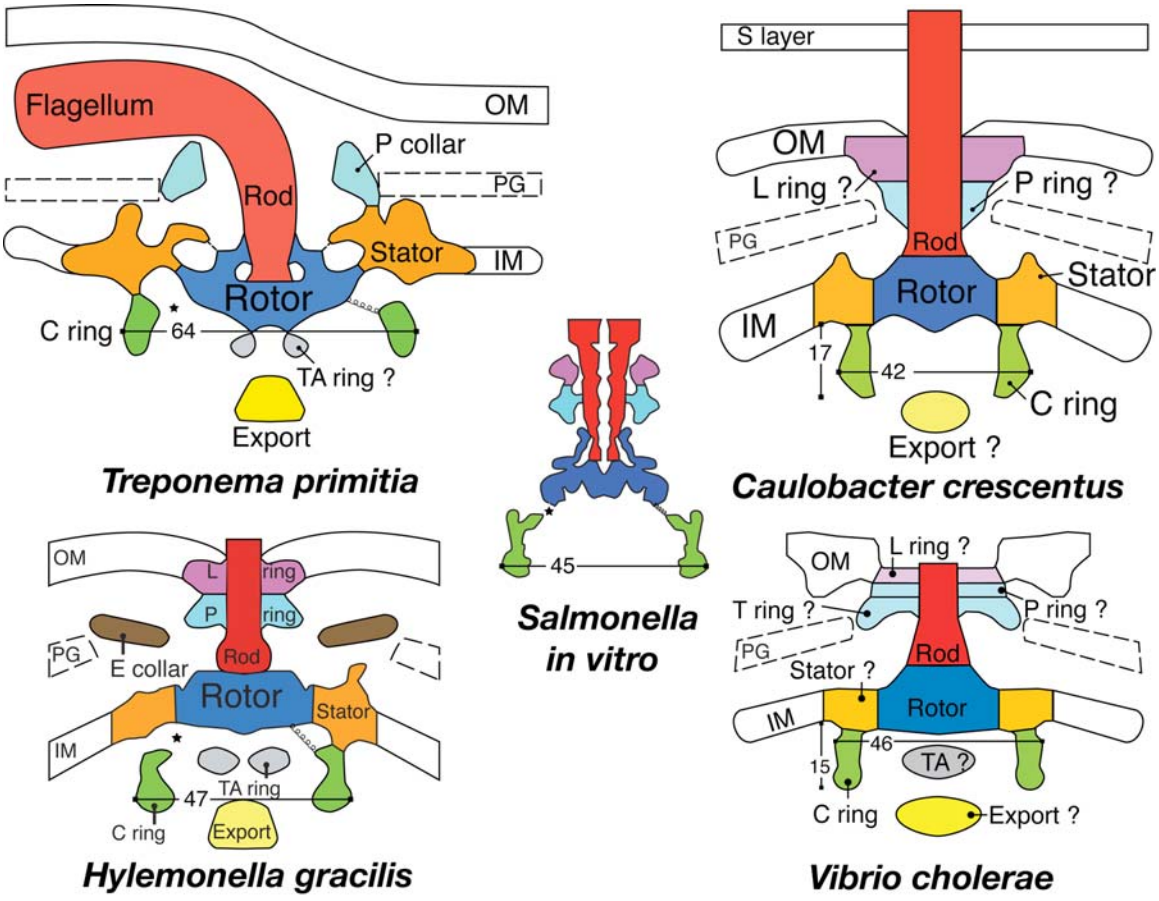

Figure VI-3. ***In situ*** **flagellar motors in comparison to** ***Salmonella in vitro***

All motors are approximately to scale. Stator studs are visible in all except *V. cholerae*. All motors have high-contrast density below their rotor that has been labeled as Export and may be a ribosome feeding monomers through the rotor. A ring labeled as a transport apparatus (TA) ring exists below *T. primitia* and *H. gracilis*, and may exist below *V. cholerae*. The L ring, P ring, and rotor borders were drawn by consulting the dimensions of negatively stained *in vitro* images of the respective motors, except for *H. gracilis*. The L ring, P ring, rotor, and stator densities are often continuous with the membranes and thus difficult to delineate.

Phylum	Name	Rod	L-ring	P-ring	P-collar	S-ring	M-ring	Insertion Disk	Rotor shape	C-ring	Insertion Pore	Stator Number	Stators	Stud width	Ref
Proteobacteria	H. gracilis Height			7											
beta	H. gracilis Diameter	12		26		24			disk	47		11-13	center 48-51	5	Murphy, unpublished
beta	Aquaspirillum serpens	10	18	21		28	31					16 max		5	Coulton, 1978
alpha	Caulobacter Height										6				Stallmeyer 1989
	Caulobacter Diam		31 or 34	25		24	31 or 28		disk	42 (Murphy)	10 (outer)		center 41 (Murphy)		Stallmeyer 1989; Murphy, unpublished
gamma	Salmonella Height	21	16 / 2	16 / 2		3.5 or 5; 2.7 best	6.5			17	5				Sosinsky 1992; Francis 1994 did Cring info; Katayama pore height; Thomas 2006 best for S, M rings
	Salmonella Diam	11.5	26	27.5		24	29		disk	45 (outer); 47-49 Thomas 2006	9 (outer)	12 max	22 or 28 int. diam.		Khan Khan 1991 did stators; Sosinsky 1992 did rotor; Francis 1994 did Cring; Katayama 1996 did pore; Thomas 2006 best for M,S rings
gamma	Ectothiorhodospira mobilis	6	25	25		20-25	20-25								Kupper 1989
gamma	E. coli	8.5, 7	22.5	22.5		22.5	22.5					12 max	20 (inner), 34 (outer)	7	Khan Dapice 1988; Kupper 1989 for rings and value "7" for Rod
gamma	Vibrio cholerae	8	23	23		11	11		disk	46 (Murphy)					Kupper 1989; Murphy, unpublished
epsilon	Campylobacter fetus		39	39		26	26								Kupper 1989
epsilon	Wolinella succinogenes	13	30	30		30	30								Kupper 1989
Firmicutes	Streptococcus	10										16 max	26 (inner), 40 (outer)	7	Khan Dapice 1988
	Bacillus firmus								mushroom or disk			12 max	33 (outer), 23 (inner)	6 to 7	Khan, Ivey 1992
	Bacillus stearothermophilus		no	no				30 to 35	disk						Abram Vatter 1966
	Bacillus brevis								disk						Abram Vatter 1966
	Bacillus circulans								mushroom or disk shaped						Abram Vatter 1966
	Bacillus pumilus								disk						Abram Vatter 1966
Spriochaetes	T. primitia Height		no	no	15	~4				12	5				
	T. primitia Diameter	12	no	no	49 (outer), 28 (inner)	24	38		mushroom	64 (outer)	17 (outer), 6.5 (inner)	16	outer 70, center 61, inner ~38	8	Murphy 2006
	Spirochaeta aurantia	12	no	no				40 to 45	mushroom or disk shaped; has a button						Bhahamsha 1988
	Leptospira interrogans		yes	yes				40 or 42 *	mushroom						Nauman 1969
	Spirochaeta halophila		no	no				40 to 45	mushroom						Paster 1980
	Spirochaeta stenostrepta		no	no				39	disk						Holt Canale-Parola 1968
	Treponema pallidum	12 to 15	no	no				supposedly 60, probably more like 40 or 50; also 30-35	mushroom or disk						Jackson 1971; 30-35 comes from Holt 1978
	Borrelia merionesi							30 to 35							Holt 1978
	Borrelia recurrentis							30 to 35							Holt 1978
	Borrelia burgdorferi		no	gene yes											blast
	Borrelia garinii		no	gene yes											blast
	Brachyspira aalborgi							33	disk						Hovind-Hougen 1982
	Brachyspira env. sample		no	no				40 *	bowl						Tasu 2003

Table VI-1. Flagellar motor measurements

Starred measurements were measured from the papers' figures and scale bars.

	Rotor	Stator	C ring	P bushing	L ring	Export	TA ring	Extra?
Salmonella	Normal	Normal 12	Normal	Ring	Yes	-	-	-
T. primitia	Wide	Wide	Wide	Collar	No	Yes	Probably	P Collar
H. gracilis	Normal ?	Normal 11-13	Normal	Ring, wider than *Sal*	Probably	Yes	Yes	E collar
V. cholerae	Normal ?	-	Normal	Ring ?	Probably	Yes	Maybe	T ring
C. crescentus	Normal ?	Narrow	Narrow	Ring ?	Probably	Maybe	-	S layer

Table VI-2. Motor components in the five structures

Appendix A

A "flip-flop" rotation stage for routine dual-axis electron cryotomography

Cristina V. Iancu[†1] , Elizabeth R. Wright[†1], Jordan Benjamin[1], William F. Tivol[1], D. Prabha Dias[1], Gavin E. Murphy[1], Robert C. Morrison[2], J. Bernard Heymann[3], and Grant J. Jensen[1*]

[1]Division of Biology, California Institute of Technology, 1200 E. California Blvd., Pasadena, CA 91125

[2]Gatan (UK), 25 Nuffield Way, Abingdon Oxon OX14 1RL UK

[3]Current address: Laboratory of Structural Biology Research, National Institute of Arthritis, Musculoskeletal and Skin Diseases, National Institutes of Health, Bethesda, Maryland 20892

[†]These authors contributed equally

[*]To whom correspondence should be addressed: jensen@caltech.edu, 626-395-8827 (phone) 626-395-5730 (fax)

Published in *Journal of Structural Biology* Volume 151, Issue 3 , September 2005, Pages 288–297

doi:10.1016/j.jsb.2005.07.004

Received 3 March 2005; revised 6 June 2005; accepted 6 July 2005. Available online 11 August 2005.

Abstract

Electron cryotomography can be used to solve the three-dimensional structures of individual large macromolecules, assemblies, and even small intact cells to medium (~ 4–8 nm) resolution in a near-native state, but restrictions in the range of accessible views are a major limitation. Here we report on the design, characterization, and demonstration of a new "flip-flop" rotation stage that allows facile and routine collection of two orthogonal tilt-series of cryosamples. Single- and dual-axis tomograms of a variety of samples are compared to illustrate qualitatively the improvement produced by inclusion of the second tilt-series. Exact quantitative expressions are derived for the volume of the remaining "missing pyramid" in reciprocal space. When orthogonal tilt-series are recorded to ±65° in each direction, as this new cryostage permits, only 11% of reciprocal space is left unmeasured. The tomograms suggest that further improvement could be realized, however, through better software to align and merge dual-axis tilt-series of cryosamples.

Keywords:

tomography, electron microscopy, cryoEM, dual-axis, cryoholder, missing wedge

Introduction

The highest resolution technique currently available for three-dimensional structural studies of unique objects is electron tomography, in which a specimen is imaged multiple times in an electron microscope (EM) while being incrementally tilted through a range of views. The method has the potential to couple the exquisite spatial resolution of modern electron microscopes, which in some cases can now be even sub-Angstrom [1, 2], with three-dimensional structure determination through a variety of reconstruction algorithms. Thus electron tomography is emerging as a powerful new technique in both materials and life science research [3-5].

There are several practical limitations for biological samples, however, including radiation damage and the typically restricted range of tilt-angles from which images can be recorded. The tilt-angle limitation arises because most EM samples are thin disks of material approximately 3 mm in diameter and ~ 30–500 nm thick, and as these samples are incrementally tilted, the depth of material the electron beam must pass through increases as one over the cosine of the tilt-angle. At high tilt-angles, most samples become prohibitively thick. In addition, the edges of standard sample holders block the electron beam at high tilt-angles. Because each projection image provides the amplitudes and phases of just one central section of the specimen's three-dimensional Fourier transform, this data collection constraint translates into a "missing wedge" of information in reciprocal space.

Early in the development of electron tomography, this missing wedge problem was significantly reduced for room temperature samples by collecting two tilt-series

about orthogonal axes, thus reducing the missing "wedge" to just a missing "pyramid" [6, 7]. This procedure was relatively straightforward because room-temperature samples could be removed from the microscope and the specimen holder, manually rotated 90°, and replaced for collection of the second tilt-series without much challenge. Despite complications due to the shrinking and warping of plastic-embedded sections during data collection, dramatic improvements in the quality of the tomograms were realized by inclusion of the second tilt-series, and dual-axis tomography became the recognized standard, best practice [8].

Concurrently, various improvements in microscope technology and sample preparation made it possible to image biological materials in a life-like, "frozen-hydrated" state. Such samples are produced by either plunge-freezing thin films [9] or cryosectioning high-pressure-frozen bulk samples [10, 11]. These developments have made it possible to study the three-dimensional structures of unique objects, including even whole cells *in their near-native states* [5], and strong efforts are now being invested to maximize resolution and interpretability.

One of the challenges has been the development of a cryostage that allowed facile collection of two perpendicular tilt-series. Because frozen-hydrated samples must always be kept at very low temperatures (standard practice is to maintain better than -160° C) to prevent ice crystallization, they cannot be simply removed from the microscope, rotated 90° and replaced unless it is done under cold nitrogen gas. This is awkward at best, and is not routinely successful because of the difficulty of fine grid manipulations under these conditions and the frequency of grid contamination. In an attempt to allow grid rotation within the microscope column, the Martinsreid group, in collaboration with Gatan,

modified a standard cryostage and then used it to collect dual-axis tilt-series of at least one frozen-hydrated sample [12], but the stage was not described and seems not to have been used in recent work from the same group [13-16]. A motor-driven tilt-rotation holder (the Gatan CT3500RT) has also been developed for standard side-entry goniometers, but no results of its use in this context are yet available. Here we report on the design, characterization, and experimental benefit of a new "flip-flop" cryorotation stage that allows routine dual-axis cryotomography in the FEI Polara transmission electron microscope, and identify new image processing challenges this type of data presents.

The flip-flop rotation stage

The "flip-flop" rotation stage was an experimental product designed and built by Gatan UK (RCM) in consultation with Caltech (GJJ) and others. The prototype was then tested and characterized experimentally at Caltech, as reported below. The stage is a derivative of the new cartridge-based, multispecimen stage system implemented to accommodate liquid-helium sample-cooling in the new Polara series of TEMs from the FEI Company. Frozen-hydrated grids are first clamped into cartridges, and then up to six cartridges at a time are loaded into a multispecimen holder. The holder is sealed, evacuated, mounted on the microscope column, and then opened to the column vacuum. Individual cartridges are picked up with an insertion tool and introduced into the column proper, where they are threaded onto a permanently-inserted specimen rod.

The flip-flop rotation stage consists of modified cartridges and a special rotation tool in the multispecimen holder. The modified cartridges house an inner, rotationally

mobile cup into which the grid is clamped (Fig. A-1A). This mobile cup has two protrusions extending out beyond the edge of the cartridge in opposite directions. The rotation tool is like a two-car garage, in that it can house cartridges in either side, but unlike a garage, it moves over and around the cartridges while they remain fixed (Fig. A-1B). When a cartridge is docked in the multispecimen holder, the rotation tool can be pushed over the cartridge (Fig. A-1C) in such a way that it catches one of the protrusions on the inner cup and causes the cup to rotate 90°. Depending on which docking position the cartridge occupies in the multispecimen holder, pushing the rotation tool causes the cup to be rotated into either the "flip" position or the "flop" position, 90° away.

Collection of a dual-axis tilt-series proceeds as follows. A cryosample is clamped into the cup of a flip-flop cartridge and loaded into the multispecimen holder. The multispecimen holder is mounted onto the microscope, the flip-flop cartridge is moved to position 5 in the multispecimen holder, and the rotation tool is pushed over the cartridge to ensure the cup begins in the "flip" position. Then the cartridge is introduced into the column, threaded onto the specimen rod, and a suitable specimen is located and imaged through one tilt-series. The cartridge is then retrieved from the column and placed into position 6 of the multispecimen holder, all the while protected by the microscope's column vacuum. The rotation tool is once again pushed over the cartridge, this time rotating the cup and grid into the "flop" position. The cartridge is again threaded onto the specimen rod, the object of interest is re-located, and the second, orthogonal tilt-series is recorded.

Technical characterization

One of the challenges for any cryostage is to minimize thermal drift. The grid must be in good, uniform, thermal contact with the cryoholder. There was concern that the rotating cup in the flip-flop cartridge would make poor contact with the rest of the cartridge and cause drift. Fortunately, no more drift was observed with the flip-flop cartridges than with regular cartridges, and both are impressively stable. A simple test grid with colloidal gold on carbon was allowed to equilibrate in the column at liquid nitrogen temperature for several hours. The drift rate was then measured at one-minute intervals for five minutes, manifesting displacements of 0.7, 0.8, 0.4, 0.3, and 0.3 nm (average 0.5 nm per minute).

Next, the actual rotation realized and the vertical displacement of the grid effected by the rotation were measured by setting eucentric height, recording a nominally untilted image, rotating the sample with the flip-flop mechanism, refinding the target region, resetting eucentric height, and recording a second nominally untilted image. In nine trials involving three different flip-flop cartridges, the rotation angle ranged from 87.0° to 88.8°, with an average of 87.7° and a standard deviation of 0.6°. The vertical displacements ranged from 0.15 to 2.65 μm, with an average of 1.07 μm and a standard deviation of 0.73 μm.

The dose needed to re-center the target region under the beam after rotation can be reduced to arbitrarily low values, including zero. The grid coordinate system can be re-oriented by imaging markers around the target region, for instance, which allows objects to be re-centered simply by moving to their new coordinates. Fine re-centering can be done by finding “focus” spots close to but on either side of the target. More

routinely, however, we have re-centered targets directly with low dose, low magnification images that deliver less than 1 electron/Å^2. All other preparative steps can be performed on peripheral areas, including resetting the eucentric height and re-centering the energy filter slit if necessary.

Qualitative comparisons of single- versus dual-axis tomograms

Using the flip-flop stage, dual-axis tomograms of a variety of representative frozen-hydrated specimens were produced including whole bacterial cells, virus-like-particles, bacterial carboxysomes, and solutions of purified proteins. The whole cell chosen was the bacterium *Mesoplasma florum*, a very small and simple cell that inhabits citrus plants. *M. florum* cells were plunge-frozen on Quantifoil grids into liquid ethane using an FEI Vitrobot. A tilt-series was collected from -66° to +62° with a 1° tilt step, and then the grid was rotated ~ 90° about the z-axis and a second tilt-series was collected from -62° to +66°. The total dose used for each tilt-series was 60 e^-/Å^2, the defocus was ~ 15 µm (first CTF zero at ~ 1/5.5 nm), and the magnification was set such that each CCD pixel represented 1.34 nm on the specimen. All images here and below were energy-filtered (slit width of 20 eV) and recorded on a 300 kV FEG "G2 Polara" TEM with the sample cooled by liquid nitrogen to ~ 82 K.

Three-dimensional tomograms of the first and second tilt-series were calculated and combined using the IMOD package [7], and then the individual and combined tomograms were denoised by 40 rounds of nonlinear anisotropic diffusion [17]. Fig. A-2 shows slices through the centers of three tomograms of a *M. florum* cell: one from each of the two independent tilt-series and one from their combination. All the XY slices (left

column) are comparably well-defined, and many individual large protein complexes are resolved within the cell. Nevertheless, while the tomogram from the first tilt-series (top row) shows some detail in the XZ slice (albeit smeared in the Z direction), the YZ slice is quite poor. The tomogram from the second tilt-series (middle row) is the opposite, showing some detail in the YZ but not the XZ slice. Only in the dual-axis tomogram (bottom row) are particles resolved in all three directions. The residual missing pyramid of data is still evident, though, in the membrane's lack of closure over the top and bottom surfaces of the cell.

Next, the impact of including a second tilt-series was observed on a purified, HIV-1 virus-like particle (VLP). HIV-1 is an enveloped retrovirus whose outer layer consists of a lipid bilayer and a matrix protein shell. In these VLPs, the Env protein was removed to eliminate infectivity, so no surface "spikes" are seen. Inside the lipid/matrix layer there is a typically conical capsid shell [18]. An HIV-1 VLP was plunge-frozen, imaged through orthogonal tilt-series, reconstructed, and denoised as described above for *M. florum*, except that the tilt-series were from -57° to +60° and -60° to +60° with a 3° tilt step, the defocus was ~ 16 µm (first CTF zero at ~ 1/5.6 nm), the image pixel size was 1.34 nm, the total dose was 240 $e^-/Å^2$, and only 20 rounds of denoising were performed (Fig. A-3). Although still not complete, the dual-axis tomogram resolved significantly more of the viral layers' morphologies than either single-axis tomogram. This was made particularly obvious in the three-dimensional renderings of the viral envelope isosurface. The improved but still imperfect point-spread-function was also evidenced by the gold fiducial, which appeared nicely round in the XY plane, but still elongated in the Z direction.

In the two previous cases (MF and HIV-1), comparisons were made between single-axis tomograms and their dual-axis combinations. While this eliminated structural differences between the compared objects, the dual-axis tomograms unfairly profited from twice the dose. Two additional samples were therefore tested where single- and dual-axis tomograms could be calculated from separate but very similar objects, using the same *total* dose. The first such sample was purified carboxysomes from the prokaryote *Synechococcus species*. Carboxysomes are ~ 100 nm microcompartments consisting of a proteinaceous shell surrounding many tens of copies of the enzyme ribulose1,5-bisphosphate carboxylase/oxygenase (RuBisCO), as well as other, smaller enzymes [19]. Carboxysomes were plunge-frozen and imaged through either a single tilt-series or through two orthogonal tilt-series, in every case to ±64°. The dose (total) was 120 $e^-/Å^2$, the tilt step was 2°, the defocus was ~ 10 µm (first CTF zero at ~ 1/4.5 nm), the image pixel size was 6.7 Å, and 200 rounds of denoising were performed. The protein shell and many individual RuBisCO molecules can be resolved in the tomograms (Fig. A-4). Again the resolution of the dual-axis tomogram is clearly more isotropic, but still not as good in the Z direction as in the X or Y directions.

Finally, several different purified protein complexes were imaged, including the molluscan hemocyanin from *Megathura crenulata*. This hemocyanin is an ~ 8 MDa complex that forms a double-layered, hollow barrel approximately 30 nm in diameter and 35 nm in length. Hemocyanin was plunge-frozen and imaged through single- (-66° to 63°) and dual-axis (-66° to 63° first axis, ±63° second) tilt-series with an angular step size of 3°, a defocus of 8 µm (first CTF zero at ~ 1/4.0 nm), and a pixel size of 6.7 Å. Single- and dual-axis tomograms were recorded with the same total dose (110 $e^-/Å^2$) from

different holes in the same square of a single grid with as similar ice thicknesses and other characteristics as possible. Three-dimensional renderings of particles that froze with their long axes in the plane of the sample and either parallel or perpendicular to the tilt-axis, and with their long axis perpendicular to the sample ("vertical") are shown (Fig. A-5) after 20 rounds of denoising and alignment to a reference [20] using the BSOFT software package [21] The particles were not symmetrized before rendering. While the dual-axis tomograms are perhaps just slightly better, the improvement was more modest than expected. As discussed below, this is probably due to non-optimal merging of the two tilt-series, which was most challenging in this case of isolated protein complexes.

Novel data processing challenges

The IMOD software package [7] was used to produce all these tomograms. The procedure begins by calculating two independent, real-space tomograms from the two tilt-series, and then the second tomogram is transformed into approximate alignment with the first using the coordinates of corresponding gold fiducials. The second tomogram is then sampled with an array of subvolumes ("patches"), and each patch is cross-correlated with a corresponding patch from the first. A map of the resulting displacement vectors is fit to a smooth function, and a new, "dewarped" version of the second tomogram is calculated. The dewarped second and the first tomograms are Fourier transformed and averaged in reciprocal space, and then a final, dual-axis tomogram is produced by inverse transformation. While these algorithms have been used and refined extensively to merge tilt-series of plastic sections, the data from cryosamples can be different in important ways: (1) the gold beads are typically distributed throughout the sample rather than just

on the top and bottom surfaces; (2) no shrinkage or distortion during data collection is expected; (3) images are more noisy due to the stringent dose limitations; and (4) contrasty objects can be more sparse, as, for instance, the isolated hemocyanin molecules were against the feature-less background of vitreous ice.

These differences introduced novel image processing problems. First, while no evidence for shrinking or warping was seen, a small fraction of the gold fiducials used to align the two tilt-series moved by up to several nm during acquisition of the data. Because no reproducible pattern was recognized, this mismatch is likely caused by the fiducials diffusing randomly within the vitreous ice. Thus their movements were sometimes significant, but not correlated with movements of neighboring objects of interest (unlike fiducials on the surface of a shrinking plastic section).

Next, the strategy of mapping local distortions between the first and second tomograms seemed non-ideal in this context, especially for the isolated protein complexes. In the case of hemocyanin, for instance, the best results were obtained when exceedingly large patches and high "warping residual limits" were used. This is probably because small patches sometimes contained only vitreous ice, and were therefore nearly featureless, and yielded misleading distortion vectors. To solve this problem, IMOD already allows users to identify specific regions to be included in the dewarping procedure, and discard anomalous vectors, but superior results would likely be obtained by using each reconstructed macromolecular complex as a "patch." An iterative refinement procedure in which all the images from both tilt-series were re-aligned to projections of the reconstructed object of interest (as in standard "single particle analysis," see [22], might be best of all. In principle, the structure of cryosamples should

not be changing during data collection, and thus no dewarping at all should be necessary. Slight changes in the electron optics, non-idealities of the tilt-axis, and distortions caused by the energy filter are still probably introducing slight distortions which can and should be corrected.

Finally, it was observed that in the three-dimensional power spectra of the final tomograms, the average intensity in regions where data was combined from both tilt-series was lower than the average intensity in regions covered by just one or the other (Fig. A-6a). The algorithm used in IMOD to merge tilt-series was a simple average: In regions of reciprocal space where there was data from both or neither tilt-series, the two values were simply averaged vectorially; whereas in regions where there was data from just one tilt-series, that single value was used. While this seems entirely reasonable, the reduced amplitudes in doubly-measured regions can be explained simply by the fact that the average length of two vectors is always larger than the length of their *vector* average, except in the rare case that their directions (phases) are identical. While this difference may not be large for well-aligned data with a high signal-to-noise ratio, it was apparent in these cryotomograms. D. Mastronarde therefore introduced an IMOD option to simply attenuate the amplitudes in the singly-measured regions to match those in the doubly-measured regions within shells of reciprocal space (Fig. A-6b). Whether this is the optimal procedure has yet to be explored.

Size of the missing pyramid in single- versus dual-axis data collection

The potential benefit of dual-axis tomography can be assessed quantitatively by calculating the percentage of reciprocal space covered by single- and dual-axis tilt-series.

While isolated results of similar calculations already appear in the tomography literature, the formulas and their derivations do not to our knowledge, and because they involve principles of spherical trigonometry unfamiliar to most investigators in this field, they are presented here. In spherical trigonometry, lengths and areas are quantified in degrees and "spherical" degrees, respectively, and by "spherical polygon" is meant a region on the surface of a sphere whose borders are defined by planes passing through the sphere's origin. The area of a spherical polygon in spherical degrees is equal to its angular excess; i.e., the amount by which the sum of its angles exceeds that of an analogous polygon on a plane. For example, on a globe the spherical triangle formed by a segment of the equator and two meridians of longitude has an area equal to the angle between the meridians, since the angles between each meridian and the equator is 90°, and account by themselves for the sum of the three angles of a planar triangle.

Making the assumption that the flip-flop holder yields two tilt-series that are indeed orthogonal, but allowing different maximum tilt-angles in both the positive and negative direction for both tilt-axes, one can calculate the size of the missing pyramid using Fig. A-7. The view is down the direction of the electron beam, or Z axis, and the four large arcs (two splitting away from and rejoining the X axis and two splitting away from and rejoining the Y axis) represent the limits of the two tilt-series. Thus the first tilt-series (along X) is from α_{min} to α_{max}, and the second tilt-series (along Y) is from β_{min} to β_{max}. These arcs should be thought of as lying on the surface of a sphere in reciprocal space, while the X and Y axes lie within an "equatorial" plane below, such that they do not intersect with the arcs except at the endpoints. Since the totality of information out to any specified resolution is a sphere, and since the solid angle of the missing pyramid is

the same regardless of the sphere's radius, the fraction of missing information is the ratio of the area of the spherical quadrilateral bounded by the planes of maximum tilts (shaded region) to the area of the full hemisphere, or 360 spherical degrees. The missing area is equal to its angular excess, or $(180° - \theta^{++}) + (180° - \theta^{-+}) + (180° - \theta^{--}) + (180° - \theta^{+-}) - 360°$. Napier's rules for right spherical triangles state that the cosine of one of the non-right angles is equal to the sine of the other non-right angle times the cosine of the opposite side length. Thus $\cos(\theta^{++}) = \sin(90° - \alpha_{max})\cos(\beta_{max})$, or $\cos(\alpha_{max})\cos(\beta_{max})$. Similarly, $\cos(\theta^{-+}) = \cos(\alpha_{min})\cos(\beta_{max})$, $\cos(\theta^{--}) = \cos(\alpha_{min})\cos(\beta_{min})$, and $\cos(\theta^{+-}) = \cos(\alpha_{max})\cos(\beta_{min})$. Given α_{min}, α_{max}, β_{min}, and β_{max}, the percentage of missing information can be found by calculating the angles θ, and then the angular excess of the missing region. Note that the formulas are symmetric with respect to which angles are called α and β, which directions are called "max" and "min," and give correct results at limiting values, including the case of single-axis tilting.

Several key results are listed in Table A-1. In order to reduce the missing information to just 10% (an arbitrary example target) with single-axis tilting, ±81° must be obtained. This is of course fundamentally problematic, because thin films are 6.4 times thicker parallel to the electron beam at 81° than they are untilted. For dual-axis tilting, reducing the missing pyramid to 10% requires reaching just 67°, where the sample is only 2.6 times thicker. The flip-flop cartridges allow imaging to ±65°, so that all but 11% of the data can be gathered for a thin sample.

Discussion

From this work we conclude that: (1) the new flip-flop holder succeeds in making the collection of dual-axis tilt-series of cryosamples convenient and routine, (2) including the second tilt-series does result in more isotropic resolution as expected, but (3) further gains should be realizable through better software to merge the data. The flip-flop holder has been used to collect more than a hundred dual-axis tilt-series of various samples now, of which only a few examples were shown here. These demonstrated that inclusion of the second tilt-series clarified the morphology of membranes, protein shells, and individual protein complexes. We have since observed other cases where dual-axis tilting has proven critical—including one dramatic case where a key bacterial cytoskeletal filament was essentially invisible in the tomogram of the first tilt-series, but was clearly resolved in the second. Except for the 90° rotation, the two tilt-series were otherwise identical in defocus, etc., and of course radiation damage does not explain the difference, since the filament was seen in the second tilt-series but not the first. Instead, this filament exemplified how long, tubular features that lie perpendicular to the tilt-axis are nearly invisible to single-axis tomography.

Despite these encouraging improvements, the results also suggest that better methods for alignment and merging are needed. This study is the first attempt to our knowledge to merge dual-axis tilt-series of isolated macromolecules suspended in vitreous ice. Considering the range of views used in the hemocyanin tomograms, the dual-axis tomograms theoretically profited from an additional 15% coverage of reciprocal space (72% for the single-axis tomograms, 87% for the dual). The gains experimentally realized in this particular case (as seen in Fig. A-5) were only modest. We attribute this to

non-optimal alignment and merging, which should be improved by more customized software.

Finally, the cartridge-based specimen holder system was originally designed to allow samples to be cooled with liquid helium rather than liquid nitrogen, in hopes that radiation damage could be further slowed or restrained. One of the potential disadvantages of the flip-flop stage design was that the sample had to be warmed to approximately -190° C between tilt-series for rotation because the multispecimen holder is only nitrogen-cooled. Thus the potential advantages of helium-cooling would be lost mid-way. Disappointingly, this is no longer a concern. Only disadvantages have been observed for liquid helium-cooling in cryotomography, and we now routinely use only liquid nitrogen. As part of the present investigations, however, the effects of warming helium-cooled samples to -190° C for rotation in the multispecimen holder were extensively explored. While the results will be reported in full alongside related experiments evidencing phase transitions in vitreous ice (manuscript in preparation), we note here that the warming associated with rotation did indeed relax some radiation-induced strains. The relaxation was a net advantage, however, if anything, as it tended to restore lost contrast and delay the appearance of small bubbles.

Acknowledgements

We thank D. Mastronarde for assistance with IMOD, H.J. Ding and B. Wen for image processing, A. Martino for providing purified carboxysomes, W. Sundquist for purified HIV-1 virus-like particles, and S. Tivol for reading the manuscript. This work was supported in part by NIH Grant PO1 GM66521 to GJJ, DOE grant DE-FG02-04ER63785

to GJJ, the Beckman Institute at Caltech, and gifts to Caltech from the Ralph M. Parsons Foundation, the Agouron Institute, and the Gordon and Betty Moore Foundation.

References

1. Batson, P.E., N. Dellby, and O.L. Krivanek, *Sub-angstrom resolution using aberration corrected electron optics.* Nature, 2002. **418**(6898): p. 617-20.
2. Hosokawa, F., et al., *A spherical aberration-corrected 200 kV TEM.* J. Electron Microsc., 2003. **52**(1): p. 3-10.
3. Ziese, U., K.P. de Jong, and A.J. Koster, *Electron tomography: a tool for 3D structural probing of heterogeneous catalysts at the nanometer scale.* Applied Catalysis A:General, 2004. **260**(1): p. 71-74.
4. Subramaniam, S. and J.L.S. Milne, *Three-dimensional electron microscopy at molecular resolution.* Annu. Rev. Biophys. Biomol. Struct., 2004. **33**: p. 141-155.
5. Baumeister, W., *Mapping molecular landscapes inside cells.* Biol. Chem., 2004. **385**(10): p. 865-72.
6. Penczek, P., et al., *Double-Tilt Electron Tomography.* Ultramicroscopy, 1995. **60**(3): p. 393-410.
7. Mastronarde, D.N., *Dual-axis tomography: an approach with alignment methods that preserve resolution.* J. Struct. Biol., 1997. **120**(3): p. 343-52.
8. McEwen, B.F. and M. Marko, *The emergence of electron tomography as an important tool for investigating cellular ultrastructure.* J. Histochem. Cytochem., 2001. **49**(5): p. 553-64.

9. Dubochet, J., et al., *Cryo-electron microscopy of vitrified specimens.* Q. Rev. Biophys., 1988. **21**(2): p. 129-228.

10. Hsieh, C.E., et al., *Electron tomographic analysis of frozen-hydrated tissue sections.* J. Struct. Biol., 2002. **138**(1-2): p. 63-73.

11. Al-Amoudi, A., et al., *Cryo-electron microscopy of vitreous sections.* EMBO J., 2004. **23**(18): p. 3583-8.

12. Nickell, S., et al., *Pyrodictium cannulae enter the periplasmic space but do not enter the cytoplasm, as revealed by cryo-electron tomography.* J. Struct. Biol., 2003. **141**(1): p. 34-42.

13. Beck, M., et al., *Nuclear pore complex structure and dynamics revealed by cryoelectron tomography.* Science, 2004. **306**(5700): p. 1387-90.

14. Grünewald, K., et al., *Three-dimensional structure of herpes simplex virus from cryo-electron tomography.* Science, 2003. **302**(5649): p. 1396-8.

15. Cyrklaff, M., et al., *Cryo-electron tomography of vaccinia virus.* Proc. Natl. Acad. Sci. U.S.A., 2005. **102**(8): p. 2772-7.

16. Kürner, J., A.S. Frangakis, and W. Baumeister, *Cryo-electron tomography reveals the cytoskeletal structure of Spiroplasma melliferum.* Science, 2005. **307**(5708): p. 436-8.

17. Frangakis, A.S. and R. Hegerl, *Noise reduction in electron tomographic reconstructions using nonlinear anisotropic diffusion.* J. Struct. Biol., 2001. **135**(3): p. 239-50.

18. Benjamin, J., et al., *Three-dimensional structure of HIV-1 virus-like particles by electron cryotomography.* J. Mol. Biol., 2005. **346**(2): p. 577-588.

19. Cannon, G.C., et al., *Microcompartments in prokaryotes: carboxysomes and related polyhedra.* Appl. Environ. Microbiol., 2001. **67**(12): p. 5351-61.

20. Mouche, F., et al., *Automated three-dimensional reconstruction of keyhole limpet hemocyanin type 1*. J. Struct. Biol., 2003. **144**(3): p. 301-12.

21. Heymann, J.B., *Bsoft: image and molecular processing in electron microscopy.* J. Struct. Biol., 2001. **133**(2-3): p. 156-69.

22. Frank, J., *Single-particle imaging of macromolecules by cryo-electron microscopy.* Annu. Rev. Biophys. Biomol. Struct., 2002. **31**: p. 303-19.

Figures and Table

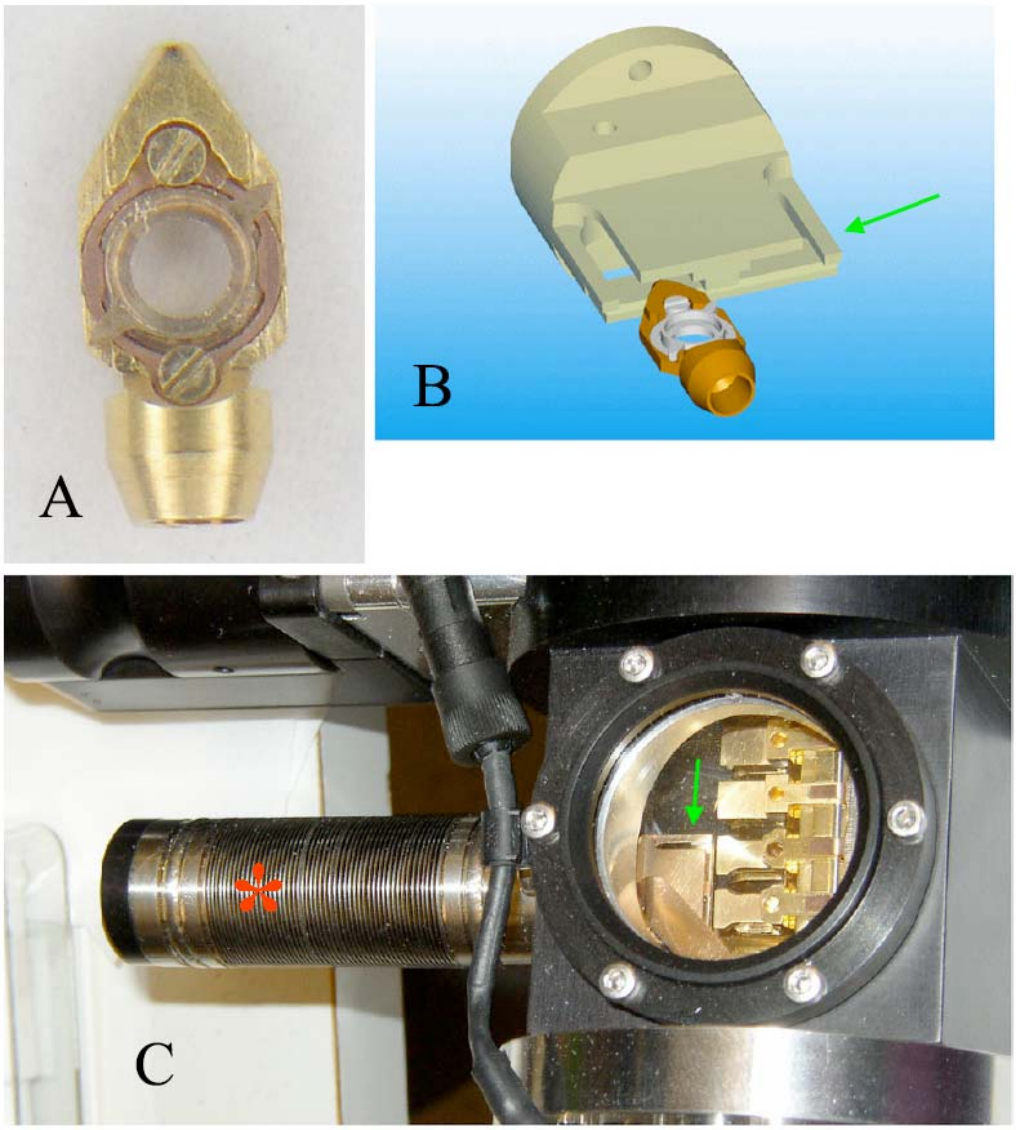

Figure A-1. Flip-flop rotation stage.

Panel A: Photograph of a flip-flop cartridge. The lower (non-pointed) end houses threads used to mount the cartridge to the end of the specimen rod, which resides permanently in the microscope. The inner cup can be rotated, and has two protrusions seen here at "2" and "8 o'clock." For scale, the cup circumscribes grids 3 mm across. Panel B: A drawing

of a flip-flop cartridge positioned in front of the rotation tool (courtesy FEI Company and Gatan UK). The rotation tool is like a two-car garage in that it could house the cartridge in either of two positions, here seen as “left” and “right” sides. If the rotation tool were pushed over the cartridge as aligned in the drawing, its front edge would catch the right cup protrusion and cause the cup to rotate 90°. Panel C: a photograph of the part of the multispecimen holder that houses the rotation tool. Through the circular glass window on top, cartridge docking positions 3 (top) through 6 (bottom) are visible on the right, and the front edge of the rotation tool is visible on the left (green arrows in panels B and C point to rotation tool in the same orientation). Pushing the bellowed piston (red asterisk) seen on the left side of the photograph moves the tool over and around cartridge docking positions 5 and 6, rotating any cartridges that may be present into either the flip or flop orientation, depending on their position.

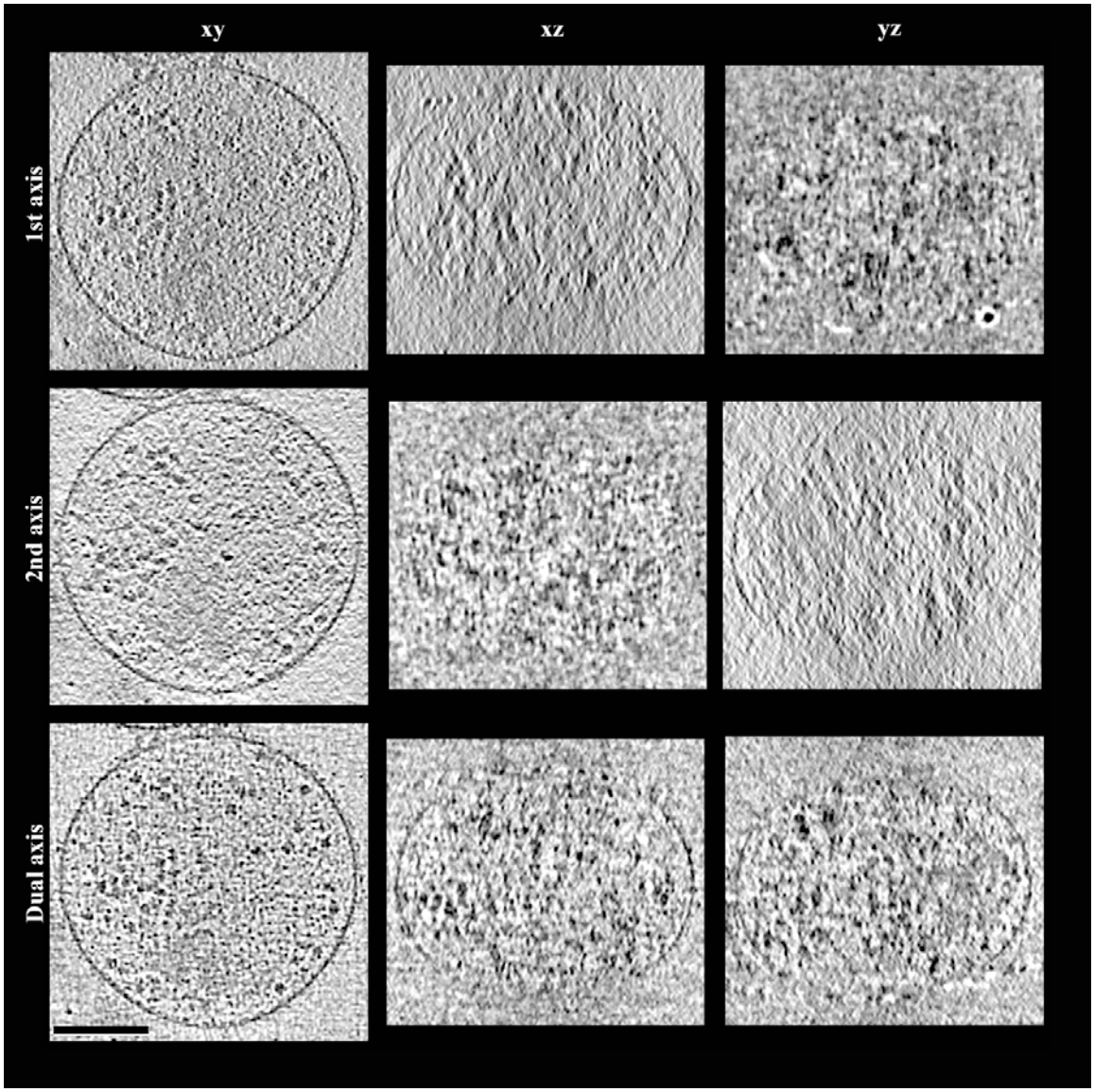

Figure A-2. Single- and dual-axis tomograms of an intact cell.

On the top, middle, and bottom rows are shown single slices of the first single-axis tomogram, the second single-axis tomogram, and the combined dual-axis tomogram, respectively, of an intact *M. florum* cell. The left, middle, and right columns show XY, XZ, and YZ slices, respectively. While individual macromolecular complexes are visible in the XY slices of all three tomograms, only in the dual-axis tomogram are the densities resolved (punctate) in all three directions. The extended but still not complete definition

of the membrane clearly reveals the improved but still anisotropic point-spread-function. (Scale bar is 150 nm.)

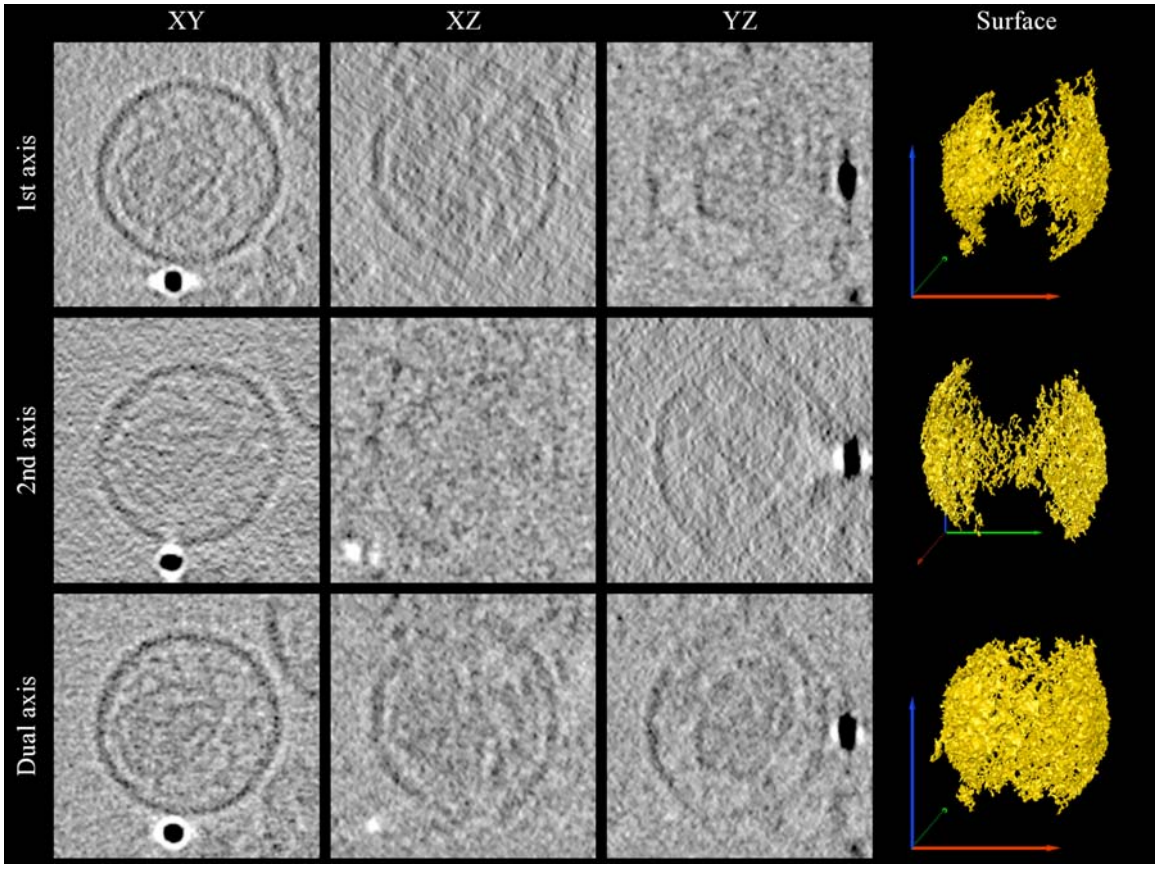

Figure A-3. Single- and dual-axis tomograms of an HIV-1 virus-like particle.

XY, XZ, and YZ slices from the first single-axis tomogram (top), the second single-axis tomogram (middle), and the combined dual-axis tomogram (bottom) of an HIV-1 virus-like particle are shown as in Fig. A-2. The outer bilayer/matrix layer and the capsid are visible. A single gold fiducial also appears at the bottom of the XY slices and on the right side of the YZ slices, which shows well the asymmetry of the point-spread-function in the single-axis tomograms. Dual-axis tilting makes this point-spread-function round in the XY slice, but it is still elongated in the Z direction. Three-dimensional renditions of the continuous envelope density are shown on the far right (note that the view in the second row has been rotated 90° relative to the others to show its missing wedge). These isosurfaces were defined by the "Magic Wand" tool in the Amira software package,

which marks voxels that are both connected to an initial seed voxel and have densities higher than a user-specific value. (For scale, the diameters of the gold fiducial and virus-like particle are 10 and ~ 125 nm, respectively.)

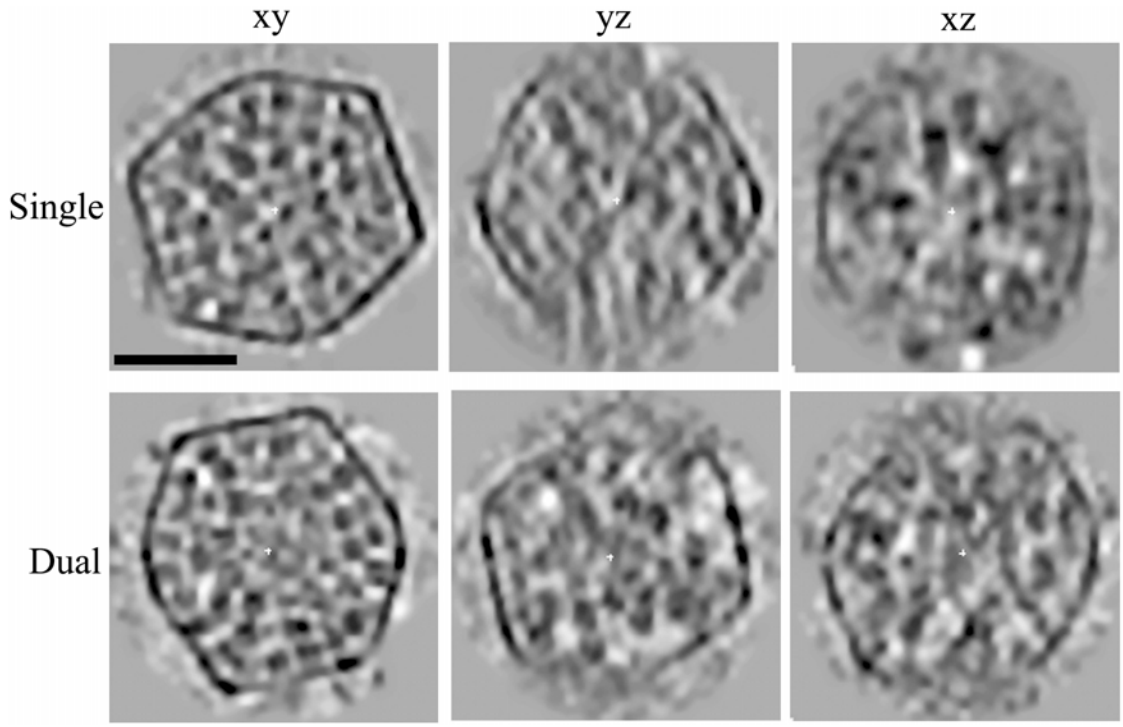

Figure A-4. Single- and dual-axis tomograms of prokaryotic carboxysomes.

XY, YZ, and XZ slices through the tomograms of two different carboxysomes are shown. The outer protein shell can be seen enclosing many tens of RuBisCO enzymes inside. Each tomogram used the same total dose, so the improvements in the dual-axis tomogram are due to data collection geometry rather than any increase in dose. (Scale bar is 50 nm.)

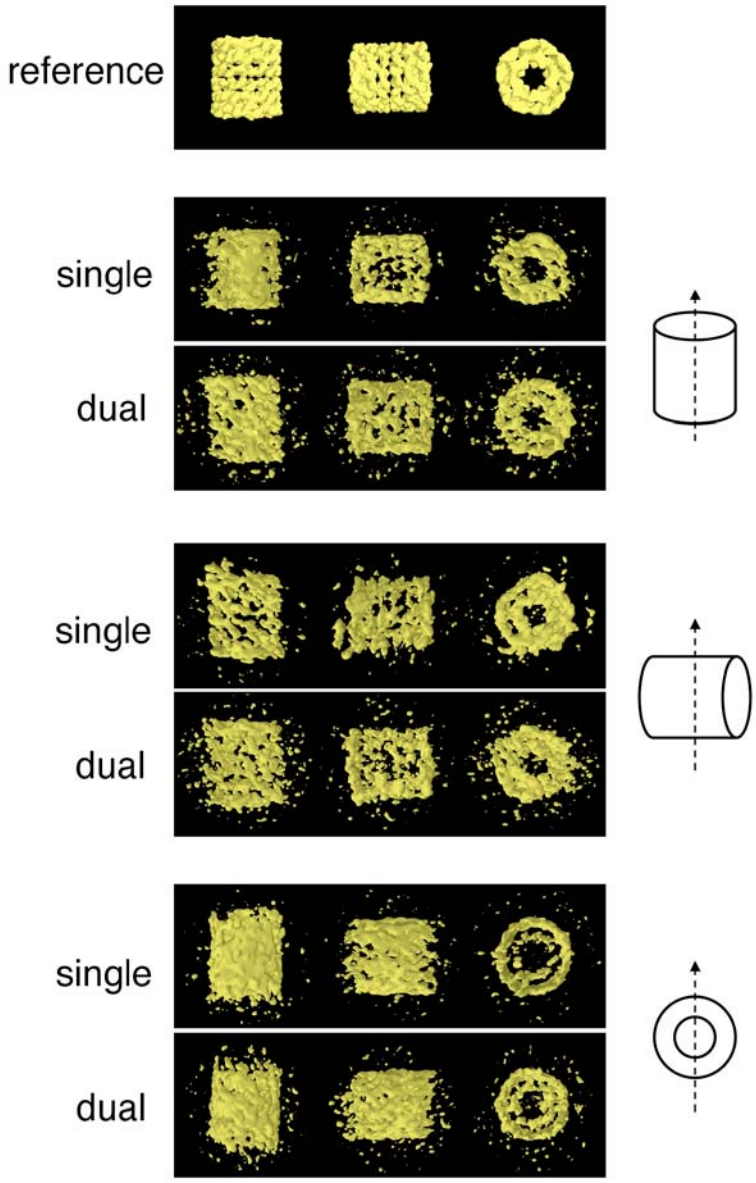

Figure A-**5. Single- and dual-axis tomograms of individual protein complexes.** Surface renderings of seven independent reconstructions of the barrel-shaped hemocyanin protein complex are shown. Each row presents one reconstruction, seen from three different points of view. The top row displays the 12 Å "single-particle" reconstruction obtained by averaging hundreds of projection images [20], and is shown for comparison and orientation. The even- and odd-numbered rows show single- and dual-axis tomograms, respectively, generated with the same total dose. The particular

particles shown were chosen to control for and reveal how orientation in the ice, as depicted on the right, influenced the results. In the schematic, the dotted line represents the tilt axis (or the first tilt axis in the case of the dual-tilt tomograms), and the plane of the schematic represents the plane of the grid. Simple isosurfaces are shown, contoured at 2.5 standard deviations above the mean. (For scale, hemocyanin is ~ 35 nm in length.)

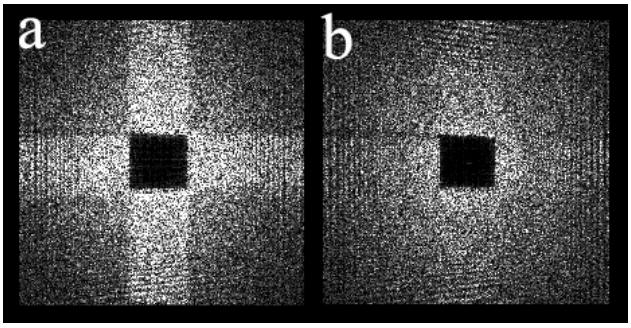

Figure A-6. Missing pyramid and intensity scaling.

Sections from the three-dimensional power spectrum of a reconstructed *M. florum* cell are shown. Both are the fortieth XY section above the central "Z = 0" section, so that the missing pyramid is visible as a square in the middle. In (a), the overweighted intensities in the singly-measured regions of reciprocal space appear as a bright cross. The same section is shown in (b) after application of the new intensity scaling function.

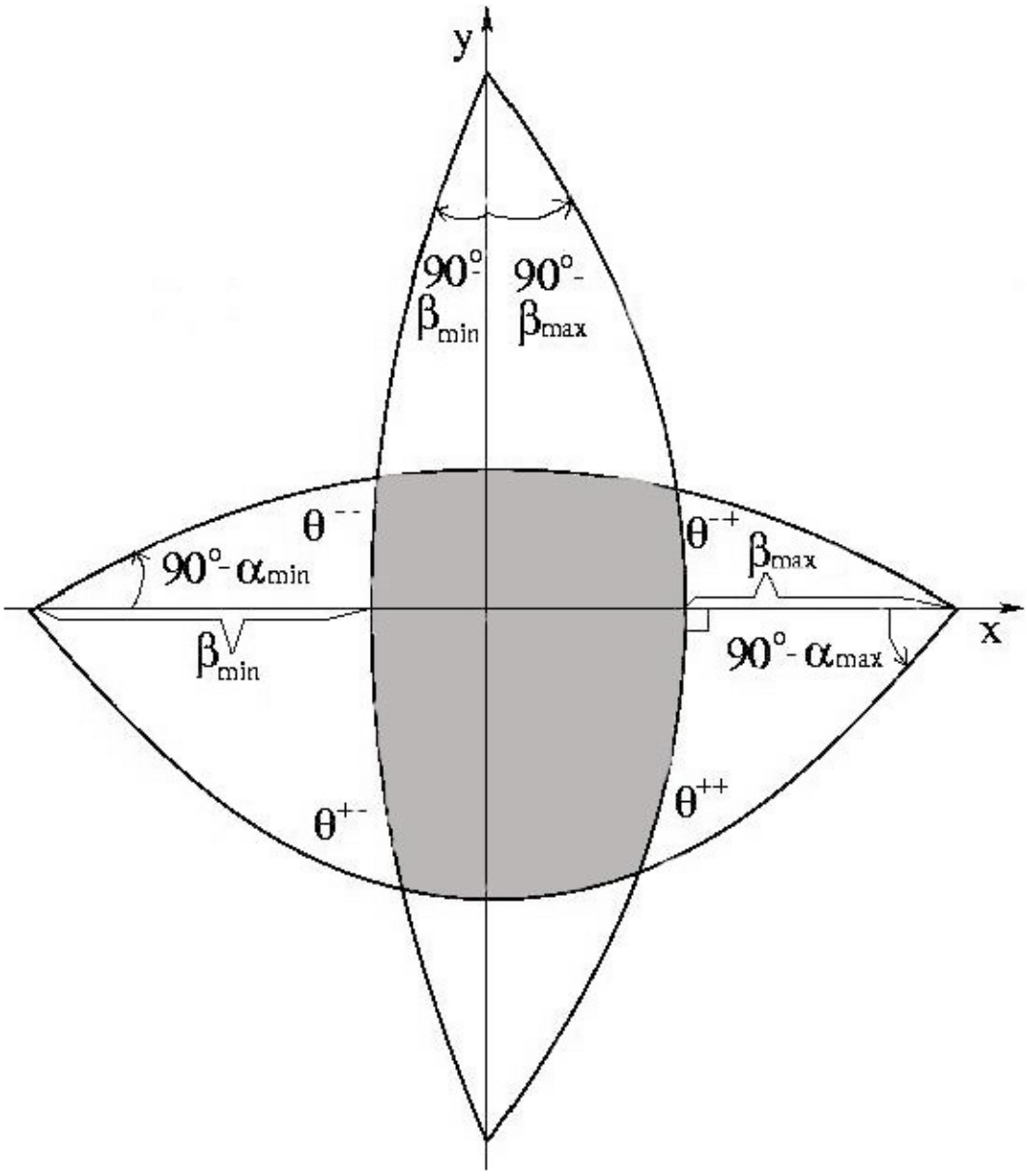

Figure A-7. Diagram used to find the area of the "missing pyramid."

The four large arcs delineate the angular limits of data collection in the two orthogonal tilt-series (α_{min}, α_{max}, β_{min}, and β_{max}) on the surface of a sphere in reciprocal space. The area of the missing pyramid is equal to the "angular excess" of the shaded spherical quadrilateral, and is found as described in the text.

Tilt range	Thickness increase at angular extreme	Percent of reciprocal space unmeasured	
		Single-axis data collection	Dual-axis data collection
±60°	2.0_	33%	16%
±67°	2.6_	26%	10%
±70°	2.9_	22%	7.5%
±81°	6.4_	10%	1.6%

Table A-1. Percent coverage of reciprocal space in single- and dual-axis tomography.

Appendix B

Electron cryotomography sample preparation using the Vitrobot.

*Cristina V. Iancu, William F. Tivol, Jordan B. Schooler, D. Prabha Dias, Gregory P. Henderson, Gavin E. Murphy, Elizabeth R. Wright, Zhuo Li, Zhiheng Yu, Ariane Briegel, Lu Gan, Yongning He, and Grant J. Jensen**

Division of Biology, California Institute of Technology, 1200 E. California Blvd., Pasadena, CA 91125

*To whom correspondence should be addressed: Jensen@caltech.edu, 626-395-8827 (phone) 626-395-5730 (fax)

Published in Nature Protocols 2007; 1: 2813-2819

doi:10.1038/nprot.2006.432

ABSTRACT

Electron cryotomography (ECT) is the highest-resolution structural technique currently available that can be applied to unique objects such as flexible large protein complexes, irregular viruses, organelles, and small cells. Specimens are preserved in a near-native, "frozen-hydrated" state by vitrification. The thickness of the vitreous ice must be optimized for each specimen, and gold fiducials are typically added to facilitate image alignment. Here, we describe in detail our protocols for ECT sample preparation including (1) introduction of fiducial markers into the sample and (2) sample vitrification. Because we almost exclusively use an automated, climate-controlled plunge freezing device (the FEI Vitrobot) to vitrify our samples, we discuss its operation and parameters in detail. A session in which 8 grids are prepared takes 1.5 to 2 hours.

INTRODUCTION

Electron cryotomography (ECT) is an increasingly important technique for determining the structure of unique objects such as flexible large protein complexes, irregular viruses, organelles or small cells (Lucic *et al.*, 2005; Nickell *et al.*, 2006). Specimens preserved in a near-native, "frozen-hydrated" state are tilted incrementally around one or two (orthogonal) axes while being imaged in a transmission electron microscope (TEM). The resulting "tilt-series" of projections are aligned with respect to each other usually using fiducial markers (electron-dense reference objects such as colloidal gold) embedded with the sample in the ice. The aligned images are then computationally merged into a three-dimensional (3-D) reconstruction.

As in all types of microscopy, sample preparation is vital. Three factors are key: the sample itself must be maintained in as near a native state as possible, the vitreous ice must be thin and uniform, and the fiducial markers should be abundant and evenly distributed. To minimize artifacts and perturbations, samples can be plunge-frozen in complete growth media or physiologic buffers. Because the surrounding media or buffer produces background scattering that degrades the image, however, it is generally advantageous to thin the ice as much as possible, as long as the structure of the sample is not distorted. In extremely thin ice, even individual strands of duplex DNA have been seen in electron cryomicrographs (Adrian *et al.*, 1990). Thicker ice seems to have improved mechanical stability, however, in other contexts (Li *et al.*, 2002), so ice thickness must be optimized for every situation. The fiducial markers need to be abundant and distributed uniformly to ensure accurate image alignment.

ECT sample preparation typically comprises two major steps: (1) introduction of gold fiducial markers and (2) sample vitrification. In order to increase the chances of having uniformly distributed fiducials in any particular area, we apply colloidal gold to both the grids and the sample solutions before they are united. Aqueous solutions are vitrified by cooling them so quickly (~ 10^7 K/s) that individual water molecules do not have opportunity to move around and form an extended, hydrogen bond-mediated crystal lattice with long-range order. Rather, they become "trapped" in an amorphous state resembling liquid water (Angell, 2004). Using a strategy pioneered by Jacques Dubochet and his colleagues (Adrian *et al.*, 1984; Dubochet and McDowall, 1981; Lepault *et al.*, 1983), this can be accomplished in four steps: (1) applying the sample onto an electron microscopy grid; (2) blotting excess fluid to produce a thin film; (3) plunge-freezing the grid into liquid ethane or propane; and (4) transferring the grid to a storage box immersed in liquid nitrogen.

Today many labs have custom-made, "in-house" plunge-freezing devices where the sample is blotted manually (by hand with a filter paper) and the plunger is accelerated by gravity or air pressure. We are not aware of any that give robustly reproducible results, however, even for expert practitioners, because they depend on user dexterity, timing, and the local climate conditions. More recently, sophisticated commercial devices have become available that allow precise control of nearly all the parameters including the temperature and humidity of the blotting chamber; the frequency, duration, and pressure used for blotting; and the plunge velocity. In our lab we use the FEI Company's automatic plunge-freezer, which they named the "Vitrobot" (Frederik and Hubert, 2005). In addition to the aforementioned parameters, which are self-explanatory, a "blot offset"

parameter controls the position of the grid between the blotting pads, which controls in part the pressure exerted by the filter paper on the grid. "Drain time" is a surprisingly useful parameter that specifies an optional delay between blotting and plunging when the sample simply equilibrates in the blotting chamber ("drain time" is actually a misnomer, since no fluid is actually draining). In general, the blotting chamber is humidified to 100% to minimize potential imbalances in evaporation and condensation that might develop during the drain time, and the temperature is generally set to the preferred temperature of the sample (can be the incubation temperature of a cell culture, for instance).

Using the Vitrobot, we have successfully prepared a variety of samples for ECT including large protein complexes, viruses, organelles and narrow whole cells (Benjamin *et al.*, 2005; Briegel *et al.*, 2006; Henderson and Jensen, 2006; Iancu *et al.*, 2005; Iancu *et al.*, 2006; Komeili *et al.*, 2006; Murphy and Jensen, 2005; Murphy *et al.*, 2006; Wright *et al.*, 2006). The protocol and discussion presented here is the result of our laboratory members' collective experience with several different Vitrobots and in-house plunge freezing devices and will describe details of both the introduction of fiducial markers and the specific Vitrobot conditions used for different samples. (Additional information on the use and applications of the Vitrobot, including a video demonstration of its operation, can be found on the company website at www.vitrobot.com.)

MATERIALS

REAGENTS

- sample
- 10 nm (or 5 nm) colloidal gold (SPI Supplies, West Chester, PA, USA, www.2spi.com or Sigma, St Louis, MO, USA, www.sigma.com)
- liquid nitrogen
- ethane
- bovine serum albumin (BSA).

CAUTION: Liquid nitrogen and ethane are cryogens and should be handled with care and appropriate personal protective equipment (goggles, gloves, lab coat). Additionally, ethane gas is flammable and along with nitrogen poses an asphyxiation hazard and should only be used in a well-ventilated, spark-free environment.

CRITICAL: Small gold fiducials can be more precisely localized and obscure fewer specimen details, but they can be difficult to see at high tilt angles in thick samples. For objects larger than ~ 30 nm, use 10 nm colloidal gold, but for smaller specimens (for example, protein complexes under 1 MDa), 5 nm colloidal gold will likely be better. Some batches of colloidal gold are prone to clumping. In some cases, coating these particles with BSA helps prevent their aggregation (see the reagent setup section). In our experience this property neither improves nor degrades with shelf life, so if a good batch is found it can be used successfully for even years. Store colloidal gold solution at 4° C

in 1 ml aliquots, in 1.5 ml centrifuge tubes in order to minimize repeated contact with air and, implicitly, variations in temperature and possible contamination that may cause further aggregation.

EQUIPMENT

- lacey carbon film on 200 mesh copper grids (Ted Pella, Redding, CA, USA, www.tedpella.com) or Quantifoil holey carbon films (various sizes) on 200 mesh
- copper/rhodium grids (Quantifoil Micro Tools, Jena, Germany, www.quantifoil.com)
- plasma cleaner (Harrick, Model PDC-32G)
- filter paper (pre-punched from FEI Co or Whatman #1)
- grid boxes (usually custom-made)
- anticapillary tweezers (SPI Supplies, West Chester, PA, USA, www.2spi.com)
- vortexer
- FEI Vitrobot (FEI Company, Hillsboro, OR, USA, www.vitrobot.com)
- forceps or long tweezers
- cryo-transfer dewars

CAUTION: Any metallic tool such as a forceps or tweezer in contact with liquid nitrogen will be extremely cold and should be handled with care and appropriate personal protective equipment (gloves).

EQUIPMENT SETUP

Grids CRITICAL: Before starting, carefully choose which type of grid to use. In our experience, the carbon film of lacey grids is more sensitive to dose than that of Quantifoil grids. Therefore, if the intended total dose per tomogram exceeds ~ 60 electrons/Å^2, Quantifoil grids are a better choice. Furthermore, the selection of the type of Quantifoil film (hole size) depends on the type of sample and the targeted magnification (pixel size of the image). During data collection, successive tilts are correlated with each other to maintain tracking, and it is helpful to have contrast-rich features in the field of view. For small objects (10–100 nm) such as protein complexes or viruses that are imaged at 4–5 Å per pixel and have little contrast, Quantifoil holey film grids such as R 0.6/1 or R1.2/1.3 are most suitable because the holes are smaller and their edges guide the tracking. On the other hand, for cells that are around 2 μm in length, R 2/2 or R 2/1 grids are more appropriate because the entire cell can be housed within a hole. Although we have not tried this specifically, for much longer cells, we would predict that R 3.5/1 or S 7/2 grids would be even better.

In our experience, grids that are nominally identical but were manufactured on different days can behave quite differently with regards to dose (they may bubble earlier) or wetting (the ice distribution may be uneven). We think that grids bubble sooner if they are dirty and distribute ice more poorly as they age. Because of this we procure freshly manufactured grids. Our main grids supplier, Quantifoil, labels the batches of grids with the date on which the carbon film was applied. One way to clean the grids is to simply rinse them in methanol before glow-discharging. An easy way is to float them on a drop

of methanol on parafilm for 30 seconds, then pick them up with anti-capillary tweezers, remove most of the methanol by touching the grid edge to filter paper, and then let them finish drying by evaporation.

Because the cooled freezing apparatus becomes increasingly contaminated with ice during the procedure, we recommend that only two boxes of grids (8 grids total) should be frozen per session.

Vibrobot Turn on the tank of compressed air ensuring that the proper air pressure (at least 6 bar) is applied to the Vitrobot. Fill the humidifier with distilled water using the special 60 ml syringe. Mount the filter paper on the blotting pads, securing them with the clip rings (it is better to do this while the Vitrobot is off because the plunger is not in the way). Turn on the Vitrobot and set the desired parameters in the Console and Options screens: temperature, humidity (100%), type of application (manual or automatic), the blotting time, blotting offset, drain time, wait time, etc.

REAGENT SETUP

Sample Depending on the molecular weight of a purified specimen, the concentration of the sample should be somewhere between 0.3–8 mg/ml. In our hands, saturated bacterial cultures produce well-populated grids when the cells are concentrated about 20 times by very gentle centrifugation. Care must be taken, however, because centrifugation or turbulent ejection from a small-diameter syringe can shear off external structures such as pili or flagella and can distort cell shape. Likewise, extensive centrifugation may distort

the shapes of viruses or cause other structural damage. Whenever possible, use buffers low in salt and without glycerol or sucrose to increase contrast.

Bovine serum albumin (BSA)-treated colloidal gold Coating the gold fiducials with BSA can help prevent clumping and promote even distribution on the grid. To do this, make a stock solution of 5% (w/v) BSA solution in distilled water. Using a tabletop centrifuge, pellet a volume of 10 nm colloidal gold for ~ 10 minutes at 18,000X gravity (25 minutes for 5 nm colloidal gold). Carefully remove the supernatant with a micropipette. Resusupend the pellet of colloidal gold in the same volume of 1 % (w/v) BSA solution and incubate at 4 °C or room temperature for 30 minutes. Centrifuge the colloidal gold-BSA solution again for 10 minutes at 18,000X gravity to pellet the gold. Remove the supernatant and resuspend the gold pellet in a large (~ 500 μl) volume of distilled water (rinse step). Centrifuge one more time as before to pellet the gold and finally resuspend in deionized water at the desired concentration (typically 5X) for the treatment of grids or resuspend in some volume of the sample solution. Note that excess BSA will, of course, contaminate the sample. If it dries on the grid in abundance it can interfere with vitrification. Note also that even when BSA-treated, gold will precipitate in sample solutions if the solute concentration is too high. If the gold precipitates, this is immediately visible because the normally red color of the gold solution turns purple.

PROCEDURE

First phase: Preparation of gold, grids, and the sample. Timing: 30–60 min

1 Briefly vortex (~ 10 s) a tube of 10 nm colloidal gold solution. (Two concentrations of colloidal gold solution will be prepared: a lower concentration to be applied to the grids (2X-concentrated) and a higher concentration to be mixed with the sample (4 to 7X-concentrated). Expect to use 5 μl of each concentration of gold per grid.)

2 Pipette into one tube (tube "A," for grid treatment) 10 μl of unconcentrated gold per grid.

3 Pipette into a second tube (tube "B," for sample treatment) 30 μl of unconcentrated gold per grid.

4 Centrifuge the colloidal gold solutions using a tabletop microfuge at 18,000X gravity for 10 minutes to pellet the gold. If 5 nm colloidal gold solution is used, the centrifugation duration should be extended to 25 minutes.

5 Remove the supernatants, being careful to avoid losing gold.

6 Resuspend the pellet from tube A in 5 μl filtered deionized water per grid with a pipet.

7 Glow-discharge the grids in a plasma cleaner for between 30 seconds and 2 minutes, ensuring that the carbon film of the grids is exposed to the plasma.

8 Pick up the grids with anticapillary tweezers so that the carbon face is upward.

9 Vortex the tube of 2X-concentrated colloidal gold solution (tube A) at maximum speed for ~ 3 minutes and apply 5 μl of this solution onto the carbon side of the first 2–3 grids (part of the vortexing can be done while the grids are being glow-

discharged). If more than 3 grids are to be prepared, one may briefly vortex the 2X-concentrated gold solution after treating every 2–3 grids to decrease clumping.

10 Bake the grids in a 50 °C oven (drying will take less than 10 minutes) or let them air dry (drying may take 30 minutes or more).

11 Add an appropriate amount of sample to the gold pellet in tube B (see comments on ideal sample concentrations above). As soon as the grids have dried, be ready to proceed with the vitrification.

TROUBLESHOOTING

Second Phase: Cooling the Vitrobot cup. Timing: ~ 10 min

CAUTION: This step should be done in a fume hood or a well-ventilated area, as a large amount of nitrogen and some ethane is released. Liquid nitrogen, liquid ethane. and cryogen-cooled metallic tools (such as forceps or tweezers) are extremely cold: be sure to wear appropriate personal protective equipment (gloves, goggles, lab coat, and closed-toe shoes) and be careful when handling these reagents and tools.

12 Start cooling the Vitrobot cup while the grids are drying. Fill both the central ethane cup and outer nitrogen ring initially with liquid nitrogen to cool them down quickly. (The Vitrobot cup is cylindrical and consists of a central cup for liquid ethane into which the grid is plunged and a larger peripheral ring for liquid nitrogen. Between these chambers is a gap spanned by carefully designed thermal connectors that

conduct just enough heat that the ethane will first liquefy and then very slowly freeze.) Grid boxes may be placed in their holders in the outer ring at this time and cooled along with the Vitrobot cup. Keep replenishing the liquid nitrogen in the outer ring so that it is at least 75% full at all times.

13 When vigorous liquid nitrogen bubbling has ceased, begin liquefying ethane in the central cup. To do this, open the ethane tank slightly to produce just a modest flow rate directed towards the bottom or side of the cold cup wall. (If the flow rate is too low, the ethane will solidify. If the flow rate is too fast, it will not liquefy and will blow out of the chamber. Holding the tip of the ethane supply tube against the inner wall of the ethane cup facilitates condensation.)

14 Continue filling the ethane cup until it is full.

15 Wait until a thin layer of solid ethane coats the inner walls of the ethane cup to ensure that the liquid ethane is cool enough. If too much of the ethane becomes solid, melt it by blowing in more warm ethane gas.

16 When necessary, refill the ethane cup to the brim. To avoid ice contamination, make sure that the tip of the ethane supply tube is dried completely each time you introduce it into the ethane cup.

CRITICAL: The rate of heat transfer between the ethane cup and the outer nitrogen ring is important. If the heat transfer rate is slow, it takes a longer time to liquefy the ethane. If the heat transfer rate is too fast, the ethane may solidify too quickly. For the newest Vitrobot model (Mark III) there is a metal frame that should be placed over the ethane compartment during the liquefaction process. It helps to transfer heat and liquefy the ethane more quickly. After filling the ethane compartment with

liquid ethane, the metal frame should be removed to prevent the ethane from rapidly solidifying.

Third phase: Sample vitrification. Timing: 3–5 min

17 Pick up the edge of a grid with the Vitrobot tweezers (tweezers especially constructed for the Vitrobot so that the fixed end can be attached onto the Vitrobot plunger and the pincers can be closed or opened by changing the position of a black clamp ring) and secure their grip on the grid by sliding the black clamp ring into the first notch.

18 Gently tap the tweezers on a finger to ensure that the grid does not fall off.

19 Bring the plunger in the appropriate position and mount the tweezers onto the tip of the plunger. (The Vitrobot provides two ways to apply samples to the grid. In the "manual application" mode, the sample is applied to the grid by hand with a pipetman through a side port in the blotting chamber. In the "automatic application" mode, the sample is placed in a 1.5 mL tube and secured in a holder in the blotting chamber, and the Vitrobot dips the grid into the tube before blotting. The choice of manual or automatic sample application depends on the amount of sample available. The depth to which the grid is dipped in the sample tube can be set. To use the automatic application mode, at least 50 μl of the sample must be available, but with samples smaller than even 100 μl, the grid and tweezers are sometimes damaged by hitting the tube walls near the bottom.) If the manual application mode is to be used, be sure the carbon side of the grid faces the sideport.

20 Double-check the parameters in the Console and Option screens. Different blotting parameters are needed for different samples. Our most successful parameters are summarized in Table 1.

21 Enable the humidifier to reach 100 % humidity.

22 Wait until the blotting chamber reaches the desired temperature and humidity.

23 Refill the nitrogen and ethane chambers of the Vitrobot cup as necessary.

24 Activate the plunger to bring the grid in the blotting chamber and enable the holder housing the Vitrobot cup to move it right under the blotting chamber.

25 If the 'automatic application' mode has been selected, the grid will be automatically dipped in the sample tube, blotted, and plunged in the ethane. Skip to Phase Four, Placing the grid in the storage box. Otherwise proceed with the manual application as follows.

TROUBLESHOOTING

26 Mix the sample again with a pipet or briefly vortex it.

27 Draw 3–5 μl of the combined sample and colloidal gold into the pipet, insert it through the sideport of the blotting chamber and discharge the sample onto the grid.

28 Close the entry port and wait until 100% humidity is restored in the climate chamber, if opening the port reduced the humidity.

29 Press the button to initiate grid blotting and plunging.

TROUBLESHOOTING

Notes: When using the automatic application option, we found that protein orientations in the ice were more randomly distributed and, for the same concentration of protein, the particles were more numerous in a given area than in the case of manual application. The increased range of views is important for single particle analysis. If the sample is fairly dilute and for some reason cannot be further concentrated, one way we have been able to increase the number of objects per field of view is to use the sequential application option, which was not described earlier for simplicity. This allows for the sample to be applied and blotted several times before plunge freezing. We have used at most two sequential applications.

If no sample is seen on the grids, it may be preferentially adhering to the blot paper (see Troubleshooting table). In this case, the grid can be manually blotted from its edge (rather than "face on") with a small piece of blotting paper inserted through the side port with tweezers. This minimizes the contact area while maintaining the controlled environmental conditions.

The drain time may be adjusted to 1 s to increase the likelihood of thin ice and/or to get more uniform ice (instead of the typical gradient), in cases where the increment in the blotting time (0.5 s) is insufficient to define optimal sample preparation conditions. For example, in the case of *Caulobacter crescentus* cells, 2 seconds of blotting is too long, and 1.5 seconds without drain time is too short, so we use 1.5

seconds with a 1 second drain time. Additionally, using a drain time of 1 s or more may also avoid formation of non-vitreous ice with samples where this may be a problem.

There is an optional wait time between the application of the sample to the grid and blotting, during which time the sample solution may reach equilibrium with its environment. For some of our protein complexes, a 15–30 second wait time resulted in grids with more randomly distributed and numerous particles in a given area than 0 seconds waiting. In the case of some of our viral samples, a 15 second wait time increased the number of viral particles present. Presumably this is because some samples adhere to the grid in time and remain throughout the blotting process.

Fourth phase: Placing the grid in the storage box. Timing: 1–2 min

30 Slide the Vitrobot tweezers off the tip of the plunger while keeping the grid submerged within the liquid ethane.

31 Support the tweezers on the edge of the ethane cup, again keeping the grid completely immersed in liquid ethane, and stabilize your hand against the side of the Vitrobot cup.

32 Using both hands, move the cryogen cup from the Vitrobot to the bench so that there is more room to maneuver the grid and tweezers.

33 In one swift motion transfer the grid from the ethane to the liquid nitrogen ring. Alternatively, with the latest model of the Vitrobot (Mark III), the transfer of the tweezers from the ethane cup to the liquid nitrogen ring can be done automatically.

Before doing this, fill the nitrogen reservoir again after its descent and before activating the movement.

34 Slide the black clamp ring off the tweezers while keeping them pinched closed with your fingers.

35 Gently move the tweezers close to the grid box and place the grid in the desired slot.

TROUBLESHOOTING

Fifth phase: Iterations. Timing: 4–6 min per grid

36 Before proceeding with the next grid, if there is any condensation on the outside bottom part of the climate chamber resulting from the contact of the chamber with the cold Vitrobot cup, wipe it off with a paper towel and/or warm it with a heat gun.

37 Dry the Vitrobot tweezers with a Kim wipe.

38 Repeat steps 17–37 for each new grid.

Sixth phase: Sample storage. Timing: 2–3 min

39 When all the grids have been frozen and placed in the grid boxes, cool the grid box lids in liquid nitrogen and secure them on top of the grid boxes. (If the lids are fastened by screws, pre-cool the screwdriver before touching it to the grid boxes.)

40 Cool a pair of forceps or long tweezers in liquid nitrogen and use them to move the grid box into a liquid-nitrogen-filled transfer dewar.

41 Store the grid box under liquid nitrogen until ready for observation.

PAUSE POINT: If the grids will not be used immediately, the grid box can be stored essentially indefinitely in a 50 ml screw-cap conical tube. We typically punch two holes on opposite sides of the tube, approximately 1 cm below the bottom thread, and loop an ~ 4 ft long labeled nylon or polyester string through the holes. We then fill the 50 ml tube with liquid nitrogen, drop the grid storage boxes into it, and place the tube in a cane which is finally lowered into a large nitrogen cryostorage dewar with the labeled string hanging out the top.

TIMING

Steps 1–11 (Preparation of gold, grids, and the sample) take 30–60 minutes depending on which method is used to dry the gold solution onto the grids. Steps 12–16 (Cooling the Vitrobot cup) take about 10 minutes. Steps 17–29 (Sample vitrification) take 3–5 minutes. Steps 30–35 (Placing the grid in the storage box) take 1–2 minutes. Steps 36–38 (Iterations) take 4–6 minutes per grid. Finally, steps 39–41 (Sample storage) take 2–3 minutes.

ANTICIPATED RESULTS

This protocol typically produces plunge-frozen electron cryomicroscopy grids with suitably thick ice covering most of the grid (~ 70% or more) and a uniform gold distribution (see Fig. B-1 for an example). The preparation of 8 grids takes less than two hours and most of these grids are suitable for single- or dual-tilt tomography data collection.

REFERENCES

Adrian, M., Dubochet, J., Lepault, J., and McDowall, A.W. (1984) Cryo-electron microscopy of viruses. *Nature* **308**: 32-36.

Adrian, M., ten Heggeler-Bordier, B., Wahli, W., Stasiak, A.Z., Stasiak, A., and Dubochet, J. (1990) Direct visualization of supercoiled DNA molecules in solution. *Embo J* **9**: 4551-4554.

Angell, C.A. (2004) Amorphous water. *Annu Rev Phys Chem* **55**: 559-583.

Benjamin, J., Ganser-Pornillos, B.K., Tivol, W.F., Sundquist, W.I., and Jensen, G.J. (2005) Three-dimensional structure of HIV-1 virus-like particles by electron cryotomography. *J Mol Biol* **346**: 577-588.

Briegel, A., Dias, D.P., Li, Z., Jensen, R.B., Frangakis, A.S., and Jensen, G.J. (2006) Multiple large filament bundles observed in Caulobacter crescentus by electron cryotomography. *Mol Microbiol* **62**: 5-14.

Dubochet, J., and McDowall, A.W. (1981) Vitrification of pure water for electron microscopy. *J. Microsc.* **124**: RP3-4.

Frederik, P.M., and Hubert, D.H. (2005) Cryoelectron microscopy of liposomes. *Methods Enzymol* **391**: 431-448.

Henderson, G.P., and Jensen, G.J. (2006) Three-dimensional structure of Mycoplasma pneumoniae's attachment organelle and a model for its role in gliding motility. *Mol Microbiol* **60**: 376-385.

Iancu, C.V., Wright, E.R., Benjamin, J., Tivol, W.F., Dias, D.P., Murphy, G.E., Morrison, R.C., Heymann, J.B., and Jensen, G.J. (2005) A "flip-flop" rotation stage for routine dual-axis electron cryotomography. *J Struct Biol* **151**: 288-297.

Iancu, C.V., Wright, E.R., Heymann, J.B., and Jensen, G.J. (2006) A comparison of liquid nitrogen and liquid helium as cryogens for electron cryotomography. *J Struct Biol* **153**: 231-240.

Komeili, A., Li, Z., Newman, D.K., and Jensen, G.J. (2006) Magnetosomes are cell membrane invaginations organized by the actin-like protein MamK. *Science* **311**: 242-245.

Lepault, J., Booy, F.P., and Dubochet, J. (1983) Electron microscopy of frozen biological suspensions. *J Microsc* **129**: 89-102.

Li, H., DeRosier, D.J., Nicholson, W.V., Nogales, E., and Downing, K.H. (2002) Microtubule structure at 8 A resolution. *Structure* **10**: 1317-1328.

Lucic, V., Forster, F., and Baumeister, W. (2005) Structural studies by electron tomography: from cells to molecules. *Annu Rev Biochem* **74**: 833-865.

Murphy, G.E., and Jensen, G.J. (2005) Electron cryotomography of the E. coli pyruvate and 2-oxoglutarate dehydrogenase complexes. *Structure* **13**: 1765-1773.

Murphy, G.E., Leadbetter, J.R., and Jensen, G.J. (2006) In situ structure of the complete Treponema primitia flagellar motor. *Nature* **442**: 1062-1064.

Nickell, S., Kofler, C., Leis, A.P., and Baumeister, W. (2006) A visual approach to proteomics. *Nat Rev Mol Cell Biol* **7**: 225-230.

Wright, E.R., Iancu, C.V., Tivol, W.F., and Jensen, G.J. (2006) Observations on the behavior of vitreous ice at approximately 82 and approximately 12 K. *J Struct Biol* **153**: 241-252.

Figure and Tables

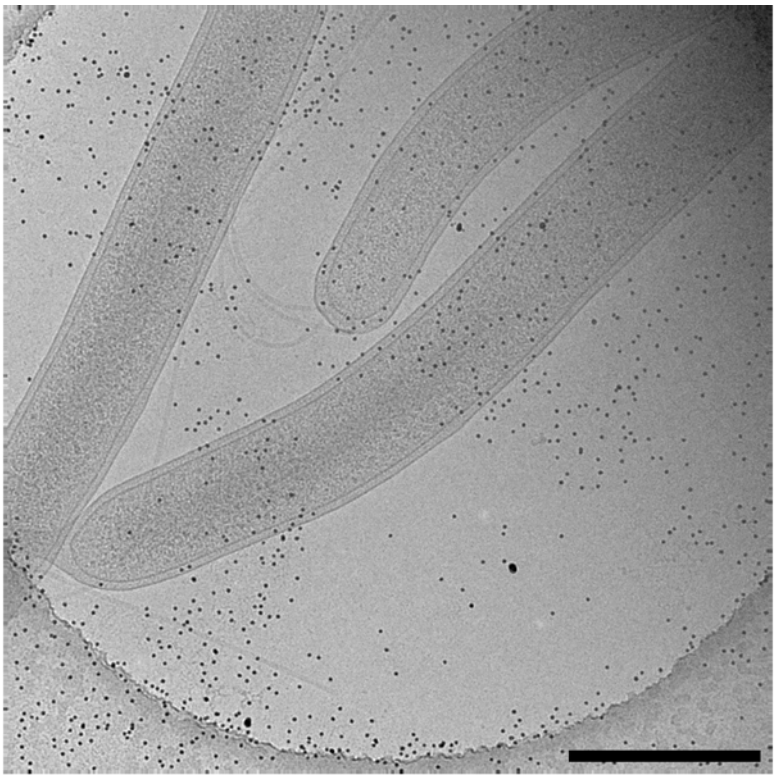

Figure B-1. Example image showing well-preserved bacterial cells, a good distribution of gold fiducials, and thin ice.

Energy filtered (20 eV slit) image collected on a 300 kV FEG "G2 Polara" TEM (FEI Company), using a 2048 x 2048 GIF CCD (Gatan, UK) and a pixel size of 0.98 nm. (Scale bar is 500 nm.)

Sample	Blot time (s)	Blot offset (mm)
Large protein complexes	3-4	2-3
Viruses	2-3 + drain time 0.5-1 s	2
Organelles	1-2	1-2
Cells	1-2 + drain time 1 s	1-2

Table B-1. Vitrobot blotting parameters for different samples.

"Blot time" is the period that the blot pads are pressed against the sample. "Blot offset" describes the position of the grid between the blot pads and partially controls the pressure exerted by the blotting paper on the grid. Larger absolute values of the blot offset produce a steeper ice thickness gradient on the grid. Blot offset values in the table are negative numbers. "Drain time" is the delay between blotting and plunging.)

Table 2. Troubleshooting.

Problem	*Possible reason*	*Solution*
Steps 1–11. Non-uniform dispersion of colloidal gold (associated with massive aggregation of gold particles)	The buffer is potassium phosphate or has high concentrations of salt or other additives promoting the aggregation of gold. If the gold solution changes color (like from pink or red to purple), this indicates it has precipitated.	Try to minimize salts and additives. Otherwise, apply gold only on the grids, avoid combining gold with the sample, or treat the gold with BSA.
Steps 12–35. Formation of non-vitreous ice on the grids	Humidity in the climate chamber may not have reached 100% in the blotting chamber.	Double-check that the humidity sensor is working properly.
	The transfer of the grid from the ethane cup to the liquid nitrogen ring was too slow.	Accelerate the transfer. If the Vitrobot Mark III model is available, use the automatic transfer option.
	The ethane may not have been cold enough.	Check that there is a thin film of solid ethane on the sides of the cup at all times and that the liquid nitrogen level is maintained throughout the freezing session.
Steps 25 or 29. Damaged grids (some of the carbon film gets stuck on the blotting paper)	The blotting pressure is too high.	Reconsider the blotting offset or ensure that the blotting pads function properly. The springs of the blotting pads may need to be adjusted or replaced.
	If, after the blotting, the wet spots on the blotting paper are significantly different in size for the two pads, the blotting mechanism is probably not centered correctly with respect to the plunger.	Recenter the blotting mechanism relative to the plunger.
Steps 25 or 29. No sample is visible on the grid	The sample is sticking to the filter paper.	Blot manually from the edge of the grid.